Title
Engineering Micro- and Nanostructured Biomaterials for Cell and Tissue Engineering

Author
Lee, Benjamin Li-Ping

Publication Date
2014

Peer reviewed|Thesis/dissertation

Engineering Micro- and Nanostructured Biomaterials for Cell and Tissue Engineering

By

Benjamin Li-Ping Lee

Dissertation

submitted in partial satisfaction of the requirements for the degree of

Joint Doctor of Philosophy

with University of California, San Francisco

in

Bioengineering

in the

Graduate Division

of the

UNIVERSITY OF CALIFORNIA, BERKELEY

Committee in charge:

Song Li, Ph.D. (Chair)
Randall Lee, M.D., Ph.D.
Kyriakos Komvopoulos, Ph.D.

Spring 2014

Copyright Page

Engineering Micro- and Nanostructured Biomaterials for Cell and Tissue Engineering

By Benjamin Li-Ping Lee

Abstract

Tissue engineering has emerged as a well-investigated research area that aims to ultimately create biological substitutes, ranging from skin replacement to artificial blood vessels, for regenerative medicine applications. It is a multidisciplinary field that integrates knowledge and advancements from biology, materials, chemistry, and many others. Although the goal of tissue engineering is to engineer tissues with structure and function that closely mimic those of native tissues for not only diagnostic and drug testing applications but also repair and replacement of diseased and injured tissues, it provides in-depth understanding of tissue development and morphogenesis, including the intricate biological systems in the body that together operate to direct growth, repair, and death.

The general approach of tissue engineering is to use cells, biomaterials, bioactive molecules, or a combination thereof to best recapitulate the properties of native tissues and reconstitute function. Specifically, biomaterial scaffolds play a key role in that their main function is to serving as a basis to interact with and support cells, promoting their attachment and migration while providing a porous and biomimetic microenvironment for mass transport and integration of bioactive factors.

Therefore, in order to fabricate implantable scaffolds with properties that emulate the natural extracellular matrix (ECM) in terms of structure and organization, we utilize and implement electrospinning technology. Electrospinning is a versatile technique with immense potential to create cell-instructive scaffolds possessing ECM-like fibrous structures. Because of the ability to tune scaffold structure with respect to physical (i.e. geometry and mechanical properties) and chemical (i.e. retention and presentation of bioactive molecules) features, electrospun scaffolds, which are made from synthetic, natural, or a combination of the two polymers, have demonstrated functional success in an array of tissue engineering applications. In fact, the fibrous network, especially in the nanoscale, possesses high surface-area-to-volume ratio that is favorable for surface modifications to facilitate cell attachment as well as immobilization and covalent conjugation of bioactive molecules. However, one major shortcoming of electrospun scaffolds as a result of such densely packed network of fibers is their small pore size, limiting cell infiltration and tissue ingrowth essential for desired angiogenesis and tissue integration. Thus, electrospun scaffolds with dense fibrous structure and small pore size have not had enormous success in the regeneration of large, more complex tissues that require abundant vascularization and mass transport of oxygen and nutrients.

In this dissertation, we attempt to address both the physical and chemical elements of electrospun scaffolds as we engineer novel ways to modulate their structural features and surface chemistry for their utilization in different cell and tissue engineering applications. We focus primarily on micro- and nanostructures, topographical cues, and chemical modifications and their role in enhancing cell infiltration and promoting better tissue integration in terms of angiogenesis in and overall functional performance of implanted scaffolds as well as vascular graft. Specifically, we detail the employment of an ultrafast, femtosecond (FS) laser system as a promising post-fabrication technology to pattern structural features (i.e. through-holes) that influence cell behavior and improve the integration electrospun scaffolds *in vivo*. We also demonstrate that changes in biophysical factors, such as increasing pore size and porosity via incorporation and removal of sacrificial fibers from composite scaffolds, can not only improve cell infiltration but more importantly regulate stem cell differentiation. Lastly, we show that we can fabricate small-diameter, nanofibrous vascular graft made of Carbosil®, a commercially available polycarbonate-urethane (PCU), via electrospinning and subsequently manipulate its surface properties through plasma treatment and reductive amination to effectively end-point immobilize heparin to reduce surface thrombogenicity while enhancing bioactivity and short-term *in vivo* performance.

In summary, we offer novel design and fabrication of electrospun scaffolds with large pore size and highly porous structure, and vascular grafts with tailored surface chemistry and bioactivity optimal for their biological performance. We demonstrate through our studies that physical and chemical features of not only electrospun scaffolds but implantable biomaterials in general can be engineered and manipulated using post-fabrication processing (i.e. FS laser and tunable surface chemistry) and unique fabrication approaches (i.e. multiple polymers with sacrificial components). Only with ample vascularization and tissue integration will such biomaterial scaffolds regenerate native tissue function and demonstrate success in both simple, such as skin substitutes, as well as complicated, such as artificial heart, tissues and organs for applications in regenerative medicine.

Table of Contents

List of Figures

List of Tables

Acknowledgments

Why did I decide to embark on the notorious Ph.D. journey? Should I have prepared myself better and gone to medical school instead? These were few questions that resided in the back of my mind throughout my graduate study. To be honest, I believe it was a combination of my lack of thorough preparation along with a bit of laziness. In particular, I used AP credits to skip numerous prerequisite classes during my undergraduate years, which prevented me from being eligible to apply for most medical schools unless I was willing to delay my graduation and make up those courses; in addition, during my senior year, I did not actively search for full-time jobs in biotech industry, which up to this day I blame myself for being afraid to challenge the financial crisis in 2009 but more importantly to begin the next stage of my life. Thus, I ultimately decided to apply for graduate programs, specifically Ph.D. programs as I learned that they would essentially pay the students to remain in school while conducting research.

I was fortunate enough to be accepted back into UC Berkeley for the UC Berkeley/UCSF Graduate Program in Bioengineering. However, the first two years were filled with disappointments and insecurities. Despite doing rotations during the first year to find a lab that best fits my interests, I limited myself again of the options as I only wanted to return to the Li lab, the lab where I initially and officially began my research career with a group of friendly fellow undergrads, graduate students, and post-docs whom I had built a strong connection with. Even though I knew this lab was where I wanted to continue my research and graduate studies, the situation became more complicated as funding issues became problematic. Luckily, through my determination as well as Dr. Li's trust and belief that I would be a diligent and successful graduate student, I secured myself a spot and was welcomed back to the Li lab. As the research slowly progressed with numerous experiments failing, I struggled with self-motivation as I transitioned from an undergraduate to a graduate student. In fact, I was unsure whether I would be able to overcome the many obstacles of Ph.D., including troubleshooting, redoing experiments to obtain valid and exciting results, and ultimately publishing journals and making contributions to the scientific community. Eventually, it would take me a seemingly-endless five years of hard-work and dedication to complete my graduate study and attain that priceless Ph.D. diploma. Of course, I would not have been able to reach this end of the tunnel without the encouragement, guidance, support, and love from everyone who I would sincerely like to acknowledge and dedicate the following section to.

First and foremost, I truly want to thank my wonderful family, especially my lovely parents and younger brother Andy. I want to thank my parents for always being there for me even when they are in Taiwan. You constantly reminded me to take care of myself in terms of staying healthy and happy (or at least be optimistic and search for that silver lining), and offered me financial support. Your unconditional love and support for me as the elder son truly provided me the strength and desire to fight on and be the best that I can be. Next, I want to thank Andy. I truly appreciate you always looking up to me as your older brother and a role model, whether it is academic- or hobby-related. Your intelligence and performance in medical school now surprises me yet makes me a proud older brother. I also have to thank you for helping me to take care of mom and dad, as you keep them entertained and happy with your humor and carelessness. In addition, I

have to thank all of my grandparents. Even though God or Buddha took you away from me while I was still in graduate school, I have to thank you immensely for raising not only your children but also me to become who we are today, as individuals with the potential to influence the world and carry on your principles and traditions. I wish you were still here to attend my Ph.D. graduation, to see me represent our family as the first to receive a graduate degree. I would definitely do anything in the world to be able to celebrate that moment with you. To my adorable grandmas and grandpas, my lovely mom and dad, and Andy – you guys really mean the world to me; without you guys, I definitely would not be where I am today.

Next, I want to thank Tracy Wang (and her hospitable and caring parents). My life changed drastically after meeting this wonderful girl during my first rotation of graduate school. I was no longer the lonely guy who did not have a girlfriend. My life became more eventful and fun as I enjoyed spending time with her. Although there were times in which disagreements led to arguments and stressful times, I truly appreciate her presence as a supportive girlfriend and best friend. I am thankful for all the times Tracy waited in Stanley Hall for me to finish work, for going to the gym to exercise and relieve stress, and most importantly for sharing countless memorable dates together. There are definitely much more about Tracy for me to be grateful for, but I am truly most thankful for her emotional support and physical presence, as well as her extraordinary patience, encouragement, fun character, and love. I am really really glad that I decided to take BART that day on my way to SFGH for my rotation.

From a more academic standpoint, I would like to give tremendous thanks to my graduate advisor and mentor, Dr. Song Li. I truly appreciate him giving me the opportunity to start my research career and work in his lab as a clueless undergrad who just wanted some research experience, and eventually taking me back as a graduate student under his guidance and mentorship. I definitely learned everything about cardiovascular and tissue engineering in general from him. He re-directed me towards the right direction when experiments were not working and when I felt discouraged and lost. In the end, I could not have accomplished everything, including not only all my publications and conference proceedings as a hopefully productive graduate student but also my help and contributions to Li lab as a senior student, without his valuable advice, encouragement, demands, and both emotional and financial support.

Likewise, I would like to acknowledge and thank Dr. Randall Lee and Dr. Kyriakos Komvopoulos. In addition to agreeing to be on my qualifying exam committee (and questioning me to think deeper and work harder with my projects), they involuntarily agreed to be on my thesis committee as well. More specifically, I would like to thank Dr. Komvopoulos for providing me the opportunity to collaborate with him and one of his recent graduates, Qian Cheng. In fact, the collaboration opened new doors as I learned and discovered new techniques and principles but more importantly the importance of team work. I truly appreciate the valuable guidance and feedback from both Dr. Lee and Dr. Komvopoulos, especially their patience and willingness to read and review my thesis.

I am also grateful for all of my labmates with whom I worked with and alongside during my undergraduate and graduate years (a total of seven years!) in the lab. First, I want to thank Craig Hashi, for being a strict yet helpful graduate mentor and taking the time to train me. It was his success and ability to establish a start-up that sparked my

interest in cardiovascular tissue engineering, especially the development of vascular grafts. In addition, I want to especially thank (not in any specific order): Julia Chu (for being a great lab manager and never complained about my stupid questions about where things are despite my many years in lab), Aijun Wang (for being a friendly post-doc who was always willing to help and chat), YiQian (Eugene) Zhu and Zhenyu Tang (for being like older brothers and offering me guidance and advice on not only graduate school but also life in general), Randall Janairo and Jeffrey Henry (for working together on vascular graft-related projects and thus sharing ideas and protocols with me), Danielle (An-Chi) Tsou (for being an awesome labmate as well as offering valuable advice and stories), Timothy Downing (for being the life of the lab as an aspiring music artist (inside joke) and eventually a successful researcher and professor in the near future), Shyam Patel (for being incredibly knowledgeable in everything, especially electrospinning, as a patient and helpful mentor despite his affiliation with NanoNerve), Qian Cheng (for collaborating with me and publishing journals together), Falei Yuan and Jian Yu (for helping me with in vivo studies and small animal work), Xuefeng Qiu (for working diligently with me on the last couple vascular graft projects, especially with ALL the tedious animal work), Xinghai Ning (for being an unbelievably kind post-doc from Niren Murthy's lab who dedicated a lot of his time in helping me with the surface chemistry aspect of the vascular graft project while refreshing my knowledge in organic chemistry), Julia Chang (for being a very knowledgeable and down-to-earth labmate and neighbor in the student office), Dong Wang, Ching-Wen (Helen) Huang, Wen-Ching (Danny) Huang, Jennifer Soto, Weixi Zhong, Sze Yue Wong, Junren Sia, Fang (Zoey) Huang, and Tiffany Dai. I also have to thank several undergraduate students, specifically Jessie Tung, Neerav Dixit, and Neil Ray, who worked with me and had to endure my wrath at times when experiments and assays did not work.

On the same note, I would like to extend the appreciation to all of my friends with whom I frequently talk to and see. They have definitely provided me with the crucial motivation and work-life balance that keep me sane and optimistic.

I am also thankful for the funding I received during my graduate career. First, I have to thank National Institute of Health for offering me a stem cell training grant that helped support my studies for two years. Second, I greatly appreciate the scholarship and award from the Siebel Foundation, which is a prestigious award with a significant amount to support the final year of my studies. Both provided me with valuable financial, academic, and career development support.

Lastly but most importantly, I would also like to thank all the rats that were used in my studies throughout my graduate years. I apologize but am forever grateful for their sacrifices, which I hope will help me make significant contributions to the scientific community. As what I recall from an undergraduate bioengineering lab course at UC Berkeley, "A mouse is an animal that, if killed in sufficiently many and creative ways, will generate a PhD."

List of Publications

Benjamin L. Lee*, Zhenyu Tang*, Aijun Wang, Fang Huang, Zhiqiang Yan, Dong Wang, Julia S. Chu, Neerav Dixit, Li Yang, Song Li. (2013) Synovial Stem Cells and Their Responses to the Porosity of Microfibrous Scaffold. *Acta Biomater.* 9(7):7264-75.

Qian Cheng*, Benjamin L. Lee*, Kyriakos Komvopoulos, Song Li. (2013) Engineering the microstructure of electrospun fibrous scaffolds by microtopography. *Biomacromolecules* 14(5):1349-60.

Qian Cheng, Benjamin L. Lee, Kyriakos Komvopoulos, Zhiqiang Yan, Song Li. (2013) Plasma Surface Chemical Treatment of Electrospun Poly(L-lactide) Microfibrous Scaffolds for Enhanced Cell Adhesion, Growth and Infiltration. *Tissue Eng. Part A* 19(9-10):1188-98.

Benjamin L. Lee, Hojeong Jeon, Aijun Wang, Zhiqiang Yan, Jian Yu, Costas Grigoropoulos, Song Li. (2012) Femtosecond Laser Ablation Enhances Cell Infiltration into Three-Dimensional Electrospun Scaffolds. *Acta Biomater.* 8(7):2648-58.

Jian Yu*, Aijun Wang*, Zhenyu Tang, Jeffrey Henry, Benjamin L. Lee, Yiqian Zhu, Falei Yuan, Fengping Huang, Song Li. (2012) The effect of stromal cell-derived factor-1α/heparin coating of biodegradable vascular grafts on the recruitment of both endothelial and smooth muscle progenitor cells for accelerated regeneration. *Biomaterials* 33(32):8062-74.

Randall Raphael R. Janairo, Jeffrey J. D. Henry, Benjamin L. Lee, Craig K. Hashi, Nikita Derugin, Randall Lee, Song Li. (2011) Heparin-Modified Small-Diameter Nanofibrous Vascular Grafts. *IEEE Transactions on Nanobioscience* 11(1):22-27.

* denotes equal contribution.

CHAPTER 1

Introduction

Endeavors of Tissue Engineering

History

Tissue engineering is best defined as the use of cells, materials, or a combination of both with appropriate biochemical cues to restore, repair, or replace biological functions of damaged or lost tissues in the body. The term "tissue engineering" was coined by Y.C. Fung in 1985, and was officially introduced by the National Science Foundation in 1987. However, this emerging field was then further described by Langer and Vacanti, in which the concept of tissue engineering integrates the principles of biology and engineering for the development of functional substitutes for damaged tissue [1]. In fact, tissue engineering caught global attention after the introduction of the "Vacanti mouse," which was simply a laboratory mouse with a human ear-shaped, tissue-engineered cartilage grown on its back (Figure 1.1). Since then, the multidisciplinary field of tissue engineering, which bridges biology and materials science with chemistry, bioengineering, medicine, and other areas, has widely expanded as numerous groups worldwide are researching new technologies for engineering tissues as well as whole organs [2].

Figure 1.1. Vacanti mouse. Chondrocytes were seeded and cultured on a polymer ear mold *in vitro*, and the tissue-engineered cartilage construct was subsequently implanted into subcutaneous pockets on the back of athymic mice. Image courtesy of [3]

Principle

Tissue engineering was thus developed as an attempt to resolve the limited availability of tissues and organs for transplantation therapy. Regardless of the complexity of the target tissue, tissue engineering approaches almost always entail isolated cells or cellular substitutes, biomaterial scaffolds, and bioactive factors in various combinations to promote tissue repair and new tissue formation (Figure 1.2) [4]. In particular, biomaterials are essentially materials that are designed and used to control the biological environment of cells and tissues. Depending on the application and the specific tissue type, each strategy is precisely tailored and optimized with the utilization of single or multiple cell types (i.e. progenitor or mature cells) with or without suitable scaffolding (i.e. synthetic or natural biomaterials) and bioactive cues (i.e. cytokines or growth factors). For example, for heart valve tissue engineering, trileaflet valve constructs were fabricated from poly-4-hydroxybutyrate-coated polyglycolic acid scaffolds seeded with human marrow stromal cells, and subsequently cultured and grown *in vitro* in a bioreactor to promote maturation prior to *in vivo* implantation [5]. In addition, some tissues, such as bone and skin, have the innate potential to regenerate with the assistance of progenitor or stem cells, which can be isolated from almost every tissue in the body as suggested by recent studies [6]. In such cases, these adult stem cells can be stimulated to repair and form new tissue without biomaterial intervention under the right conditions with respect to their biochemical microenvironment. However, to translate these engineered tissue substitutes into large animals and ultimately humans for clinical application while retaining the same effectiveness in terms of function, cell source to obtain large numbers of cells and their survival after transplantation are important issues that need to be considered. One potential solution from a biomaterial perspective to address and ensure cell survival is the design, development, and optimization of cell-instructive scaffolds.

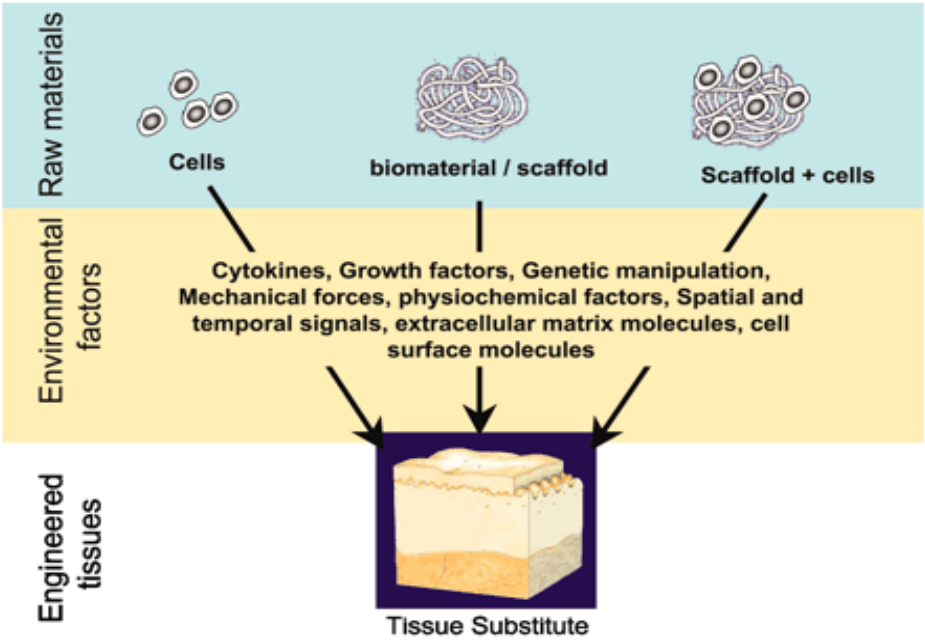

Figure 1.2. Tissue engineering strategies. The diagram shows various approaches in tissue engineering using cells, scaffolds, or a combination thereof, along with bioactive factors to construct a tissue substitute. Image courtesy of [7]

Biomaterial Scaffolds

Biomaterial scaffolds play a major role in tissue engineering in that their primary function is to serve as a foundation and provide physical support for the attachment and growth of not only transplanted but more importantly host cells. Specifically, tissue-engineered substrates must be cell-instructive in order to maintain cell viability and control cell behavior, as cells constantly interact with their surrounding extracellular matrix (ECM). In addition, the scaffold, which is preferably three-dimensional and highly porous in structure made from synthetic, natural, or a combination of both materials, must be built to facilitate tissue integration and growth in order to achieve desired tissue formation. However, this support would only be temporary as an ideally engineered scaffold should be degraded or resorbed (in the case of synthetic materials) without toxicity or digested and remodeled (in the case of natural materials) over time, allowing the native tissue of interest to progressively replace the construct and regain normal function. Moreover, depending on the specific application, scaffolds can be made with synthetic materials or natural polymers; synthetic materials are advantageous for their versatility and adjustable physico-chemical features (i.e. degradation rate, mechanical properties, surface chemistry) to closely mimic key components of the ECM, whereas natural polymers are inherently more similar to native tissues and thus favorable for inducing desired cell interactions and behaviors [8, 9].

In addition, the cultivation of cells in various engineered scaffolds with three-dimensional, ECM-like environments provide novel ways to study in-depth the cell-material interactions, specifically in better understanding the mechanisms of cell biology and tissue formation from a molecular perspective. These cell-instructive scaffolds can be fabricated by incorporating bioactive cues, such as cell-adhesion peptides or growth factors, and tailoring their surface or bulk presentation as well as controlled release to promote initial cell attachment and ultimately tissue regeneration. Furthermore, the growth and maturation of functional tissue is governed primarily by the appropriate cell differentiation and more importantly the constant interactions between cells and their surrounding microenvironment. However, in some cases in which it is difficult to maintain and regulate differentiation of certain cell types on scaffolds *in vitro* despite the addition of exogenous chemical cues, an *in vivo* bioreactor, such as the peritoneal cavity, can be used to provide a more familiar microenvironment for not only the cells but also the entire cellular construct [10, 11]. Such technologies to culture progenitor and stem cells on specially designed three-dimensional matrices are useful in recapitulating the *in vivo* setting to better elucidate and understand the various mechanisms of how cells interact in the formation of intricate tissue structures.

Angiogenesis

The integration of tissue-engineered scaffolds *in vivo*, especially in large tissues and organs, is primarily dictated by the formation of vascular network, specifically angiogenesis. Angiogenesis is the process in which new blood vessels, typically capillaries, sprout from pre-existing blood vessels in the body [12]. This natural process occurs immediately in response to tissue growth and repair, and thus is a critical for the survival and integration of constructs for tissue engineering therapies. In fact, the body responds to an implanted biomaterial within 24 hours after implantation, in which macrophages along with other inflammatory cells elicit chemoattractive signals to induce migration of fibroblasts and vascular endothelial cells into the area [13]. In order for a scaffold to obtain sufficient perfusion from vascular network critical for cell survival and tissue integration, it needs to be not only implanted in close proximity to existing vessels but more importantly designed with an interconnected network of pores to facilitate and enhance angiogenesis. Although creating functional vasculature may not be as essential in skin or cartilage tissue engineering in that tissue structures are thin or avascular, it is especially crucial in large, three-dimensional tissues. The dimensions and complexity of the implanted scaffold may present a significant barrier to mass transport, and thus the permeability and the porous structure are necessary for efficient oxygen diffusion as well as nutrient delivery and waste removal. Furthermore, because vascularization plays a key role in determining the functionality and integration with host tissue of any implanted scaffold, many groups have investigated the incorporation and controlled delivery of bioactive molecules to further induce and enhance angiogenesis [14]. For example, vascular endothelial growth factor (VEGF), a potent angiogenic factor, has been widely researched with materials-based approaches [15-17]. However, because angiogenesis is an inherently complex process, it is doubtful that a single bioactive molecule, such as VEGF, can provide all the mandatory cues to direct the numerous facets of angiogenesis in terms of initiating and stabilizing an entire network of vessels. Additional processing techniques applied to the fabrication of scaffolds for tissue engineering applications to promote angiogenesis and facilitate tissue integration will be discussed more in-depth in the following sections.

Porosity and Porous Network

Successful vascularization of and tissue ingrowth into tissue-engineered constructs are dependent on the porosity and pore size of the scaffolds. Hypoxia and cell death are apparent in thick scaffolds without sufficient porous network or vascular infiltration because cells cannot survive at distances greater than several hundred microns from the nearest capillaries without optimal transport of oxygen, nutrients, and waste [18, 19]. Studies have shown that an increase in pore size drastically decreased the inflammatory response without compromising the degree of angiogenesis after implantation of porous scaffolds [20]. In fact, a narrow range of optimal pore size exists; extremely large pore size prevents proper vascularization as they deter endothelial cells from bridging across pores larger than a cell diameter, whereas exceedingly small pores below submicron size adversely limit mass transport and angiogenesis [21].

In addition to facilitating angiogenesis and the integration with host vasculature and tissue, pore size, along with other structural properties, is also important in influencing cell-cell and cell-material communications in three-dimensional network, providing them space for growth and differentiation as well as organization and remodeling. In fact, we and others have demonstrated that highly porous biodegradable polymer scaffolds with a network of interconnected space favorable for cell spreading can be used as a platform to deliver and support stem cells as they offer an effective strategy to assist and potentially accelerate the formation of complex three-dimensional tissues [22, 23]. Such optimized porosity and uniform pore size are advantageous in terms of not only desired diffusion and vascularization but more importantly material integrity with mechanical cues to influence cellular behavior, especially stem cell proliferation and differentiation. Therefore, tuning the porosity of biomaterial scaffolds is an effective way to better enhance local angiogenesis *in vivo* by promoting a gradual penetration of host vasculature into the scaffolds during tissue integration and healing.

Host Response

In addition to an interconnected porosity to facilitate angiogenesis, the biocompatibility and functional performance of tissue-engineered scaffolds *in vivo* also relies on initial blood-material interactions and subsequent cascade of host tissue response. Interestingly, repair-associated angiogenesis as a result of tissue damage, such as injury due to scaffold implantation, is linked to the presence and activity of inflammatory cells and the wound healing process [24]. For instance, fibrin, which is a major component of the provisional matrix formed during wound healing filled with an array of bioactive molecules, is a natural biomaterial that has been prepared as growth matrices to deliver angiogenic growth factors and stimulate angiogenesis [25, 26]. In addition, even though synthetic polymers themselves generally do not induce an immune response due to the lack of biologically functional domains, the end-stage formation of fibrous capsule following foreign body reaction around implanted devices is almost inevitable as any artificial surface, regardless of its topography and chemistry, is considered foreign and triggers a series of events upon implantation [27]. For example, certain synthetic polymers, such as poly(glycolic) acid and other poly(α-hydroxy esters), produce acidic byproducts upon degradation that may result in thicker capsules and a prolonged inflammatory response [28]. As a result, excessive fibrous encapsulation is often considered a main failure mechanism of tissue-engineered implants. Although tissue engineering has been traditionally focused on utilizing different methods to modulate the fate of cellular or acellular constructs *in vivo*, recent progress has transitioned to the development of modified or new materials using biomimetic biomaterial-based strategies to better emulate molecular features of the ECM in order to mitigate or inhibit immune responses, including surface modifications to control protein adsorption or cell adherence as well as bulk modifications to incorporate desired therapeutic molecules [29-31]. Therefore, to achieve desired biocompatibility and bioresponse in the host environment, tissue-engineered implants are designed to lower the intensity and/or duration of the inflammatory response without sacrificing the angiogenic

element as neovascularization is essential during wound healing, repair, and restoration of normal tissue function.

Role of Macrophages

Although macrophages are typically perceived negatively for their contributions to downstream outcomes of host tissue response, they play both a detrimental role in the inflammatory response and a beneficial role in the remodeling process of implanted biomaterials. These inflammatory cells are derived from blood-borne monocytes that adhere to the surface of foreign scaffolds during the early stage of the acute inflammatory response and subsequently differentiate into macrophages that actively participate in wound healing during foreign body reaction [13, 32]. Although the exact activities of macrophage and the mechanism of their activation at the biomaterial interface is unclear, these activated macrophages eventually fuse to form foreign body giant cells (FBGCs), which interact with additional macrophages to form granulation tissue and fibrous capsule towards the final stages of the host response cascade. However, the exact composition of granulation tissue and fibrous capsule as well as the degree of their formation are affected the topography and surface chemistry of the implanted biomaterial as briefly mentioned previously. In addition, macrophages possess two primary functional phenotypes – pro-inflammatory (M1) or immunomodulatory and tissue remodeling (M2), despite having a remarkable plasticity to reversibly and progressively shift their functions in response to changes in microenvironmental influences [33, 34]. The pro-inflammatory, M1 phenotype is characterized by cytotoxic macrophages associated with chronic inflammation; in contrast, the anti-inflammatory, M2 phenotype is identified as macrophages that participate in tissue repair and modulate remodeling, which are two key aspects that determine the functional success of tissue-engineered scaffolds [35]. Moreover, recent studies have shown that porous biomaterials elicit foreign body reaction and fibrosis with less encapsulation and more vascularity compared to their non-porous counterparts of the same composition [36]. Similarly, researchers from the Ratner group demonstrated the porosity is associated with healing, in which materials possessing spherical, interconnected pores of approximately 30-40 μm healed with the highest vascularity along with minimal fibrosis and significantly higher ratios of M2/M1 macrophages [37, 38]. Another example involves controlling the local architecture and chemistry to allow selective vessel ingrowth only into desired regions, in which angiogenic and anti-angiogenic peptides were attached inside laser-drilled holes through the thickness of porous polypropylene disks [39]. Thus, from a tissue engineering perspective, the ability to mediate and better control the macrophage phenotype has major implications, since the M2 population is dominant in long-term remodeling, making it beneficial and favorable for the constructive remodeling of all scaffold materials.

Tissue-Engineered Vascular Grafts

Tissue engineering has been able to successfully create many tubular structures for the repair and/or regeneration of various tubular tissues in high clinical demand. One main example is vascular tissue engineering, specifically for coronary and peripheral arterial disease applications. Because of these vascular diseases, which affect millions of people worldwide with continuously rising prevalence, there is a huge unmet need for small-diameter (< 6 mm) vascular grafts as bypass and blood vessel replacement. Even though autologous vessels, typically taken from saphenous vein, are considered the gold standard and have demonstrated superior clinical outcome, they are limited by their availability as well as surgical morbidity and complications [40]. Similarly, an alternative uses synthetic grafts made of materials such as polyethylene terephthalate (Dacron) and expanded polytetrafluoroethylene (Teflon), but they are also limited primarily because of their inherently thrombogenic surface and compliance mismatch [41, 42]. Therefore, numerous groups, including us, have utilized various strategies aimed to develop an ideal, small-diameter vascular graft possessing both mechanical (i.e. compliant) and chemical (i.e. antithrombogenic) properties similar to those of native vessels. Examples of such approaches include decellularized vessels [43-45] and electrospun vascular grafts [46, 47] using synthetic and/or natural polymers in combination with different elements to achieve desired endothelialization both *in vitro* and *in situ* (Figure 1.3).

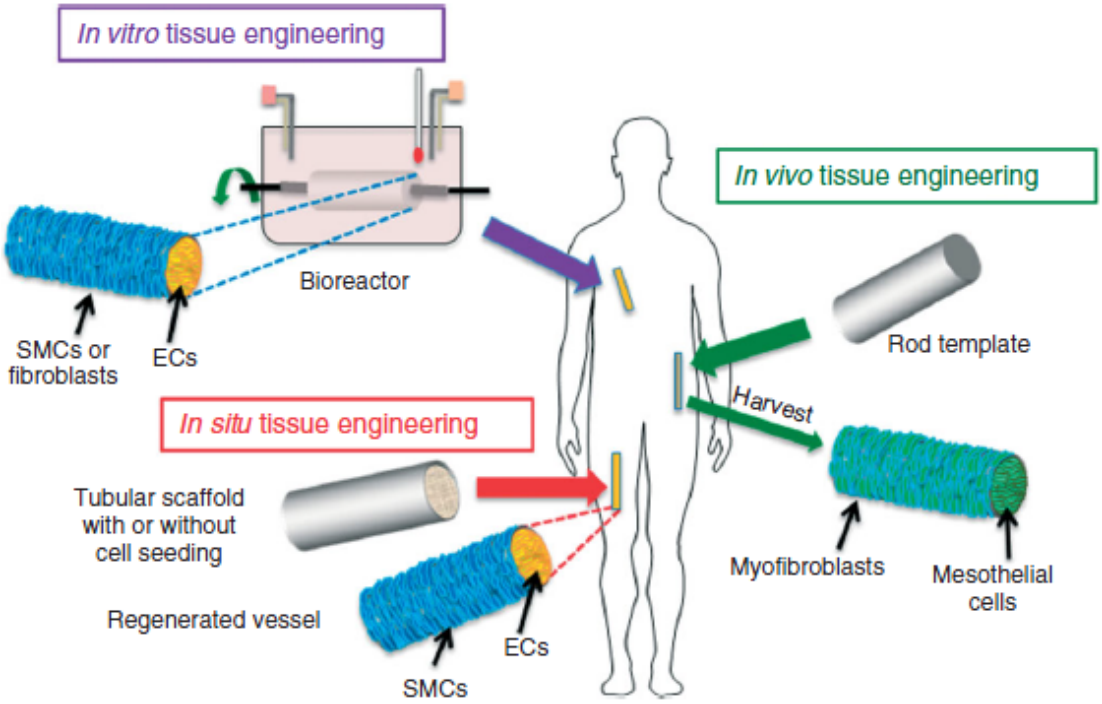

Figure 1.3. Tissue engineering of vascular grafts. The schematic illustrates current *in vitro*, *in vivo*, and *in situ* engineering approaches in the development of tissue-engineered vascular grafts. Image courtesy of [48]

Electrospinning

Electrospinning is a commonly utilized technique to fabricate tissue-engineered scaffolds that closely resemble the organized structure and biological function of native ECM [49]. It is a process that was first introduced by Lord Rayleigh in the late 19th century but further developed and described in early publications by the Reneker group [50, 51]. Electrospinning, which relies on the generation of an electric field between a positively charged capillary filled with a polymer solution and a typically grounded collector, is a simple yet versatile method that can easily produce nonwoven, three-dimensional fibrous structures with controllable fiber diameters ranging from tens of nanometers to microns [52].

A basic electrospinning setup is illustrated below (Figure 1.4):

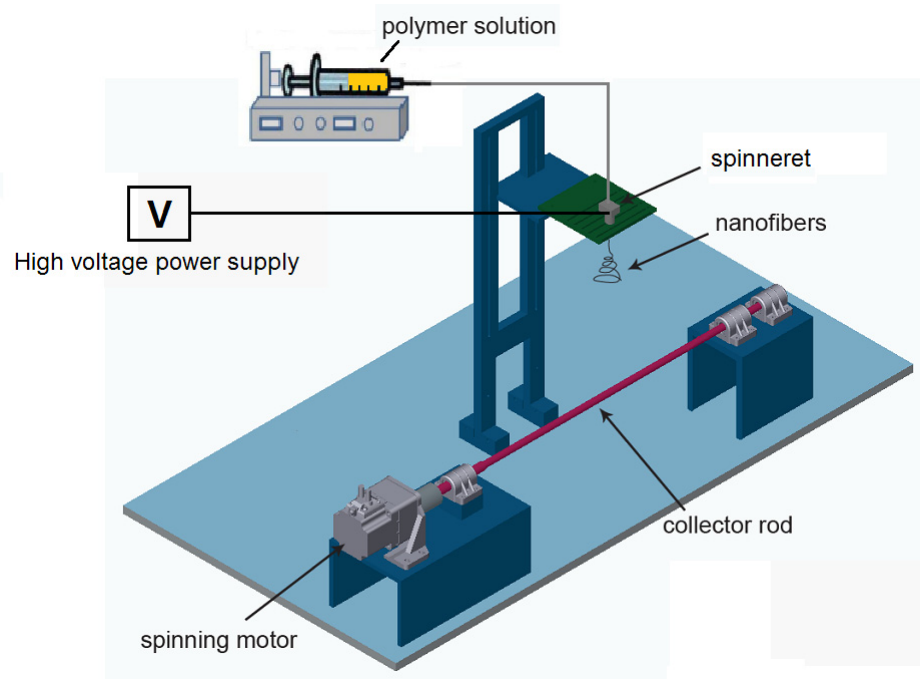

Figure 1.4. Electrospinning process. The setup consists of a spinneret, high voltage power supply, and collector. The polymer solution is delivered through a charged spinneret via syringe pump. In the presence of an electric field, a polymer jet is extruded, whipping across towards the collector to form micro- or nanofibers. Image modified from [53]

When the charged polymer solution is delivered through the spinneret (i.e. needle tip) in the presence of an electric field, a conical droplet forms as a result of the equilibrium between the surface tension of the droplet and the electric field. However, when the applied electric field overcomes the surface tension, a polymer jet is extruded from the tip. As this jet whips and travels across the electric field to the grounded target, the solvent in the jet evaporates and individual polymer fibers are deposited and collected.

In the end, a nonwoven fibrous scaffold with varying fiber diameter and morphology is produced. In fact, various electrospinning parameters, including polymer solution properties (i.e. concentration, viscosity, and conductivity of polymer and solvent), solution feed rate, gap distance between the tip of the spinneret and the collector, electric field strength (i.e. voltage), collector geometry (i.e. size and shape), temperature, and humidity, can be adjusted and optimized to attain desired fiber characteristics, especially fiber diameter and integrity (Table 1.1) [54, 55].

Parameters	Effect on fiber morphology
Solution parameters	
Viscosity	Low-beads generation, high-increase in fiber diameter , disappearance of beads.
Polymer concentration	Increase in fiber diameter with increase of concentration.
Molecular weight of polymer	Reduction in the number of beads and droplets with increase of molecular weight.
Conductivity	Decrease in fiber diameter with increase in conductivity.
Surface tension	No conclusive link with fiber morphology, high surface tension results in instability of jets.
Processing parameters	
Applied voltage	Decrease in fiber diameter with increase in voltage.
Distance between tip and collector	Generation of beads with too small and too large distance, minimum distance required for uniform fibers.
Feed rate/Flow rate	Decrease in fiber diameter with decrease in flow rate, generation of beads with too high flow rate.
Ambient parameters	
Humidity	High humidity results in circular pores on the fibers.
Temperature	Increase in temperature results in decrease in fiber diameter.

Table 1.1. Electrospinning parameters. Fiber morphology (i.e. diameter) can be fine-tuned by the control and optimization of various solution, processing, and ambient parameters. Table courtesy of [56]

Advantages and Disadvantages

Because of the versatility of electrospinning and the ability to control structure in terms of geometry and mechanical properties, electrospun scaffolds have tremendous potential as functional scaffolds for various tissue engineering applications [57, 58]. One main appeal of such scaffolds is that the electrospun fibrous structure is made to resemble the fibrous collagen networks observed in the natural ECM. In particular, electrospun fibers, especially in nanoscale dimension, possess high surface-area-to-volume ratio that is favorable for the attachment of not only exogenous and endogenous cells but also bioactive molecules on the fiber surface. However, regardless of the raw material selected for electrospinning, a major shortcoming that significantly limits the utilization of electrospun scaffolds is their small pore size. The finer the fiber diameter becomes, the

more densely the fibers are packed, leading to pore sizes that are too small for both seeded and host cells to migrate and reside inside. As a result of such dense fibrous network and the associated small pore size, cell infiltration and tissue ingrowth necessary to facilitate desired angiogenesis and tissue integration of implanted scaffolds as discussed earlier cannot be achieved, restraining the potential of electrospun scaffolds to be employed and effective in the regeneration of large, complex tissues that demand ample vascularization and diffusion of oxygen and nutrients.

Strategies to Engineer Desired Physical Features and Surface Chemistry

There are numerous strategies to engineer desired structure and surface chemistry of electrospun scaffolds to improve their performance in various applications. First, in order to address a physical issue and alleviate the detrimental effect of insufficient pore size and poor cell permeability on the functional performance of these scaffolds *in vivo*, an array of novel techniques that offers precise control of scaffold architecture and chemistry have been developed to improve tissue ingrowth and enhance vascularization. From an engineering standpoint, common examples of scaffold fabrication manipulation include: integration with three-dimensional printing [59, 60], incorporation of sacrificial polymers [22, 61] or porogens (i.e. salt) in particulate leaching to control scaffold composition [62, 63], as well as adjustments of electrospinning parameters to tailor fiber diameter and generate nano- and microfibers [64, 65]; likewise, examples of post-fabrication processing and modifications consist of: micropatterning [66], ultraviolet radiation treatment [67], and femtosecond laser ablation [68] to increase pore size or create additional topographical features. On the other hand, chemical modifications of dense, electrospun scaffolds to manipulate surface properties and emulate the bioactive features of ECM, specifically in terms of cell infiltration and vascularization, consist primarily of surface functionalization, such as plasma treatment [69, 70], covalent surface bonding [71, 72], and physical adsorption [73], and also bulk incorporation of bioactive molecules via direct mixing [74, 75], co-axial electrospinning [76], and other techniques. Therefore, the challenge to obtain antiquate cell infiltration and angiogenesis into dense electrospun scaffolds with small pore size and poor surface characteristics can be effectively overcome, expanding their utilization in both simple and complex tissues. With proper yet creative approaches, we aim to engineer the structure and surface chemistry of novel micro- and nano-biomaterials for cell and tissue engineering applications, including the development and fabrication of small-diameter bioactive vascular graft.

References

1. Langer R, Vacanti J. Tissue engineering. Science. 1993;260(5110):920-6.

2. Atala A, Kasper FK, Mikos AG. Engineering complex tissues. Science Translational Medicine. 2012;4(160):160rv12-rv12.
3. Cao Y, Vacanti JP, Paige KT, Upton J, Vacanti CA. Transplantation of chondrocytes utilizing a polymer-cell construct to produce tissue-engineered cartilage in the shape of a human ear. Plastic and Reconstructive Surgery. 1997;100(2).
4. Polak JM, Bishop AE. Stem cells and tissue engineering: past, present, and future. Annals of the New York Academy of Sciences. 2006;1068(1):352-66.
5. Hoerstrup SP, Kadner A, Melnitchouk S, Trojan A, Eid K, Tracy J, et al. Tissue engineering of functional trileaflet heart valves from human marrow stromal cells. Circulation. 2002;106(12 suppl 1):I-143-I-50.
6. Meirelles LdS, Chagastelles PC, Nardi NB. Mesenchymal stem cells reside in virtually all post-natal organs and tissues. Journal of Cell Science. 2006;119(11):2204-13.
7. Khademhosseini A, Langer R, Borenstein J, Vacanti JP. Microscale technologies for tissue engineering and biology. Proceedings of the National Academy of Sciences of the United States of America. 2006;103(8):2480-7.
8. Courtney T, Sacks MS, Stankus J, Guan J, Wagner WR. Design and analysis of tissue engineering scaffolds that mimic soft tissue mechanical anisotropy. Biomaterials. 2006;27(19):3631-8.
9. Reis RL, Neves NM, Marques AP, Santos TC, Oliveira JM, Boesel LF, et al. Natural origin biodegradable systems in tissue engineering and regenerative medicine: present status and some moving trends. Journal of The Royal Society Interface. 2007;4(17):999-1030.
10. Campbell GR, Turnbull G, Xiang L, Haines M, Armstrong S, Rolfe BE, et al. The peritoneal cavity as a bioreactor for tissue engineering visceral organs: bladder, uterus and vas deferens. Journal of Tissue Engineering and Regenerative Medicine. 2008;2(1):50-60.
11. Chue W-L, Campbell GR, Caplice N, Muhammed A, Berry CL, Thomas AC, et al. Dog peritoneal and pleural cavities as bioreactors to grow autologous vascular grafts. Journal of Vascular Surgery. 2004;39(4):859-67.
12. Helisch A, Schaper W. Arteriogenesis: the development and growth of collateral arteries. Microcirculation. 2003;10(1):83-97.
13. Anderson JM. Chapter 38 - Biocompatibility and bioresponse to biomaterials. In: Atala A, Lanza R, Thomson JA, Nerem R, editors. Principles of Regenerative Medicine (Second edition). San Diego: Academic Press; 2011. p. 693-716.
14. Patel Z, Mikos AG. Angiogenesis with biomaterial-based drug- and cell-delivery systems. J Biomater Sci Polym Ed. 2004;15(6):701-26.
15. Norton LW, Koschwanez HE, Wisniewski NA, Klitzman B, Reichert WM. Vascular endothelial growth factor and dexamethasone release from nonfouling sensor coatings affect the foreign body response. Journal of Biomedical Materials Research Part A. 2007;81A(4):858-69.
16. Backer MV, Patel V, Jehning BT, Claffey KP, Backer JM. Surface immobilization of active vascular endothelial growth factor via a cysteine-containing tag. Biomaterials. 2006;27(31):5452-8.

17. Zisch AH, Lutolf MP, Hubbell JA. Biopolymeric delivery matrices for angiogenic growth factors. Cardiovascular Pathology. 2003;12(6):295-310.
18. Colton C. Implantable biohybrid artificial organs. Cell Transplant. 1995;4(4):415-36.
19. Freed LE, Vunjak-Novakovic G. Culture of organized cell communities. Advanced Drug Delivery Reviews. 1998;33(1–2):15-30.
20. Bezuidenhout D, Davies N, Zilla P. Effect of well defined dodecahedral porosity on inflammation and angiogenesis. ASAIO Journal. 2002;48(5).
21. Salem AK, Stevens R, Pearson RG, Davies MC, Tendler SJB, Roberts CJ, et al. Interactions of 3T3 fibroblasts and endothelial cells with defined pore features. Journal of Biomedical Materials Research. 2002;61(2):212-7.
22. Lee BL-P, Tang Z, Wang A, Huang F, Yan Z, Wang D, et al. Synovial stem cells and their responses to the porosity of microfibrous scaffold. Acta Biomaterialia. 2013;9(7):7264-75.
23. Levenberg S, Huang NF, Lavik E, Rogers AB, Itskovitz-Eldor J, Langer R. Differentiation of human embryonic stem cells on three-dimensional polymer scaffolds. Proceedings of the National Academy of Sciences. 2003;100(22):12741-6.
24. van Hinsbergh VWM, Collen A, Koolwijk P. Role of fibrin matrix in angiogenesis. Annals of the New York Academy of Sciences. 2001;936(1):426-37.
25. Clark RAF. Fibrin and wound healing. Annals of the New York Academy of Sciences. 2001;936(1):355-67.
26. Wong C, Inman E, Spaethe R, Helgerson S. Fibrin-based biomaterials to deliver human growth factors. Thrombosis and Haemostasis. 2003;89(3):573-82.
27. Anderson JM, Rodriguez A, Chang DT. Foreign body reaction to biomaterials. Seminars in Immunology. 2008;20(2):86-100.
28. Lu L, Peter SJ, D. Lyman M, Lai H-L, Leite SM, Tamada JA, et al. In vitro and in vivo degradation of porous poly(dl-lactic-co-glycolic acid) foams. Biomaterials. 2000;21(18):1837-45.
29. Ratner BD. Reducing capsular thickness and enhancing angiogenesis around implant drug release systems. Journal of Controlled Release. 2002;78(1–3):211-8.
30. Novak MT, Bryers JD, Reichert WM. Biomimetic strategies based on viruses and bacteria for the development of immune evasive biomaterials. Biomaterials. 2009;30(11):1989-2005.
31. de Mel A, Jell G, Stevens MM, Seifalian AM. Biofunctionalization of biomaterials for accelerated in situ endothelialization: a review. Biomacromolecules. 2008;9(11):2969-79.
32. Johnston RB. Monocytes and macrophages. New England Journal of Medicine. 1988;318(12):747-52.
33. Mantovani A, Sica A, Sozzani S, Allavena P, Vecchi A, Locati M. The chemokine system in diverse forms of macrophage activation and polarization. Trends in Immunology. 2004;25(12):677-86.
34. Stout RD, Jiang C, Matta B, Tietzel I, Watkins SK, Suttles J. Macrophages sequentially change their functional phenotype in response to changes in microenvironmental influences. The Journal of Immunology. 2005;175(1):342-9.

35. Badylak SF, Valentin JE, Ravindra AK, McCabe GP, Stewart-Akers AM. Macrophage phenotype as a determinant of biologic scaffold remodeling. Tissue Engineering Part A. 2008;14(11):1835-42.
36. Madden LR, Mortisen DJ, Sussman EM, Dupras SK, Fugate JA, Cuy JL, et al. Proangiogenic scaffolds as functional templates for cardiac tissue engineering. Proceedings of the National Academy of Sciences. 2010.
37. Marshall A, Irvin C, Barker T, Sage E, Hauch K, Ratner BD. Biomaterials with tightly controlled pore size that promote vascular in-growth. Polymer Preprints. 2004;45:100-1.
38. Fukano Y, Usui ML, Underwood RA, Isenhath S, Marshall AJ, Hauch KD, et al. Epidermal and dermal integration into sphere-templated porous poly(2-hydroxyethyl methacrylate) implants in mice. Journal of Biomedical Materials Research Part A. 2010;94A(4):1172-86.
39. Sanders JE, Baker AB, Golledge SL. Control of in vivo microvessel ingrowth by modulation of biomaterial local architecture and chemistry. Journal of Biomedical Materials Research. 2002;60(1):36-43.
40. Isenberg BC, Williams C, Tranquillo RT. Small-diameter artificial arteries engineered in vitro. Circulation Research. 2006;98(1):25-35.
41. Conte MS. The ideal small arterial substitute: a search for the Holy Grail? The FASEB Journal. 1998;12(1):43-5.
42. Hoenig MR, Campbell GR, Rolfe BE, Campbell JH. Tissue-engineered blood vessels: alternative to autologous grafts? Arteriosclerosis, Thrombosis, and Vascular Biology. 2005;25(6):1128-34.
43. Kaushal S, Amiel GE, Guleserian KJ, Shapira OM, Perry T, Sutherland FW, et al. Functional small-diameter neovessels created using endothelial progenitor cells expanded ex vivo. Nat Med. 2001;7(9):1035-40.
44. Gui L, Muto A, Chan SA, Breuer CK, Niklason LE. Development of decellularized human umbilical arteries as small-diameter vascular grafts. Tissue Eng Part A. 2009;15(9):2665-76.
45. Dahl SLM, Kypson AP, Lawson JH, Blum JL, Strader JT, Li Y, et al. Readily available tissue-engineered vascular grafts. Science Translational Medicine. 2011;3(68):68ra9-ra9.
46. Hashi CK, Zhu Y, Yang G-Y, Young WL, Hsiao BS, Wang K, et al. Antithrombogenic property of bone marrow mesenchymal stem cells in nanofibrous vascular grafts. Proceedings of the National Academy of Sciences. 2007;104(29):11915-20.
47. Yu J, Wang A, Tang Z, Henry J, Li-Ping Lee B, Zhu Y, et al. The effect of stromal cell-derived factor-1α/heparin coating of biodegradable vascular grafts on the recruitment of both endothelial and smooth muscle progenitor cells for accelerated regeneration. Biomaterials. 2012;33(32):8062-74.
48. Li S, Sengupta D, Chien S. Vascular tissue engineering: from in vitro to in situ. Wiley Interdisciplinary Reviews: Systems Biology and Medicine. 2014;6(1):61-76.
49. Liang D, Hsiao BS, Chu B. Functional electrospun nanofibrous scaffolds for biomedical applications. Advanced Drug Delivery Reviews. 2007;59(14):1392-412.

50. Doshi J, Reneker DH. Electrospinning process and applications of electrospun fibers. Journal of Electrostatics. 1995;35(2–3):151-60.
51. Reneker DH, Chun I. Nanometre diameter fibres of polymer, produced by electrospinning. Nanotechnology. 1996;7(3):216.
52. Barnes CP, Sell SA, Boland ED, Simpson DG, Bowlin GL. Nanofiber technology: Designing the next generation of tissue engineering scaffolds. Advanced Drug Delivery Reviews. 2007;59(14):1413-33.
53. Tsou DA-C, Li S. Engineering microenvironments to control stem cell functions. Emerging Technology Platforms for Stem Cells: John Wiley & Sons, Inc.; 2009. p. 311-26.
54. Huang Z-M, Zhang YZ, Kotaki M, Ramakrishna S. A review on polymer nanofibers by electrospinning and their applications in nanocomposites. Composites Science and Technology. 2003;63(15):2223-53.
55. Ramakrishna S, Fujihara K, Teo W, Lim T, Ma Z. An introduction to electrospinning and nanofibers. Singapore: World Scientific; 2005.
56. Bhardwaj N, Kundu SC. Electrospinning: a fascinating fiber fabrication technique. Biotechnology Advances. 2010;28(3):325-47.
57. Khil M-S, Bhattarai SR, Kim H-Y, Kim S-Z, Lee K-H. Novel fabricated matrix via electrospinning for tissue engineering. Journal of Biomedical Materials Research Part B: Applied Biomaterials. 2005;72B(1):117-24.
58. Ma Z, Kotaki M, Inai R, Ramakrishna S. Potential of nanofiber matrix as tissue-engineering scaffolds. Tissue Eng. 2005;11(1-2):101-9.
59. Derby B. Printing and prototyping of tissues and scaffolds. Science. 2012;338(6109):921-6.
60. Lee M, Kim H-Y. Toward nanoscale three-dimensional printing: nanowalls built of electrospun nanofibers. Langmuir. 2014;30(5):1210-4.
61. Baker BM, Gee AO, Metter RB, Nathan AS, Marklein RA, Burdick JA, et al. The potential to improve cell infiltration in composite fiber-aligned electrospun scaffolds by the selective removal of sacrificial fibers. Biomaterials. 2008;29(15):2348-58.
62. Nam J, Huang Y, Agarwal S, Lannutti J. Improved cellular infiltration in electrospun fiber via engineered porosity. Tissue Eng. 2007;13(9):2249-57.
63. Kim TG, Chung HJ, Park TG. Macroporous and nanofibrous hyaluronic acid/collagen hybrid scaffold fabricated by concurrent electrospinning and deposition/leaching of salt particles. Acta Biomaterialia. 2008;4(6):1611-9.
64. Thorvaldsson A, Stenhamre H, Gatenholm P, Walkenström P. Electrospinning of highly porous scaffolds for cartilage regeneration. Biomacromolecules. 2008;9(3):1044-9.
65. Soliman S, Sant S, Nichol JW, Khabiry M, Traversa E, Khademhosseini A. Controlling the porosity of fibrous scaffolds by modulating the fiber diameter and packing density. Journal of Biomedical Materials Research Part A. 2011;96A(3):566-74.
66. Cheng Q, Lee BLP, Komvopoulos K, Li S. Engineering the microstructure of electrospun fibrous scaffolds by microtopography. Biomacromolecules. 2013;14(5):1349-60.

67. Yixiang D, Yong T, Liao S, Chan C, Ramakrishna S. Degradation of electrospun nanofiber scaffold by short wave length ultraviolet radiation treatment and its potential applications in tissue engineering. Tissue Eng Part A. 2008;14(8):1321-9.
68. Lee BL-P, Jeon H, Wang A, Yan Z, Yu J, Grigoropoulos C, et al. Femtosecond laser ablation enhances cell infiltration into three-dimensional electrospun scaffolds. Acta Biomaterialia. 2012;8(7):2648-58.
69. Duan Y, Wang Z, Yan W, Wang S, Zhang S, Jia J. Preparation of collagen-coated electrospun nanofibers by remote plasma treatment and their biological properties. J Biomater Sci Polym Ed. 2007;18(9):1153-64.
70. Cheng Q, Lee BL-P, Komvopoulos K, Yan Z, Li S. Plasma surface chemical treatment of electrospun poly(L-lactide) microfibrous scaffolds for enhanced cell adhesion, growth, and infiltration. Tissue Eng Part A. 2013;19(9-10):1188-98.
71. Zhu Y, Leong MF, Ong WF, Chan-Park MB, Chian KS. Esophageal epithelium regeneration on fibronectin grafted poly(l-lactide-co-caprolactone) (PLLC) nanofiber scaffold. Biomaterials. 2007;28(5):861-8.
72. Koh HS, Yong T, Chan CK, Ramakrishna S. Enhancement of neurite outgrowth using nano-structured scaffolds coupled with laminin. Biomaterials. 2008;29(26):3574-82.
73. Shin YM, Lee YB, Kim SJ, Kang JK, Park J-C, Jang W, et al. Mussel-inspired immobilization of vascular endothelial growth factor (VEGF) for enhanced endothelialization of vascular grafts. Biomacromolecules. 2012;13(7):2020-8.
74. Chew SY, Hufnagel TC, Lim CT, Leong KW. Mechanical properties of single electrospun drug-encapsulated nanofibres. Nanotechnology. 2006;17(15):3880.
75. Luong-Van E, Grøndahl L, Chua KN, Leong KW, Nurcombe V, Cool SM. Controlled release of heparin from poly(ε-caprolactone) electrospun fibers. Biomaterials. 2006;27(9):2042-50.
76. Zhang YZ, Wang X, Feng Y, Li J, Lim CT, Ramakrishna S. Coaxial electrospinning of (fluorescein isothiocyanate-conjugated bovine serum albumin)-encapsulated poly(ε-caprolactone) nanofibers for sustained release. Biomacromolecules. 2006;7(4):1049-57.

CHAPTER 2

Femtosecond Laser Ablation Enhances Cell Infiltration into Three-Dimensional Electrospun Scaffolds

ABSTRACT

Electrospun scaffolds are used extensively in tissue engineering applications since they offer a cell-friendly microenvironment. However, one major limitation is the dense fibers, small pore size and consequently poor cell infiltration. Here, we employ a femtosecond (FS) laser system to ablate and create microscale features on electrospun poly(L-lactide) (PLLA) nanofibrous scaffolds. Upon determining the ablation parameters, we pattern structured holes of varying diameters of 50, 100, and 200 μm and spacing of 50 and 200 μm between adjacent holes on the scaffolds. The elastic moduli of ablated scaffolds decrease with the decrease of spacing and the increase of hole size. Cells seeded on the laser-ablated scaffolds exhibit different morphology but similar proliferation rate when compared with control (non-ablated) scaffold. Furthermore, animal studies indicate that ablated scaffolds facilitate endothelial cell ingrowth as well as drastically increase M2 macrophage and overall cell infiltration. These findings demonstrate that FS laser ablation can be used to increase cell infiltration into nanofibrous scaffolds. Laser ablation not only can create desired features in micrometer length scale but also presents a new approach in the fabrication of three-dimensional porous constructs for tissue engineering.

Introduction

Biocompatible three-dimensional scaffolds play a pivotal role in tissue engineering. These scaffolds are fabricated with controlled mechanical and biological properties so that they are able to support new tissue formation while providing physical and chemical cues that promote various cellular processes, including proliferation, migration, and differentiation [1]. Specifically, the architecture of tissue-engineered scaffolds is designed to closely mimic the organized structure and biological function of native extracellular matrix (ECM). Thus, a favorable ECM-like microenvironment for cells is crucial to achieve the desirable scaffold integration as well as cell-material interactions and tissue ingrowth.

Electrospinning is a popular technique used to fabricate tissue-engineered scaffolds [2-5]. It is a consistent, versatile method that produces nonwoven, three-dimensional fiber structures with controllable fiber diameter [6-8]. Electrospun scaffolds have great potential in that their structures, especially in nanoscale network, not only closely resemble natural ECM but also exhibit high surface-area-to-volume ratio favorable for attachment of cells and bioactive molecules onto fiber surfaces [9]. However, one main issue that limits their utilization is their small pore size. Such small pore size of electrospun scaffolds results from the dense network of fibers, which hinders cell infiltration and ultimately reduces their use in replacing large tissues that require ample vascularization and nutrient diffusion. Various techniques to overcome this shortcoming have been investigated, including the incorporation of sacrificial fibers and porogens [10, 11], modification of fiber diameter [12], and post-processing by photopatterning [13] or ultraviolet radiation treatment [14] to increase pore size and overall porosity.

Although laser machining is an attractive approach for many biomedical applications, a major concern with using this method to process biomaterial scaffolds is the potential for thermal effects, for example, induced by nanosecond laser. However, ultrafast laser is considered a promising tool to rapidly process and create complex structures on electrospun scaffolds. For example, although a few studies have investigated the use of femtosecond (FS) laser to ablate electrospun fibrous scaffolds since its ultrashort and high irradiance pulses produce clean ablation with minimal thermal and physical stress [15, 16], they focus primarily on surface ablations, such as grooves and microwells, which did not address the pore size issue of electrospun scaffolds, and there was limited biological characterization. In addition, key features that make FS laser processing superior over other laser machining processing, such as nanosecond or picosecond laser, lie primarily in its very rapid creation of vapor and plasma phases that lead to negligible heat conduction and the absence of liquid phase [17]. Thus, FS laser possesses the ability for precise material processing with clean surface and reduced thermal damage, whereas UV nanosecond laser ablation leads to redeposition of the material and results in melted morphology and decreased porosity [18, 19]. In fact, the level of precision in which the location and depth of well-defined ablation can be carefully regulated further facilitates the process.

Here, we explore the potential of FS laser ablation to create desired microscale topographical features and increase both pore size and bulk porosity of electrospun PLLA nanofibrous scaffolds. Using an 800 nm, 100 femtosecond (fs) laser to ablate the scaffolds, we determine optimal ablation parameters, characterize the process for patterning holes of varying diameters (50 μm, 100 μm, and 200 μm) and densities (50-μm and 200-μm spacing between adjacent holes), and compare the structure and mechanical property of the scaffolds. Furthermore, we assess the biocompatibility and biological performance of these ablated scaffolds to determine whether different extent of porosity from the patterned holes affect cell adhesion, morphology, and proliferation *in vitro*, along with cell infiltration and host response *in vivo*.

Materials and Methods

Fabrication of PLLA Nanofibrous Scaffolds

We used electrospinning, as described previously with minor modifications [20, 21], to fabricate nanofibrous scaffolds from biodegradable poly(L-lactide) (PLLA) (1.09 dL/g inherent viscosity) (Lactel Absorbable Polymers, Pelham, AL). The PLLA (19% w/v) solution was prepared by dissolving PLLA pellets in hexafluoroisopropanol (HFIP) solvent via sonication for 30 minutes until all of the PLLA pellets were completely dissolved. To deliver the polymer solution, a programmable pump was used along with a 5-ml syringe filled with PLLA that was fitted with flexible silicon tubing connected to 1.5" long stainless steel 23G dispensing needles. A high-voltage generator was used to apply a 12 kV voltage to the needle. PLLA fibers with diameters ranging from 200 nm to 3 μm were ejected from the charged needle towards the surface of a grounded collector to form a nonwoven nanofibrous membrane. Specifically, the PLLA solution was delivered at a flow rate of 1 ml/hr from a gap distance (distance between needle tip and collecting drum) of 8.5 cm. For this study, a random orientation of nanofibers was achieved by using a low speed of rotation (200 rpm) for the collecting drum. Electrospinning continued until the scaffolds reached an approximate thickness of 130-200 μm based on measurements with a thickness gauge (Mitutoyo America, Aurora, IL). The electrospun sheets were then placed in a vacuum overnight to remove any residual HFIP.

Femtosecond Laser Ablation and Characterization of Ablated Nanofibrous Scaffolds

The ablation characteristics of PLLA scaffold were evaluated to determine the optimal parameters for creating the desired ablations. We used a Ti:Sapphire amplified laser system (Spitfire, Spectra physics, Irvine, CA) and 5x objective lens with numerical aperture N.A. = 0.14 (M Plan Apo, Mitutoyo, Barrington, NJ) to perform FS laser ablation. First, using single pulses of the FS laser, we varied the laser energy and observed the corresponding change in ablation pore size. The pulse energy was adjusted

with a half wave plate (λ/2) and a polarizing beam splitter. Samples were loaded on motorized stages (ANT130, Aerotech Inc., Pittsburgh, PA) with a synchronized laser trigger system controlled by a personal computer. Subsequently, using constant laser energy (35 μJ), we varied the pulse number to determine the resulting change in depth of the ablation with increasing pulse number. The ablated scaffolds were examined and imaged from both top and cross-sectional views to compare changes in pore size and depth, respectively, with Hitachi TM-1000 scanning electron microscope (SEM) (Hitachi, Pleasanton, CA). For the samples used in *in vitro* and *in vivo* studies, through-holes were fabricated on the PLLA scaffolds by circular and linear motion of the motorized stages with 1 mm/s speed with fixed laser energy (35 μJ) and pulse frequency (1 kHz).

To determine the mechanical property of the nanofibrous scaffolds, scaffolds were first cut into approximately 0.5-cm x 1-cm pieces and subjected to uniaxial tensile testing in the longitudinal direction by using an Instron 5544 tester (Instron, Canton, MA). Prior to testing, three thickness measurements along the length of each sample were taken with the thickness gauge and averaged; likewise, three width measurements were acquired using a digital caliper and averaged. After placing the sample in between the grips, the gauge length was measured with a digital caliper. Each sample was extended until failure at a rate of 0.1 mm/sec, and the applied force and deformation were recorded every second via Bluehill software (Instron, Canton, MA). Elastic modulus was calculated by determining the slope based on the applied load and scaffold deformation in the linear region of the stress-strain curve and the dimensions (thickness and width) of the samples.

Cell Culture and In Vitro Cell Experiments

Human mesenchymal stem cells (hMSCs) (Lonza Walkersville, Walkersville, MD) were cultured and expanded in hMSC maintenance medium (MSCGM, Cambrex, East Rutherford, NJ) and maintained in a humidified incubator at 37ºC with 5% CO_2.

Scaffolds from the 7 groups of membranes ((1) control (non-ablated); (2) 50-μm diameter/50-μm spacing (50-50); (3) 50-μm diameter/200-μm spacing (50-200); (4) 100-μm diameter/50-μm spacing (100-50); (5) 100-μm diameter/200-μm spacing (100-200); (6) 200-μm diameter/50-μm spacing (200-50); and (7) 200-μm diameter/200-μm spacing (200-200)) were cut into 0.5-cm x 0.5-cm squares and secured to non-tissue-culture-treated polystyrene dishes via double-sided tape. Prior to cell seeding, these membranes were disinfected in 70% ethanol under germicidal ultraviolet light for 30 minutes, and subsequently washed with sterile deionized water for five times. The membranes were then coated with 1% fibronectin (Sigma-Aldrich, St. Louis, MO) for 30 minutes at 37ºC and washed once with PBS before cell seeding. Approximately 3,500 cells were seeded onto each of the membranes followed by 30 minutes of incubation to allow the cells to settle and attach. After incubation, sufficient media (Dulbecco's modified Eagle medium (DMEM) (Invitrogen, Carlsbad, CA) supplemented with 10% fetal bovine serum (FBS) (Thermo Fisher Scientific, Waltham, MA) and 1% penicillin/streptomycin (P/S) antibiotic mixture was added to each dish containing a cell-seeded membrane. To visualize cell adhesion and morphology, samples were fixed after 24 hours with 4% paraformaldehyde (PFA), permeabilized with 0.5% Triton X-100, blocked with 3 mg/ml bovine serum albumin (BSA) + 0.1% Triton X-100, and stained with AlexaFluor 488

phalloidin for actin filaments as previously described [22]. Fluorescence images of the stained hMSCs were obtained with a Zeiss confocal fluorescence microscope (Zeiss LSM710, Carl Zeiss MicroImaging, Thornwood, NY).

To quantify cell proliferation, samples were prepared as described above. Scaffolds were seeded with a lower density of approximately 1,000 hMSCs per scaffold, followed by 30 minutes of incubation for cells to settle and attach. After incubation, sufficient DMEM supplemented with 10% FBS and 1% P/S was added to each dish containing a cell-seeded membrane. The samples were fixed after 24 hours and subsequently immunostained for the proliferation marker Ki-67 (Abcam, Cambridge, MA) along with 4',6-diamidino-2-phenylindole (DAPI) for nuclear counterstain. Fluorescence images of the stained hMSCs were obtained with the Zeiss confocal fluorescence microscope. The percentage of cells that were in the active phases of cell cycle was determined and correlated to cell proliferation rate.

Rat Subcutaneous Cellular Infiltration Model

All experimental procedures with animals were approved by the ACUC committee at University of California, Berkeley. Three membranes, approximately 0.5-cm x 0.5-cm in size, representing each of the 7 groups were implanted in the subcutaneous cavity of Sprague-Dawley rats. Briefly, all membranes were disinfected in 70% ethanol under germicidal ultraviolet light for 30 minutes, and subsequently washed five times with sterile deionized water. Prior to scaffold implantation, rats were anesthetized with isofluorane, and the incision sites were marked and disinfected with 70% ethanol. Four incisions were made on the right side and three incisions on the left side of the lower abdominal wall so that one scaffold from each of the 7 groups was implanted and placed subcutaneously relative to the incision in the same rat. Interrupted 5-0 Monocryl (Ethicon, Inc., Somerville, NJ) mattress sutures were used to close the incision.

All animals were monitored daily by a veterinarian and no adverse incidents were observed in any of the animals. At the end of the 1-week study on day 7 and the 2-week study on day 14, the rats were returned to the operating room, where they were given general anesthesia and disinfected with 70% ethanol at the initial implantation locations. The scaffolds, along with their immediate surrounding tissue, were explanted and immediately fixed with 4% PFA before being embedded in optimal cutting temperature (OCT) compound (TissueTek, Elkhart, IN) on dry ice. Cross-sections of 12-um thickness were generated in the transverse plane using a -20ºC cryosectioner. The samples were fixed with 4% PFA, permeabilized with 0.5% Triton X-100, and blocked with 3 mg/ml BSA + 0.1% Triton X-100. They were then immunostained for pan macrophages using mouse anti-rat CD68 (AbD Serotec, Raleigh, NC) at 1:100 dilution; for M2 macrophages using mouse anti-rat CD163 (AbD Serotec) at 1:50 dilution; for M1 macrophages using rabbit anti-rat CCR7 (Novus Biologicals, Littleton, CO) at 1:100 dilution; and for endothelial cells using mouse anti-rat CD31 (BD Pharmingen, San Diego, CA) at 1:100 dilution. The secondary antibody used was AlexaFluor 488 donkey anti-mouse IgG (H+L) (Invitrogen Corp., Carlsbad, CA) for CD68 and CD31, AlexaFluor 546 donkey anti-mouse IgG (H+L) (Invitrogen Corp.) for CD163, and AlexaFluor 546 goat anti-

rabbit IgG (H+L) (Invitrogen Corp.) for CCR7, all at 1:500 dilution. All antibodies were diluted in blocking serum. All samples were subsequently counterstained with DAPI. Fluorescent signals were observed under the Zeiss LSM710 confocal microscope. A minimum of 6 cryosections were examined for each membrane to confirm the consistency between sections.

Statistical Analysis

The data are presented as mean $\pm$ standard deviation (SD). All data were compared by using one-way ANOVA tests. Two-tailed Student's t test was used to test for significant differences between the groups with the same hole diameter. Holm's t test was then used to perform multiple comparisons against a single control to determine significant differences between each ablated scaffold group and the control. A P value less than 0.05 was considered statistically significant.

Results and Discussion

Characterization of Femtosecond Laser-Ablated Nanofibrous Scaffolds

To characterize the ablation of electrospun PLLA scaffolds, the effects of varying laser energy and pulse number on ablated pore size and depth, respectively, were examined (Figure 2.1). Our plots show that the diameter of ablated pores increased logarithmically as laser energy increased (Figure 2.1G), and the resulting depth was linearly proportional to the pulse number (Figure 2.1H). With a 35 μJ FS laser, the average depths of ablated pores increased from about 21 to 130 μm as pulse increased from 1 to 8 pulses, with complete through-holes achieved beyond 8 pulses. We demonstrated that the scaffold material could be removed by layers in controllable amounts and that well-defined pore size and spacing could be easily produced in a rapid format. Applying the optimal parameters, we prepared a total of 7 groups of membranes: (1) control (non-ablated); (2) 50-μm diameter/50-μm spacing (50-50); (3) 50-μm diameter/200-μm spacing (50-200); (4) 100-μm diameter/50-μm spacing (100-50); (5) 100-μm diameter/200-μm spacing (100-200); (6) 200-μm diameter/50-μm spacing (200-50); and (7) 200-μm diameter/200-μm spacing (200-200).

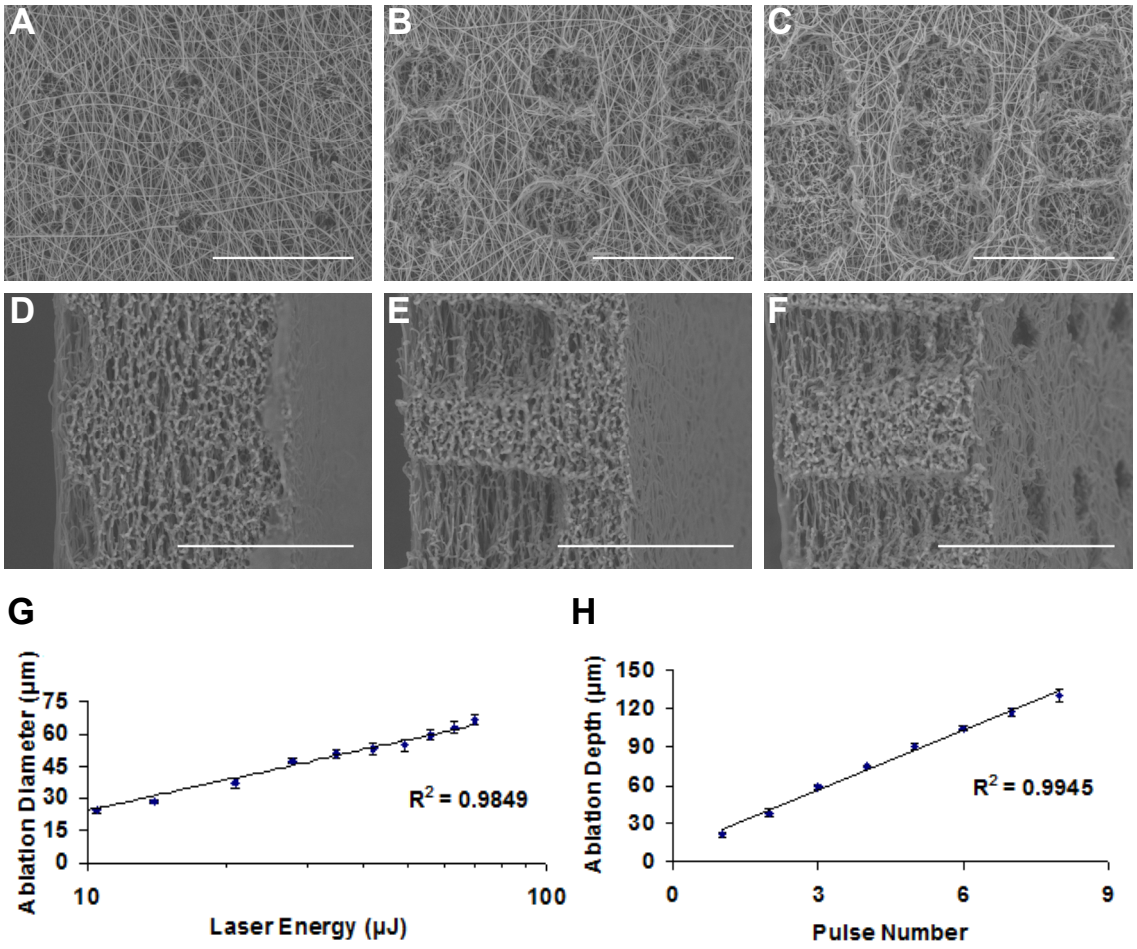

Figure 2.1. Characterization of femtosecond laser ablation of electrospun scaffolds. SEM images of PLLA nanofibrous scaffolds ablated with a single pulse of an 800 nm, 100 femtosecond laser with an energy of (A) 7 µJ, (B) 35 µJ, and (C) 70 µJ were taken to determine the resulting diameter of ablation. To characterize the ablation depth, SEM images of PLLA scaffolds ablated with (D) 1 pulse, (E) 5 pulses, and (F) 10 pulses of the same femtosecond laser with constant 35 µJ energy were taken. (G) Ablated diameter (µm) versus laser energy (µJ) for single-pulse ablation was plotted. (H) Ablated depth (µm) versus pulse number for a 35 µJ, femtosecond laser was plotted. Scale bar: 100 µm.

Our SEM visualization confirmed that FS laser ablation of electrospun scaffold resulted in minimal thermal stress and collateral damage (Figure 2.1A-F and Figure 2.2A-F). The PLLA fiber architecture, especially in regions immediately adjacent to the ablation site, did not reveal molten morphology. The ablated scaffolds maintained an overall intact fibrous structure and provided a more porous structure not only because of the patterned arrays of holes but more importantly the relatively larger pore sizes on the post-ablation edge compared to the pores on the scaffold surface. Thus, our findings suggest that the process of FS laser ablation can impart beneficial features in addition to patterned holes to electrospun scaffolds in order to not only increase pore size and

improve their bulk porosity but also provide the path for cell infiltration between layers of electrospun fibers.

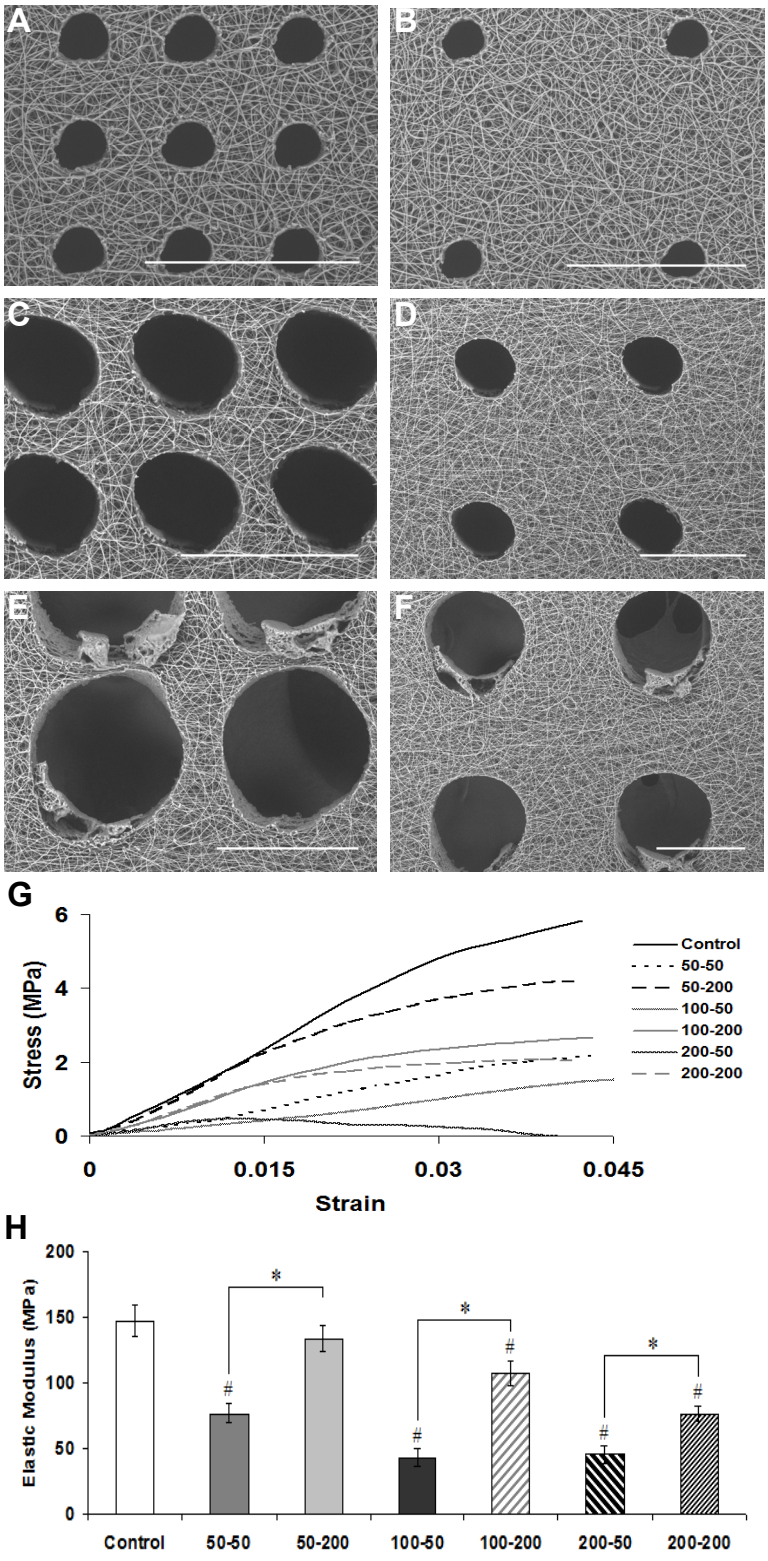

Figure 2.2. Characterization of FS laser-ablated nanofibrous scaffolds with varying hole size and density. Six groups of ablated scaffolds were prepared: (A) 50-µm diameter/50-µm spacing (50-50); (B) 50-µm diameter/200-µm spacing (50-200); (C) 100-µm diameter/50-µm spacing (100-50); (D) 100-µm diameter/200-µm spacing (100-200); (E) 200-µm diameter/50-µm spacing (200-50); and (F) 200-µm diameter/200-µm spacing (200-200). Scale bar: 200 µm. (G) Representative stress-strain curves of the control (non-ablated) scaffold and ablated scaffolds of 50-50 (red), 50-200 (orange), 100-50 (yellow), 100-200 (green), 200-50 (blue), and 200-200 (brown). (H) Elastic moduli were calculated from the slope of the curves and the scaffold dimensions for each group ($n \geq 4$). * indicates significant difference ($P<0.05$) between the pairs (same diameter, different spacing) of scaffold groups. # indicates significant difference ($P<0.05$) compared to the control group.

To assess the effect of laser-ablated hole size and density on the mechanical properties of the ablated scaffolds, we performed uniaxial tensile testing. Representative stress-strain plots of the samples tested for each scaffold group are shown (Figure 2.2G,H). The elastic moduli of the ablated scaffolds varied significantly from the control scaffold, and the decrease of the spacing between the holes had more dramatic effect on elastic modulus. Despite having the same hole density of 200-μm spacing with the two larger hole sizes, only the 50-200 group (133.8 $\pm$ 9.7 MPa) had comparable elastic modulus with that of control (147.2 $\pm$ 11.8 MPa); the 100-200 (107.4 $\pm$ 9.3 MPa) and 200-200 groups (76.8 $\pm$ 5.7 MPa) were significantly weaker as a consequence of the larger hole size. Because of the much higher density of ablated holes, the elastic moduli of the 50-μm spacing groups were decreased by approximately 2 to 2.5-fold compared to their respective 200-μm spacing counterparts (76.9 $\pm$ 7.3 MPa for 50-50; 42.9 $\pm$ 7.0 MPa for 100-50; 45.1 $\pm$ 6.9 MPa for 200-50). We believe that the presence of holes changed the stress distribution and thus decreased the strength of the scaffolds. Therefore, the range of the apparent elastic moduli of the ablated scaffolds may be tailored for specific tissue engineering applications.

Effects of Laser-Ablated Hole Size and Density on Cell Adhesion, Morphology and Proliferation

Previous studies have shown that the structuring of scaffold surfaces with topological microscale features affect cellular behaviors and provide directed tissue development [23, 24]. In our study, we stained for actin and Ki-67 (a proliferation marker) to visualize the morphology and assess the proliferation of hMSCs on the ablated and control scaffolds after 1-day culture. As shown in Figure 2.3A-G, cell adhesion on the surface of ablated scaffolds appeared unaffected as no drastic difference in cell density was observed. However, cell morphology on the ablated scaffolds was influenced by the hole size and density. On the two 50-μm diameter groups, hMSCs exhibited similar well-spread morphology compared to the cells on the control scaffold as they easily concealed the patterned holes as if no features were present (Figure 2.3B,C). As the hole size increased to 100 μm and 200 μm in diameter, the cells became more elongated with fewer cells bridging across the holes while most adhered and circumferentially aligned around the ablated holes. This difference in cell morphology was more defined for the 100-50 and 200-50 groups since the cells were more spatially confined within the constrained area as a result of the combination of larger hole size and higher hole density. In contrast, although the ablated holes altered cell morphology, our results indicated that hMSC proliferation on the surface of ablated scaffolds appeared unaffected by the varying hole sizes and densities as no considerable difference was observed (Figure 2.3H). Thus, our findings showed that although hMSC adhesion and proliferation on the scaffold surface were not significantly affected, their morphology was dictated by the patterned hole features.

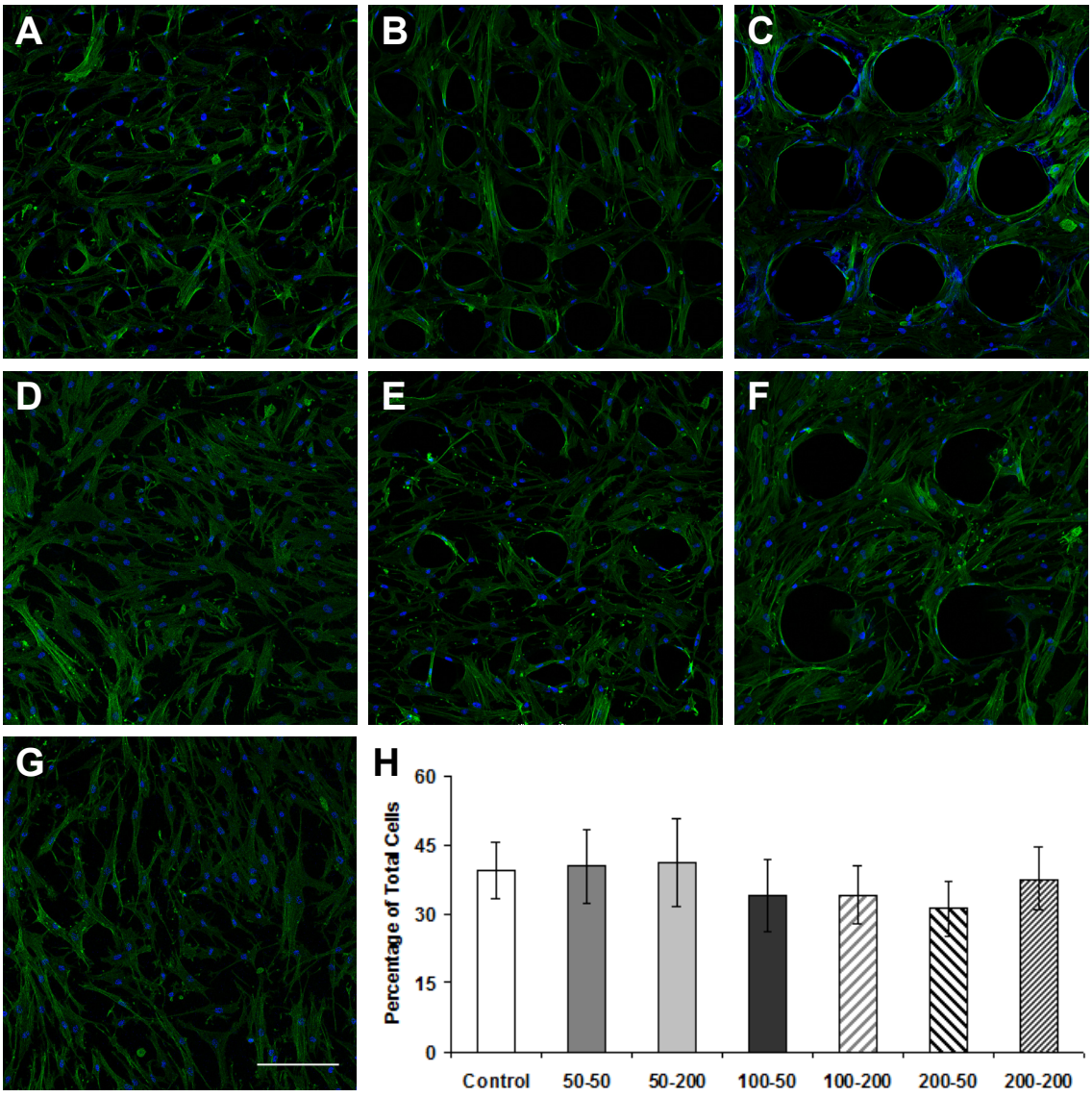

Figure 2.3. Cell adhesion, morphology, and proliferation on nanofibrous scaffolds. hMSCs were seeded onto the ablated scaffolds of (A) 50-50; (B) 100-50; (C) 200-50; (D) 50-200; (E) 100-200; (F) 200-200; and (G) control (non-ablated) scaffold. Cells were fixed after 24h and stained with AlexaFluor 488 phalloidin for actin (green) and DAPI (blue) for cell nucleus. Scale bar: 200 μm. (H) Quantitative analysis showing the percentage of cells positive for Ki-67 on each scaffold group (n=3).

Effects of Laser-Ablated Holes on Cell Infiltration and Host Response In Vivo

In order to better characterize the biological response to the microscale hole features, we demonstrated through our rat subcutaneous cell infiltration model that effective cell infiltration into electrospun scaffolds *in vivo* could be achieved and

significantly enhanced by utilizing a FS laser system to create desired ablations and increase scaffold porosity. Here, scaffolds were implanted subcutaneously between the superficial fascia and the contacting muscular layer in the lower abdominal region of Sprague-Dawley (SD) rats. The scaffolds were explanted after 1 week, and cross-sections were obtained and immunostained with anti-CD68 antibody for pan macrophages as well as anti-CD163 and anti-CCR7 antibodies for M2 and M1 phenotype of macrophages, respectively, to assess the extent of immunomodulatory response, and with DAPI to visualize the distribution of infiltrated cells throughout the thickness of the scaffolds (Figures 2.4-2.6). CD68 is a pan-macrophage marker; CD163 is a surface marker representative of the M2 phenotype of macrophages, which have been characterized as the anti-inflammatory, "alternatively" activated macrophages that promote immunoregulation, tissue repair, and constructive tissue remodeling; CCR7 is a surface marker representative of the M1 phenotype of macrophages, which have been characterized as the pro-inflammatory, "classically" activated macrophages associated with signs of inflammation [25-27]. Our results showed that $CD68^+$ macrophages were present in the surrounding and infiltrated cells for all 6 ablated scaffold groups, with $CD163^+$ M2 macrophages contributing to a large portion of the population. (Figure 2.4A-G and Figure 2.5). However, no drastic differences in the presence of $CCR7^+$ M1 macrophages were observed in the surrounding population of cells for all 7 scaffold groups (Figure 2.6). In addition, because of the poor cell infiltration into and the low number of cells throughout the control compared to the ablated scaffolds (as indicated by DAPI staining and Figure 2.4H), very few $CD68^+$ macrophages, including $CCR7^+$ M1 macrophages, and no $CD163^+$ M2 macrophages were found within the control scaffold. Several recent studies demonstrated that porosity of biomaterial scaffold is important in that porous materials, compared to their non-porous form, healed with minimal foreign body reaction (FBR) and fibrosis when implanted *in vivo* [28-30]. Interestingly, pores of optimal size were found to be heavily infiltrated by high ratio of M2/M1 macrophages [30]. Therefore, although the exact mechanisms in which the ablations timely modulate the macrophage phenotype remain unknown, the presence of $CD68^+$ macrophages, more specifically $CD163^+$ M2 macrophages, in ablated regions as well as within and surrounding our ablated scaffolds suggests the importance of microscale pores and their contribution to cell ingrowth and biological scaffold remodeling.

In addition, in Figure 2.4H, cell infiltration, as determined by cell density (cells/mm^2), into both scaffold and hole regions for the different scaffold groups was quantified. Because host tissue was able to grow into the ablations, we noticed significantly higher cell infiltration in the holes regions compared to the scaffold regions for every scaffold group except the 200-200 group. More importantly, cell infiltration was significantly higher in the scaffold regions of ablated scaffolds compared to the control scaffold. We speculate that the ablations facilitated overall cell infiltration as the cells were able to better migrate through the ablated holes and infiltrate between layers of electrospun fibers into the scaffold from the post-ablation edges rather than from the relatively less porous surface.

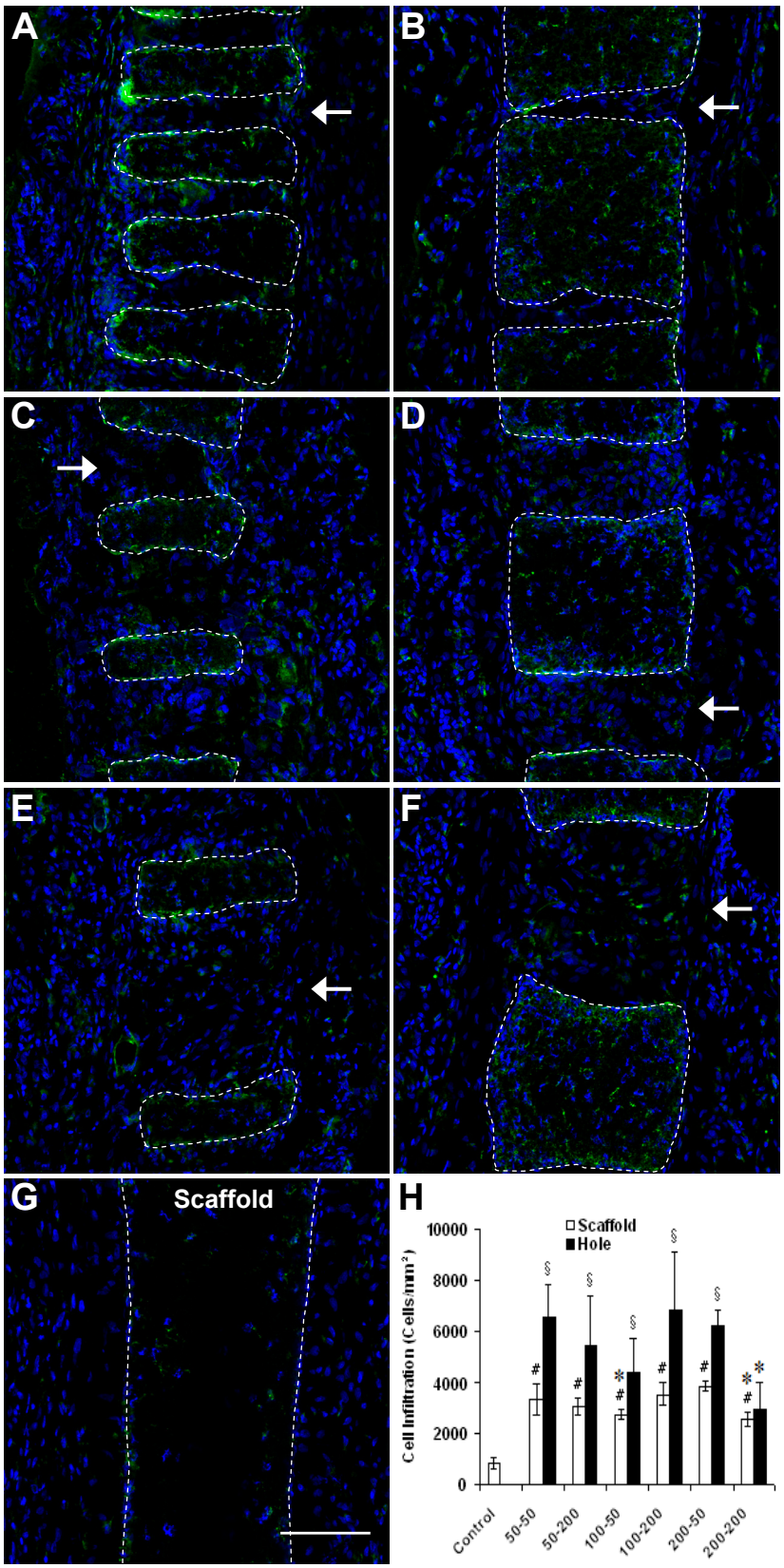

Figure 2.4. Pan-macrophage recruitment and infiltration into nanofibrous scaffolds in vivo after 1 week. Immunofluorescent staining of CD68 (green) for pan macrophages and counterstain with DAPI (blue) for cell nuclei of infiltrated and surrounding cells in the cross-sections of the ablated scaffolds of (A) 50-50; (B) 50-200; (C) 100-50; (D) 100-200; (E) 200-50; (F) 200-200; and (G) control (non-ablated) scaffold. White arrows indicate the location of the holes. Edges of the scaffolds are delineated by the white dashed lines. Scale bar: 100 μm. (H) Quantitative analysis showing general cell infiltration (in cells/mm^2) into the scaffold and hole regions of the different scaffold groups (n=3). # indicates significant difference (P<0.05) compared to the control group. * indicates significant difference (P<0.05) between the pairs (same diameter, different spacing) of scaffold groups. § indicates significant difference (P<0.05) between the scaffold and hole regions within each scaffold group.

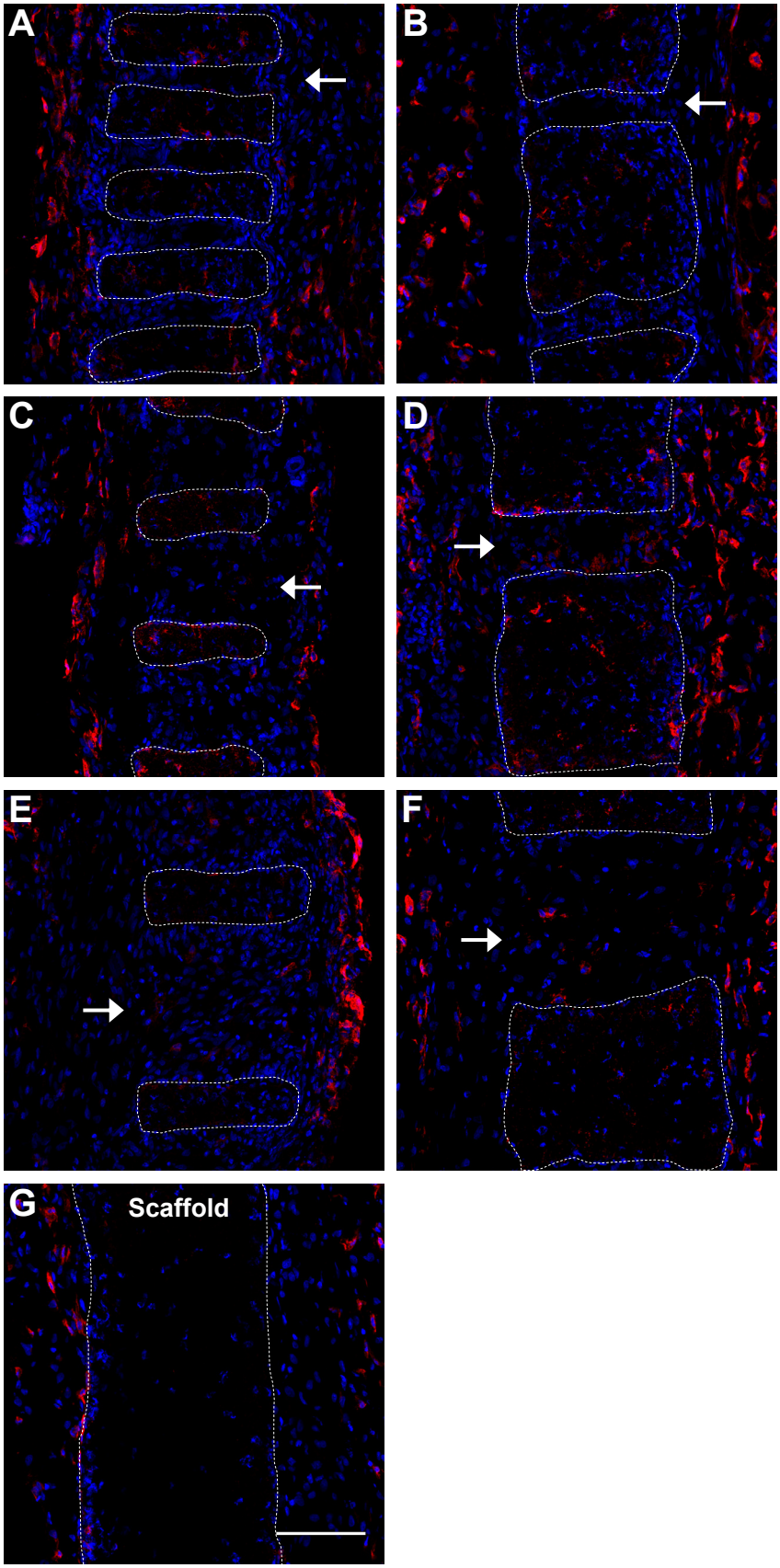

Figure 2.5. M2 macrophage recruitment and infiltration into nanofibrous scaffolds in vivo after 1 week. Immunofluorescent staining of CD163 (red) for M2 phenotype macrophages and counterstain with DAPI (blue) for cell nuclei of infiltrated and surrounding cells in the cross-sections of the ablated scaffolds of (A) 50-50; (B) 50-200; (C) 100-50; (D) 100-200; (E) 200-50; (F) 200-200; and (G) control (non-ablated) scaffold. White arrows indicate the location of the holes. Edges of the scaffolds are delineated by the white dashed lines. Scale bar: 100 μm.

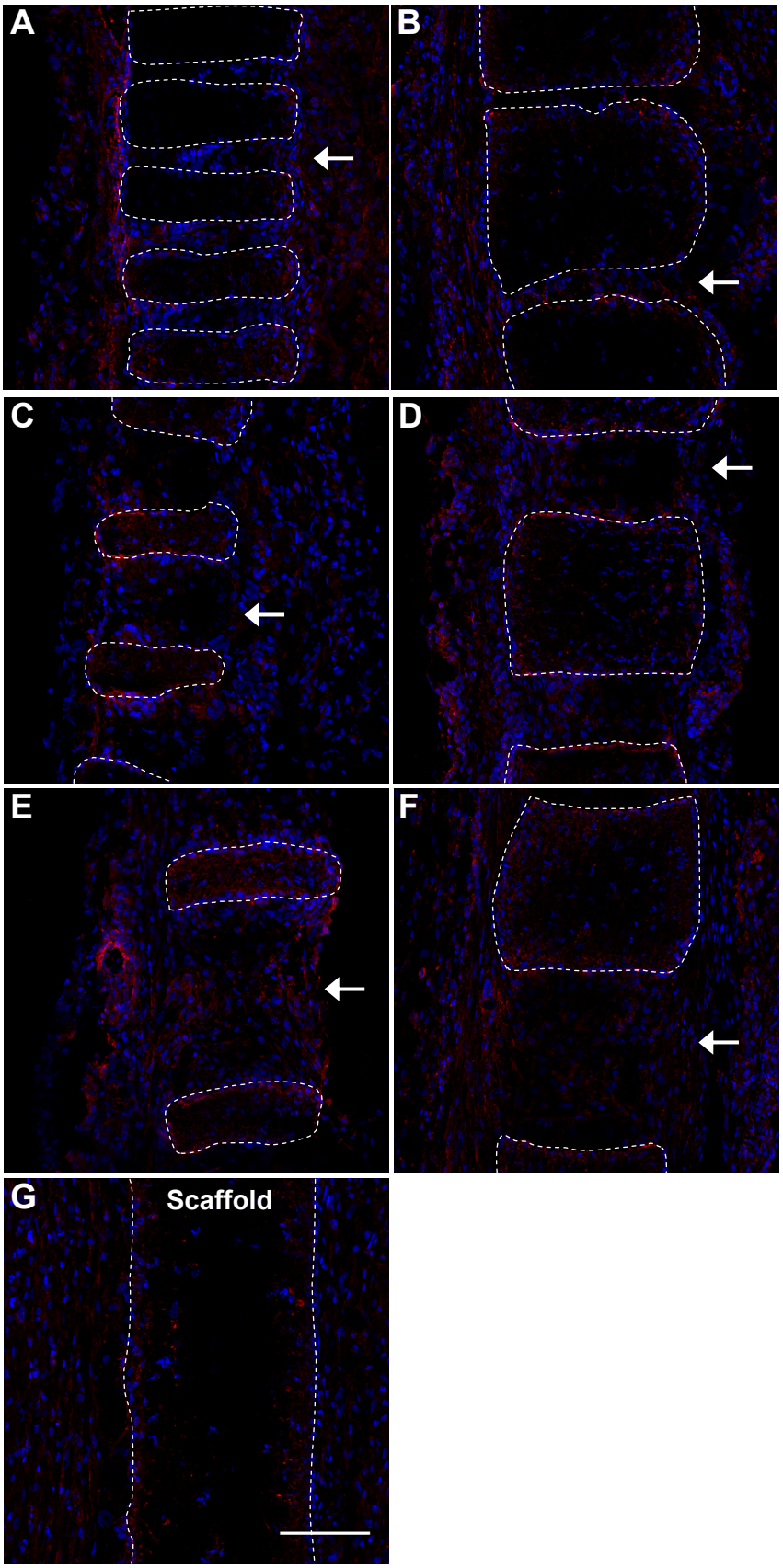

Figure 2.6. M1 macrophage infiltration into nanofibrous scaffolds in vivo after 1 week. Immunofluorescent staining of CCR7 (red) for M1 phenotype macrophages and counterstain with DAPI (blue) for cell nuclei of infiltrated and surrounding cells in the cross-sections of the ablated scaffolds of (A) 50-50; (B) 50-200; (C) 100-50; (D) 100-200; (E) 200-50; (F) 200-200; and (G) control (non-ablated) scaffold. White arrows indicate the location of the holes. Edges of the scaffolds are delineated by the white dashed lines. Scale bar: 100 μm.

Furthermore, we observed a noticeable increase in endothelial cell ingrowth of the ablated scaffolds implanted subcutaneously in the lower abdominal region of SD rats. In a study aimed to elucidate the effects of pore size on tissue response to porous biomaterials, Marshall et al. showed that tightly controlled pore size promoted vascular ingrowth in which the degree of intra-matrix vascularization increased with decreasing pore size [31]. However, as shown in Figure 2.7, our $CD31^+$ staining indicated endothelial cell infiltration within the ablated holes after 1 week *in vivo*. In addition, the extent of endothelial cell ingrowth with respect to increased $CD31^+$ staining within the holes of the ablated scaffolds was more prominent after 2 weeks *in vivo* (Figure 2.8). This is suggestive of angiogenesis as endothelial cells were able to migrate into the holes to sprout new blood vessels. In contrast, regions without ablations, such as the spacing between adjacent holes as well as the control scaffold, showed no signs of endothelial cells within the scaffolds; instead, the distribution of $CD31^+$ staining was concentrated mainly in the surrounding tissue. These findings concur with previous studies that specifically engineered pore size is pro-angiogenic and can potentially induce more vascularization [32], although additional studies need to be conducted to investigate and better understand the process.

Thus, because this approach can be not only extended to various polymers that may have different effects on inflammatory responses but also combined with other techniques such as the incorporation of sacrificial fibers in composite scaffolds, the appropriate selection of polymers or matrix proteins for fabricating electrospun scaffolds is important and needs to be customized for various tissue engineering and regenerative medicine applications.

Conclusions

In summary, porosity is an important issue that must be addressed when utilizing electrospun meshes as tissue-engineered nanofibrous scaffolds. Here, we demonstrate that FS laser can be used to ablate electrospun scaffolds while preserving their overall structural integrity and effectively improving cell infiltration. FS laser allows better control of laser power than nanosecond laser and avoids fiber melting and consequently the blockage of porous structure. The diameter of the holes increases logarithmically with the laser energy, and the depth of the holes increases linearly with the number of the laser pulse. In addition to their effects on cell morphology *in vitro*, electrospun PLLA scaffolds with FS laser-ablated holes of varying size and density exhibit significantly better endothelial cell ingrowth and macrophage infiltration compared to the control scaffold *in vivo*. We hope to integrate the FS laser system with tissue engineering applications to not only promote cell ingrowth and accelerate tissue remodeling but also enhance the vascularization of engineered tissues, the fabrication of 3D structures, and the control of topographical features in the cellular microenvironment.

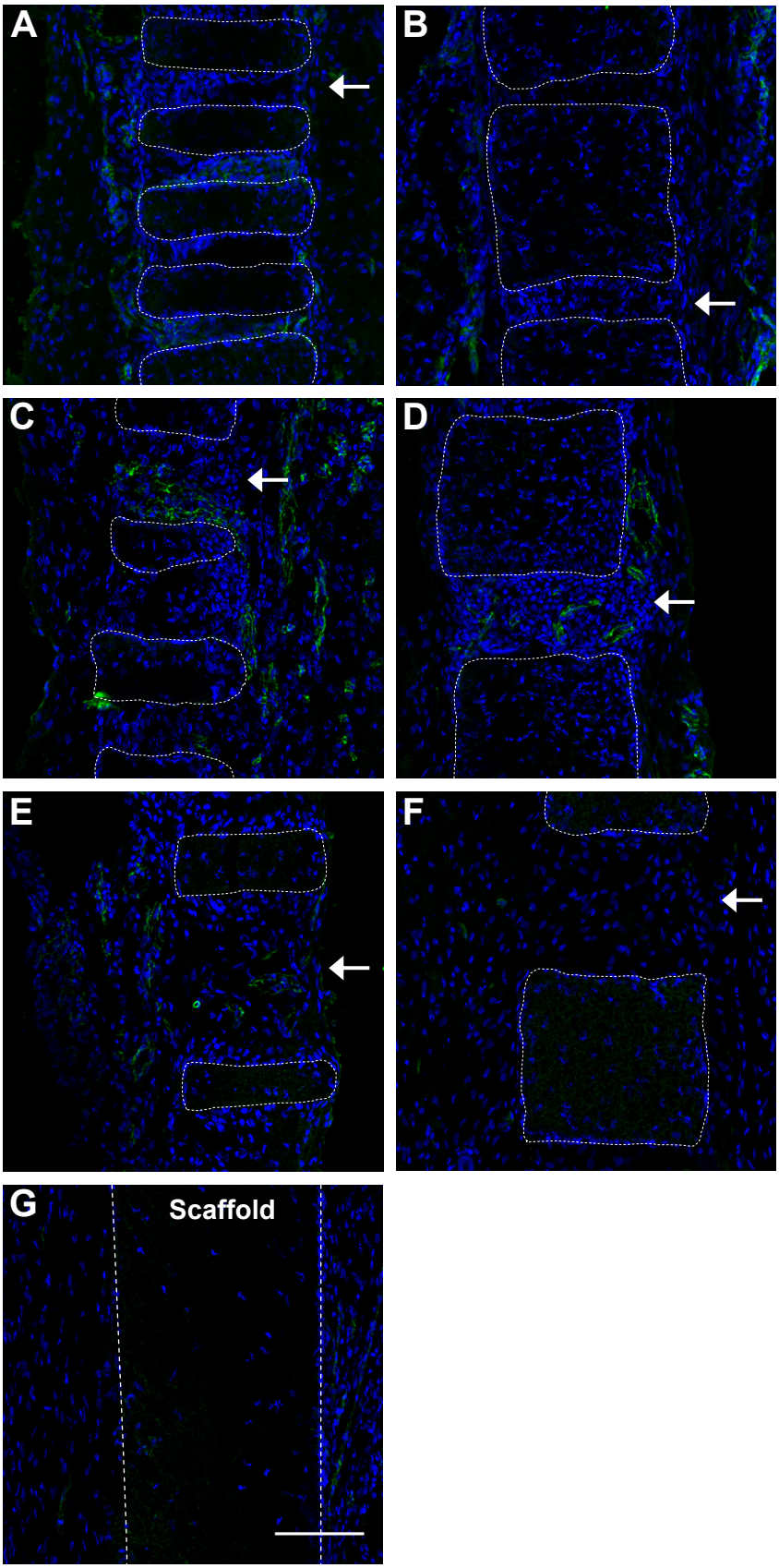

Figure 2.7. Endothelial cell infiltration into nanofibrous scaffolds in vivo after 1 week. Immunofluorescent staining of CD31 (green) for endothelial cells and counterstain with DAPI (blue) for cell nuclei of infiltrated and surrounding cells in the cross-sections of the ablated scaffolds of (A) 50-50; (B) 50-200; (C) 100-50; (D) 100-200; (E) 200-50; (F) 200-200; and (G) control (non-ablated) scaffold. White arrows indicate the location of the holes. Edges of the scaffolds are delineated by the white dashed lines. Scale bar: 100 μm.

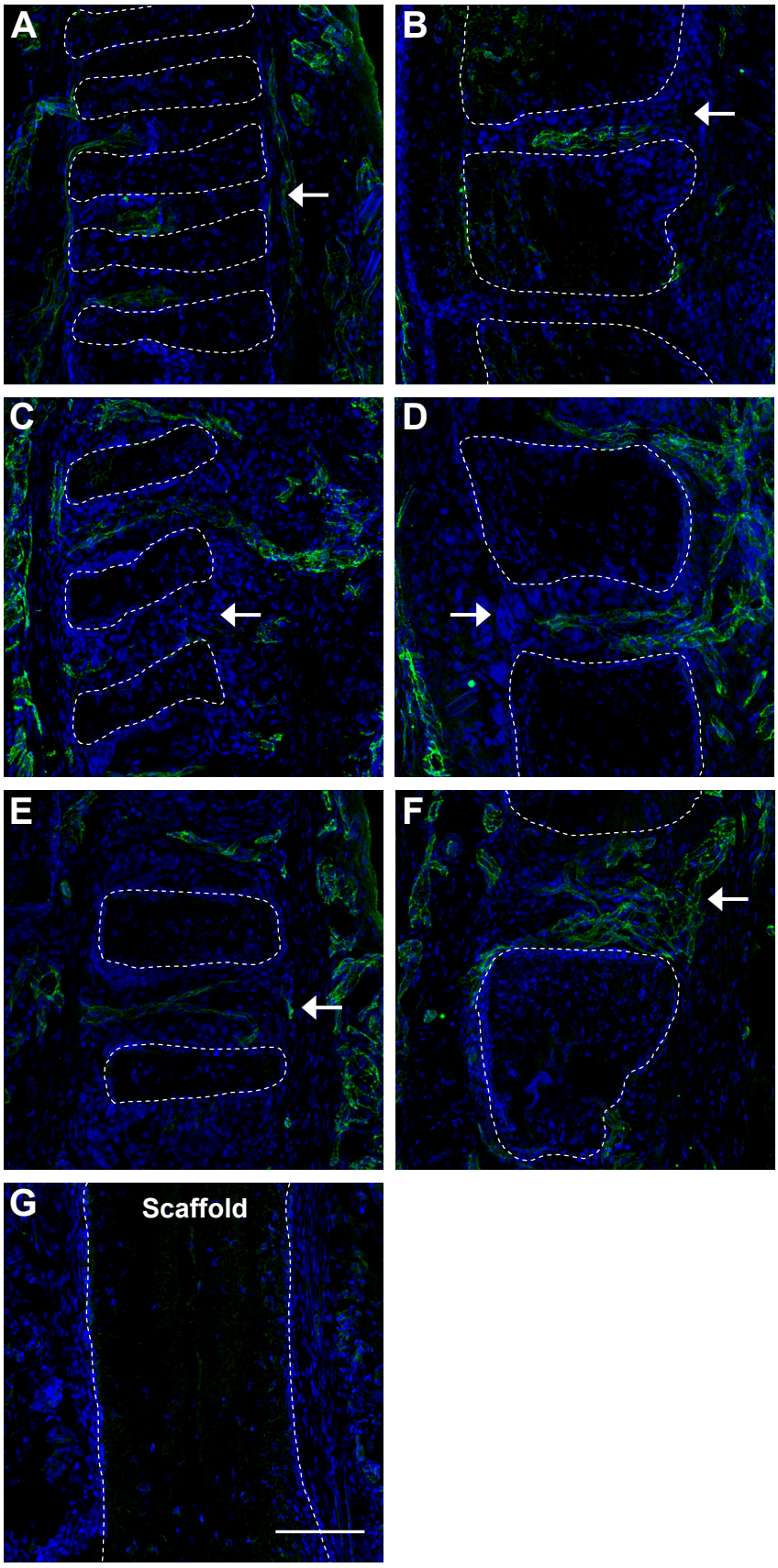

Figure 2.8. Endothelial cell infiltration into nanofibrous scaffolds in vivo after 2 weeks. Immunofluorescent staining of CD31 (green) for endothelial cells and counterstain with DAPI (blue) for cell nuclei of infiltrated and surrounding cells in the cross-sections of the ablated scaffolds of (A) 50-50; (B) 50-200; (C) 100-50; (D) 100-200; (E) 200-50; (F) 200-200; and (G) control (non-ablated) scaffold. White arrows indicate the location of the holes. Edges of the scaffolds are delineated by the white dashed lines. Scale bar: 100 μm.

References

1. Toh YC, Ng S, Khong YM, Zhang X, Zhu Y, Lin PC, Te CM, Sun W, Yu H. Cellular responses to a nanofibrous environment. Nano Today 2006;1:34-43.
2. Pham QP, Sharma U, Mikos AG. Electrospinning of polymeric nanofibers for tissue engineering applications: a review. Tissue Eng 2006;12:1197-211.
3. Liang D, Hsiao BS, Chu B. Functional electrospun nanofibrous scaffolds for biomedical applications. Adv Drug Deliv Rev 2007;59:1392-412.
4. Barnes CP, Sell SA, Boland ED, Simpson DG, Bowlin GL. Nanofiber technology: designing the next generation of tissue engineering scaffolds. Adv Drug Deliv Rev 2007;59:1413-33.
5. Ma Z, Kotaki M, Inai R, Ramakrishna S. Potential of nanofiber matrix as tissue-engineering scaffolds. Tissue Eng 2005;11:101-9.
6. Tan SH, Inai R, Kotaki M, Ramakrishna S. Polymer 2005;46:6128-34.
7. Subbiah T, Bhat GS, Tock RW, Parameswaran S, Ramkumar SS. Electrospinning of nanofibers. J Appl Polym Sci 2005;96:557-69.
8. Li D, Xia Y. Electrospinning of nanofibers: reinventing the wheel? Adv Mater 2004;16:1151-70.
9. Li W-J, Laurencin C, Caterson E, Tuan R, Ko F. Electrospun nanofibrous structure: a novel scaffold for tissue engineering. J Biomed Mater Res 2002;60:613-21.
10. Baker BM, Gee AO, Metter RB, Nathan AS, Marklein RA, Burdick JA, Mauck RL. The potential to improve cell infiltration in composite fiber-aligned electrospun scaffolds by the selective removal of sacrificial fibers. Biomaterials 2008;29:2348-58.
11. J Nam J, Huang Y, Agarwal S, Lannutti J. Improved cellular infiltration in electrospun fiber via engineered porosity. Tissue Eng 2007;13:2249-57.
12. Soliman S, Sant S, Nichol JW, Khabiry M, Traversa E, Khademhosseini A. Controlling the porosity of fibrous scaffolds by modulating the fiber diameter and packing density. J Biomed Mater Res 2011;96A:566-74.
13. Galperin A, Long TJ, Ratner BD. Degradable, thermo-sensitive poly(N-isopropyl acrylamide)-based scaffolds with controlled porosity for tissue engineering applications. Biomacromolecules 2010;11:2583-92.
14. Yixiang D, Yong T, Liao S, Chan CK, Ramakrishna S. Degradation of electrospun nanofiber scaffold by short wave length ultraviolet radiation treatment and its potential applications in tissue engineering. Tissue Eng Part A 2008;14:1321-9.
15. Choi H, Johnson JK, Nam J, Farson DF, Lannutti J. Structuring electrospun polycaprolactone nanofiber tissue scaffolds by femtosecond laser ablation. J Laser Appl 2007;19:225-31.
16. Lim YC, Johnson J, Fei Z, Wu Y, Farson DF, Lannutti JJ, Choi HW, Lee LJ. Micropatterning and characterization of electrospun poly(ε-caprolactone)/gelatin nanofiber tissue scaffolds by femtosecond laser ablation for tissue engineering applications. Biotechnol Bioeng 2011;108:116-26.

17. Chichkov BN, Momma C, Nolte S, von Alvensleben F, Tünnermann A. Femtosecond, picosecond and nanosecond laser ablation of solids. Appl Phys A 1996;63:109-15.
18. Grigoropoulos C. Transport in laser microfabrication: fundamentals and applications. New York: Cambridge University Press; 2009.
19. McCullen SD, Gittard SD, Miller PR, Pourdeyhimi B, Narayan RJ, Loboa EG. Laser ablation imparts controlled micro-scale pores in electrospun scaffolds for tissue engineering applications. Ann Biomed Eng 2011;12:3021-30.
20. Hashi CK, Derugin N, Janairo RRR, Lee R, Schultz D, Lotz J, Li S. Antithrombogenic modification of small-diameter microfibrous vascular grafts. Arterioscler Thromb Vasc Biol 2010;30:1621-7.
21. Hashi CK, Zhu Y, Yang GY, Young WL, Hsiao BS, Wang K, Chu B, Li S. Antithrombogenic property of bone marrow mesenchymal stem cells in nanofibrous vascular grafts. Proc Nat Acad Sci 2007;104:11915-20.
22. J Park JS, Chu JS, Tsou AD, Diop R, Tang Z, Wang A, Li S. The effect of matrix stiffness on the differentiation of mesenchymal stem cells in response to TGF-β. Biomaterials 2011;32:3921-30.
23. Charest JL, Bryant LE, Garcia AJ, King WP. Hot embossing for micropatterned cell substrates. Biomaterials 2004;25:4767-75.
24. Mapili G, Lu Y, Chen S, Roy K. Laser-layered microfabrication of spatially patterned functionalized tissue-engineering scaffolds. J Biomed Mater Res 2005;75B:414-24.
25. Mantovani A, Sica A, Sozzani S, Allavena P, Vecchi A, Locati M. The chemokine system in diverse forms of macrophage activation and polarization. Trends Immunol 2004;25:677-86.
26. Badylak SF, Valentin JE, Ravindra AK, McCabe GP, Stewart-Akers AM. Macrophage phenotype as a determinant of biologic scaffold remodeling. Tissue Engin Part A 2008;14:1835-42.
27. Brown BN, Londono R, Totty S, Zhang L, Kukla KA, Wolf MA, Daly KA, Reing JE, Badylak SF. Macrophage phenotype as a predictor of constructive remodeling following the implantation of biologically derived surgical mesh materials. Acta Biomaterialia 2012;8:978-87.
28. Underwood RA, Usui MI, Zhao G, Hauch KD, Takeno MM, Ratner BD, Marshall AJ, Shi X, Olerud JE, Fleckman P. Quantifying the effect of pore size and surface treatment on epidermal incorporation into percutaneously implanted sphere-templated porous biomaterials in mice. J Biomed Mater Res A 2011;98:499-508.
29. Madden LR, Mortisen DJ, Sussman EM, Dupras SK, Fugate JA, Cuy JL, Hauch KD, Laflamme MA, Murry CE, Ratner BD. Proangiogenic scaffolds as functional templates for cardiac tissue engineering. Proc Natl Acad Sci USA 2010;107:15211-6.
30. Fukano Y, Usui ML, Underwood RA, Isenhath S, Marshall AJ, Hauch KD, Ratner BD, Ulerud JE, Fleckman P. Epidermal and dermal integration into sphere-templated porous poly(2-hydroxyethyl methacrylate) implants in mice. J Biomed Mater Res A 2010;94:1172-86.

31. Marshall AJ, Irvin CA, Barker T, Sage EH, Hauch KD, Ratner BD. Biomaterials with tightly controlled pore size that promote vascular ingrowth. ACS Polymer Preprints 2004;45:100-1.
32. Ratner BD. A paradigm shift: biomaterials that heal. Polymer International 2007;56:1183-5.

CHAPTER 3

Synovial Stem Cells and Their Responses to the Porosity of Microfibrous Scaffolds

ABSTRACT

Tissue-specific stem cells can be coaxed or harvested for tissue regeneration. In this study, we identified and characterized a new type of stem cells from the synovial membrane of knee joint, named neural crest cell-like synovial stem cells (NCCL-SSCs). NCCL-SSCs showed the characteristics of neural crest stem cells: they expressed markers such as Sox10, Sox17 and S100b, were clonable, and could differentiate into neural lineages as well as mesenchymal lineages, although NCCL-SSCs were not derived from neural crest during the development. When treated with transforming growth factor b1 (TGF-b1), NCCL-SSCs differentiated into mesenchymal stem cells (MSCs), lost the expression of Sox17 and the differentiation potential into neural lineages, but retained the potential of differentiating into mesenchymal lineages. To determine the responses of NCCL-SSCs to microfibrous scaffolds for tissue engineering, electrospun composite scaffolds with various porosities were fabricated by co-electrospinning of structural and sacrificial microfibers. The increase in the porosity in microfibrous scaffolds enhanced cell infiltration in vitro and in vivo, but did not affect the morphology and the proliferation of NCCL-SSCs. Interestingly, microfibrous scaffolds with higher porosity increased the expression of chondrogenic and osteogenic genes but suppressed smooth muscle and adipogenic genes. These results suggest that the differentiation of NCCL-SSCs can be controlled by both soluble chemical factors and biophysical factors such as the porosity of the scaffold. Engineering both NCCL-SSCs and scaffolds will have tremendous potential for tissue regeneration.

Introduction

Osteoarthritis represents structural breakdown of the synovial joint, affecting 70 million people in the United States [1]. Thus, there is an urgent need to develop effective treatment for the regeneration of tissues such as cartilage, bone and tendon. Mesenchymal stem cells (MSCs) have been isolated from synovial membrane and show potential for cartilage, bone and tendon tissue engineering [2]. In addition, bioactive scaffolds with transforming growth factor β3 (TGF-β3) or stromal cell derived factor-1 (SDF-1) have been used for in situ cartilage regeneration by recruiting synovial stem cells (SSCs) [3, 4]. These results suggest that SSCs are a valuable cell source for both in vitro tissue engineering and in situ knee joint repair. However, the characterization of synovial MSCs is limited to non-specific surface markers such as CD29 and CD44, and it is not clear whether MSCs exist in synovial membranes at an earlier differentiation stage. Here we used explant culture to isolate a precursor of MSCs from the synovial membrane, characterized as neural crest cell-like SSCs (NCCL-SSCs), and investigated how soluble chemical factors and scaffold property could regulate the functions of this MSC precursor.

Scaffolds can be fabricated for tissue engineering by various methods. Electrospinning is a highly versatile method that allows the fabrication of porous, nonwoven and three-dimensional fibrous structures with controllable fiber diameter ranging from nano- to micro-scale [5, 6], and thus has been used extensively in bone, cartilage, tendon, adipose tissue and muscle tissue engineering [7-9]. However, the porosity of electrospun scaffolds is generally low as a result of densely packed network of interconnected fibers. In order to increase the porosity of electrospun scaffolds for cell infiltration, many approaches have been investigated, including using a rotating metal-frame cylinder with different rotation speeds [10], tailoring fiber diameter [11], combining nano- and microfibers [9], using NaCl crystals as porogen agents [12], post-processing by laser ablation [13] or ultraviolet radiation treatment [14], and incorporation of sacrificial fibers [15]. Here, we utilized co-electrospinning method to create microfibrous scaffold with various numbers of sacrificial fibers and thus varying porosity. In this study, we investigated the effect of scaffold porosity as a biophysical cue of extracellular matrix (ECM) on SSC differentiation, which is not well understood compared to the effects of soluble biochemical stimuli [16].

Materials and Methods

Cell Isolation

The synovial membrane was isolated from the knee joints of Sprague–Dawley (SD) rats under a dissecting microscope. Tissue segments were washed three times with phosphate-buffered saline (PBS) supplemented with 1% penicillin/streptomycin (P/S),

cut into millimeter-sized pieces and placed onto the surface of 6-well plates coated with 1% CellStart (Invitrogen Corp.), and maintained at 37 °C in an incubator with 5% CO2. The cells were cultured in Dulbecco's Modified Eagle's Medium (DMEM) with 2% chick embryo extract (MP Biomedical, Inc.), 1% FBS, 1% N2 supplement (Invitrogen Corp.), 2% B27 supplement (Invitrogen Corp.), 100 nM retinoic acid (Sigma–Aldrich, Inc.), 50 nM 2-mercaptoethanol (Sigma–Aldrich, Inc.), 1% P/S and 20 ng ml−1 bFGF (R&D Systems, Inc). Cells migrated out from the tissues within 3 days. Cells were also isolated from synovial membranes of Wnt1-Cre/LoxP-yellow fluorescence protein (YFP) mouse [17] by using the same method.

Immunostaining and Dye Staining

For immunostaining, cells were fixed with 4% paraformaldehyde (PFA), permeabilized with 0.5% Triton X-100 (Sigma–Aldrich, Inc.), and blocked with 1% bovine serum albumin (BSA) (Sigma–Aldrich, Inc.). Samples were incubated with specific primary antibodies against Sox10 (R&D systems), Sox17 (R&D systems), Snail (Santa Cruz Biotechnology, Inc.), Pax-3/7 (Santa Cruz Biotechnology, Inc.), Slug (Santa Cruz Biotechnology, Inc.), vimentin (DAKO), NG2 (Millipore), S100 calcium binding protein B positive (S100β) (Sigma–Aldrich, Inc.), neural filament-medium polypeptide (NFM) (Sigma–Aldrich, Inc.), glial fibrillary acidic protein (GFAP) (Millipore), neuronal class III β-Tubulin (TUJ1) (Chemicon), smooth muscle α-actin (SMA) (Epitomics, Inc), smooth muscle myosin heavy chain (SM-MHC) (Santa Cruz Biotechnology, Inc.), calponin-1 (CNN-1) (Epitomic, Inc.) and Collagen II (Chemicon) for 2 h at room temperature, washed three times with PBS, and incubated with appropriate Alexa 488- and/or Alexa 546-labeled secondary antibodies (Molecular Probes, Inc.). Nuclei were stained with DAPI (Invitrogen Corp.). Fluorescence images were collected using a Zeiss LSM710 confocal microscope (Carl Zeiss MicroImaging). For organic dye staining, cells were fixed with 4% paraformaldehyde for 30 min, washed and stained with alizarin red (Sigma–Aldrich, Inc.), alcian blue (Sigma–Aldrich, Inc.), or oil red (Sigma–Aldrich, Inc.) according to the manufacturer's instructions. Images were collected using a Zeiss Axioskop 2 Plus microscope.

Flow Cytometry Analysis

For flow cytometry analysis, cells were dissociated after exposure to 0.2% EDTA for 20 min at room temperature. The cells in suspension were blocked with 1% BSA, incubated with specific pre-conjugated primary antibodies against CD29 (BD Pharmingen) and CD44 (BD Pharmingen). Negative control sample was incubated with a non-specific antibody with the same isotype as the specific primary antibody, and stained with the same secondary antibody. 7-AAD (BD Pharmingen) was used to exclude dead cells. Cells were analyzed by using FACScan flow cytometer (Becton Dickinson, Inc.) and FlowJo software (Tree Star, Inc.).

Single-Cell Cloning and Stem Cell Differentiation

For the clonal assays, cells were detached, resuspended with maintenance medium, and filtered through membranes with 40 μm pore size to obtain single cells. Filtered cells were seeded onto CellStart-coated 96-well plates at the clonal density (1 cell/well) and cultured for 3 weeks at 37 °C in an incubator with 5% CO2. For the directed differentiation into peripheral neuron-like cells, Schwann cell-like cells, osteoblasts, adipocytes and chondrocytes, the cells were incubated in specific induction media for 1–3 weeks as described previously [18, 19].

Fabrication of PLLA and PLLA/PGA Microfibrous Scaffolds

To produce single-polymer poly(l-lactide) (PLLA) (1.09 dl g−1 inherent viscosity, MW ～131,000) (Lactel Absorbable Polymers) microfibrous scaffolds (as control scaffolds), we performed electrospinning as described previously [14]. In addition, we used PLLA to make structural fiber and poly(glycolic acid) (PGA) (MW ～100,000) (Polysciences, Inc.) to make fast-degrading sacrificial fibers, and fabricated composite microfibrous scaffolds by co-electrospinning. First, we dissolved PLLA and PGA pellets in hexafluoroisopropanol to prepare PLLA (19% w/v) and PGA (12.5% w/v) solutions, respectively. Two 10 ml syringes (loaded in syringe pumps) were filled with PLLA and PGA, respectively, and fitted with flexible silicon tubing connected to 1.5 in. long stainless steel 23G dispensing needles. The two needles were electrically charged by connecting to a +12 kV high-voltage generator, and were placed 90° apart with the PLLA spinneret facing a grounded collecting drum horizontally. For the three types of scaffolds produced (19% w/v PLLA, 19% w/v PLLA/12.5% w/v PGA (low) and 19% w/v PLLA/12.5% w/v PGA (high)), a random orientation of microfibers was achieved by using a low rotation speed (200 rpm) for the collecting drum. We altered the flow rate and gap distance (distance between needle tip and collecting drum) conditions for PGA to generate two different composite scaffolds with varying numbers of PGA fibers. Briefly, the PGA solution was delivered at a flow rate of 0.4 ml h−1 and gap distance of 7 cm for one type of composite scaffold with lower PGA content (referred to as PLLA/PGA (low)) and at a higher flow rate of 1 ml h−1 and a shorter gap distance of 4 cm for another type of composite scaffold with higher PGA content (referred to as PLLA/PGA (high)). Depending on the collecting time, finalized microfibrous scaffolds were ～200–350 μm in thickness based on measurements with a thickness gauge (Mitutoyo America).

To degrade the microfibrous scaffolds and selectively remove the PGA sacrificial fibers from co-electrospun composite scaffolds, we prepared 1 cm × 1 cm scaffolds and degraded them in PBS at 37 °C for 2 or 4 weeks. Due to acidic polymer remnants as a result of random hydrolytic degradation, PBS was changed every other day throughout the study. The 2 weeks and 4 weeks post-degraded (PD) scaffolds as well as the as-spun (AS) scaffolds without degradation were examined and imaged by field emission scanning electron microscopy (SEM; TM-1000, Hitachi). Furthermore, to confirm the removal of PGA sacrificial fibers, we performed Fourier transform infrared (FTIR) spectrometry with a FTIR spectrometer (Nicolet Avatar 360, Thermo Fisher Scientific)

on the AS and 4 weeks PD scaffolds from the PLLA and PLLA/PGA (high) groups as described previously [20].

Characterization of Porosity and Mechanical Properties of Microfibrous Scaffolds

We conducted image analysis using Matlab and Image J on the SEM micrographs (three micrographs per scaffold group) to generate histograms of the pore size distribution as well as to approximate the average pore diameter (d) as previously described [21]: $d = \sqrt{(l \times h)}$, where l and h are the maximum and minimum pore lengths, respectively.

To quantify the porosity of the electrospun scaffolds, we used gravimetric analysis as previously described [9] with minor modifications. Briefly, 20 samples from each of the AS scaffold groups were prepared. Thickness, width and length measurements of each sample were taken and recorded. Prior to degradation, each sample was weighed; after 2 weeks and 4 weeks degradation, the samples were air-dried and weighed again to determine their apparent density. Finally, the porosity was calculated using the following formula:

$\%\ \text{porosity} = 1 - (\rho_{\text{apparent}}/\rho_{\text{bulk scaffold}}) \times 100$, where $\rho_{\text{apparent}} = \text{mass}_{\text{sample}}/\text{volume}_{\text{sample}}$ and $\rho_{\text{bulk scaffold}} = (\text{mass}_{\text{PLLA}}/\text{mass}_{\text{total}})(\rho_{\text{PLLA}}) + (\text{mass}_{\text{PGA}}/\text{mass}_{\text{total}})(\rho_{\text{PGA}})$.

To determine the mechanical strength of the scaffolds, at least three samples from each scaffold group were air-dried and then subjected to uniaxial tensile testing in the longitudinal direction using an Instron 5544 tester (Instron) as previously described [13]. The applied force and deformation were recorded every second via Bluehill software (Instron). Elastic modulus was calculated by determining the slope from the applied force and scaffold deformation in the linear region of the stress–strain curve between 5% and 10% strain.

In Vitro and In Vivo Cell Infiltration

The 4 weeks PD scaffolds from the PLLA group, the PLLA/PGA (low) group, and the PLLA/PGA (high) group were selected and used for subsequent cell studies because of their significant porosity difference. For the cell studies in vitro, the cells were cultured in maintenance media as described previously in Section 2.1. Scaffolds were cut into 0.5 cm × 0.5 cm squares and secured to non-tissue-culture-treated polystyrene dishes via double-sided tape. Prior to cell seeding, these scaffolds were disinfected in 70% ethanol under germicidal ultraviolet light for 30 min, and subsequently washed five times with sterile deionized water. The scaffolds were then immersed in 1% fibronectin (Sigma–Aldrich, Inc.) for 60 min at 37 °C and washed once with PBS before cell seeding.

To assess the effect of scaffold degradation on cell infiltration in vitro, approximately 100,000 stem cells were seeded onto each of the scaffolds followed by 30 min of incubation to allow for cell attachment. After incubation, sufficient media (DMEM + 10% FBS) was added to each dish. At day 7, the scaffold samples were fixed

with 4% PFA and stained with DAPI for cell nucleus. Cross-sections of 20 μm thickness were generated in the transverse plane using a −20 °C cryosectioner. The fluorescent DAPI signals from the cells within these cross-sections were viewed with the Zeiss LSM710 confocal microscope. At least six cryosections were examined for each scaffold to confirm consistency.

To evaluate the effect of the removal of sacrificial PGA fibers on cell infiltration in vivo, we utilized a rat subcutaneous cell infiltration model as described previously [14]. All experimental procedures with animals were approved by the ACUC committee at University of California, Berkeley. Briefly, three scaffolds from each of the three 4 weeks PD groups were implanted in the subcutaneous cavity of SD rats. On day 7, the scaffolds, along with their immediate surrounding tissue, were explanted and immediately fixed with 4% PFA before being embedded in OCT on dry ice. Cross-sections of 10 μm thickness were generated in the transverse plane using a −20 °C cryosectioner. The sections were stained with DAPI, and observed under a Zeiss LSM710 confocal microscope. At least six cryosections were examined for each scaffold to confirm consistency between sections.

Cell infiltration in vitro was quantified as a percentage of total thickness by measuring the depth of infiltration (normalized to the entire scaffold thickness) of individual cells from the initial seeding surface. Likewise, cell infiltration in vivo was quantified also as a percentage of thickness by measuring the penetration depth (normalized to half of each scaffold's thickness) of individual cells from the surface of the scaffold.

In Vitro Cell Morphology and Proliferation

For cell morphology study, microfibrous scaffolds from the three 4 weeks PD groups were prepared via the same protocol as described above. Approximately 40,000 cells were seeded onto scaffolds from the three groups After 30 min incubation, sufficient media (DMEM + 10% FBS) was added to each dish. To visualize cell morphology and spreading, scaffolds were processed as described [22]. Briefly, samples were stained with Alexa Fluor 488 phalloidin and DAPI for actin filaments and cell nuclei, respectively.

For the cell proliferation study, approximately 75,000 cells were seeded onto each of the scaffolds from the three groups via the same protocol as described above. Samples were fixed after 24 h with 4% PFA, permeabilized and immunostained for the proliferation marker Ki67 (Abcam, Inc.) along with DAPI nuclear counterstain. Image J was used to quantify the number of $Ki67^+$ cells. Three scaffolds were examined and quantified for each scaffold group.

RNA Isolation and Quantitative Polymerase Chain Reaction (qPCR)

To directly explore the effect of cell infiltration on lineage specific gene expressions of stem cells, approximately 1,000,000 cells were seeded on 3 cm × 3 cm scaffolds and cultured in spontaneous differentiation media (DMEM + 10% FBS + 1% P/S) for 1 week. Cells were then lysed with Trizol reagent (Invitrogen Corp.) and total

RNA was extracted as previously described [23]. For qPCR, RNA pellets were resuspended in diethyl pyrocarbonate-treated H_2O. cDNA was synthesized by using two-step reverse transcription with the ThermoScript RT-PCR system (Invitrogen Corp.), followed by qPCR with SYBR green reagent and the ABI Prism 7000 Sequence Detection System (Applied Biosystems). The sequences of the primers used in this study are listed in Supplemental Table 3.1.

Statistical Analysis

The data are presented as mean ± standard deviation. All data were compared by using one-way ANOVA tests. Holm's t-test was then performed to evaluate significant differences among the scaffold groups. $P < 0.05$ was considered statistically significant.

Results and Discussion

Cell Isolation and Characterization

We dissected the synovial membrane from rat knee joint under a dissecting microscope and used a tissue explant culture method to isolate stem cells with a modified medium for neural crest stem cells (NCSCs). The isolated synovial cells showed a fibroblast-like, spindle-shaped morphology (Figure 3.1A and B). The isolated cells express general MSC markers, including CD29 and CD44, as evidenced by flow cytometry analysis (Figure 3.1C and D). To further characterize the marker expression of the isolated synovial cells, we performed protein marker expression screening with over 50 antibodies and found that the isolated cells also express neural crest markers including Sox10, snail, Pax-3/7, Slug, vimentin, endoderm markers Sox17, progenitor marker NG2, glial cell marker S100β and neural cell marker NFM (Figure 3.1E–M). These markers have not been reported in synovial MSC characterization, suggesting that the isolated cells might not be the same as previously identified MSCs.

To determine whether the isolated cells possess multipotency as NCSCs, the cells were cultured with specific induction media for 1–4 weeks. Immunostaining showed that the isolated cells can differentiate into GFAP+/S100β+ Schwann cell-like cells (Figure 3.2A and B) and NFM+/TUJ1+ peripheral neuron-like cells (Figure 3.2C and D) when cultured with specific neural induction media, indicating that they have the capability of differentiating into ectodermal lineages. However, further studies are required to determine whether the derived neural cells are functional. In addition, to test the potential of differentiation into smooth muscle cells (SMCs), we co-cultured the isolated cells with OP9-Delta-1 cell line for 2 weeks [24]. Immunostaining showed that the differentiated cells formed dense stress fibers and expressed SMA and SM-MHC (Figure 3.2E and F), indicating the differentiation into mature SMCs. Furthermore, to test the chondrogenic differentiation potential, we cultured the cells as pellets with 10 ng/ml TGF-β3 for 3 weeks. Alcian blue staining with sections of cell pellets showed significant aggrecan

synthesis (Figure 3.2G). Immunostaining also showed significant collagen II expression in the cell pellets (Figure 3.2H), indicating chondrogenic differentiation. After we cultured the cells in adipogenic medium with insulin for 3 weeks, obvious oil droplets were found in culture (Figure 3.2I). Oil red staining confirmed the differentiation into adipocytes (Figure 3.2J). When the cells were cultured with osteogenic medium for 3 weeks, the cells showed significant calcification (Figure 3.2K), as confirmed by Alizarin red staining (Figure 3.2L).

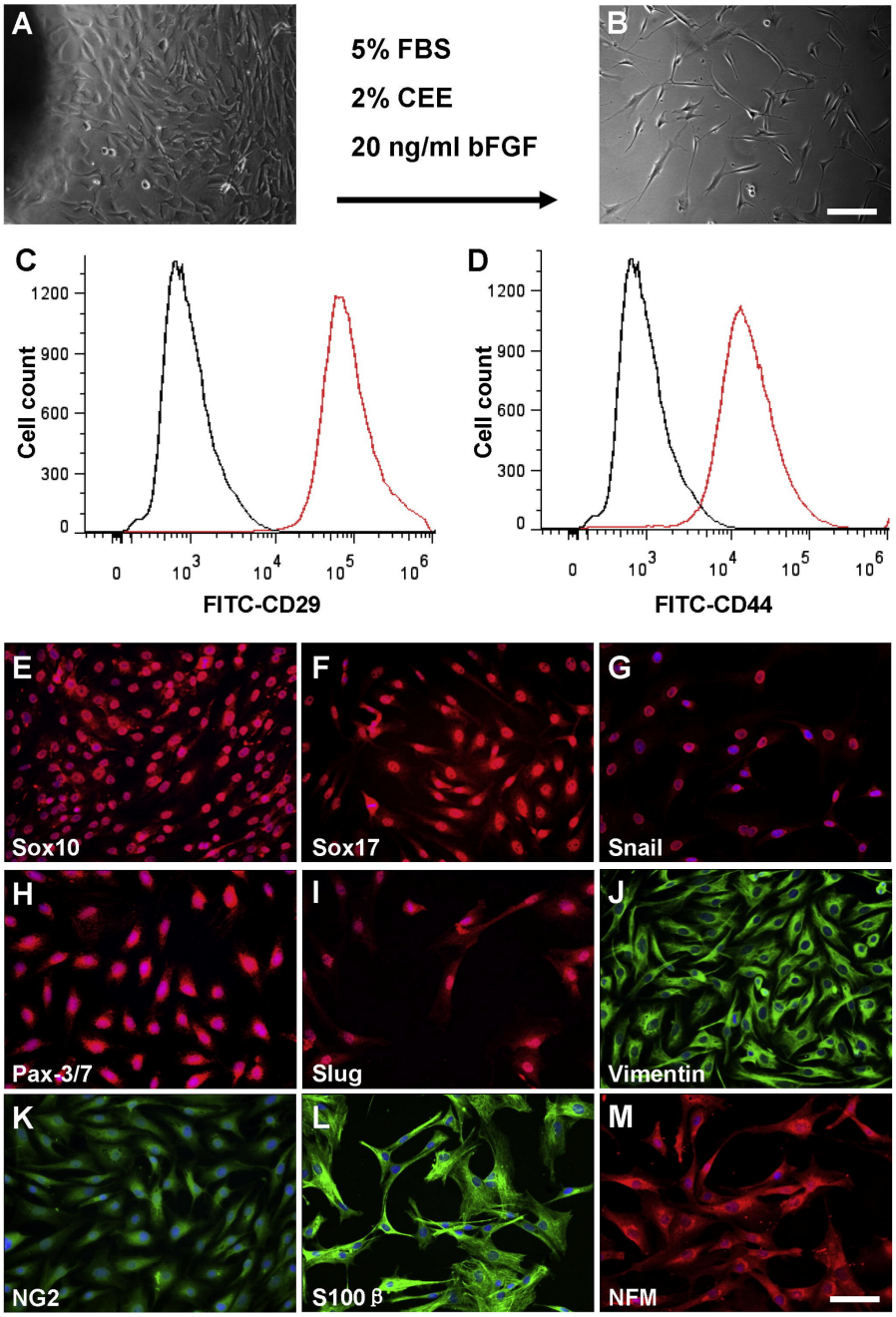

Figure 3.1. Isolation and characterization of NCCL-SSCs. (A, B) Phase-contrast images of isolated synovial cells using tissue explant culture method before and after passaging. Scale bar is 200 μm. (C, D) Flow cytometry analysis of isolated synovial cells using antibodies against CD29 and CD44. (E–M) Immunostaining of isolated cells using antibodies against Sox10, Sox17, Snail, Pax-3/7, Slug, vimentin, NG2, S100β and NFM. Scale bar is 100 μm.

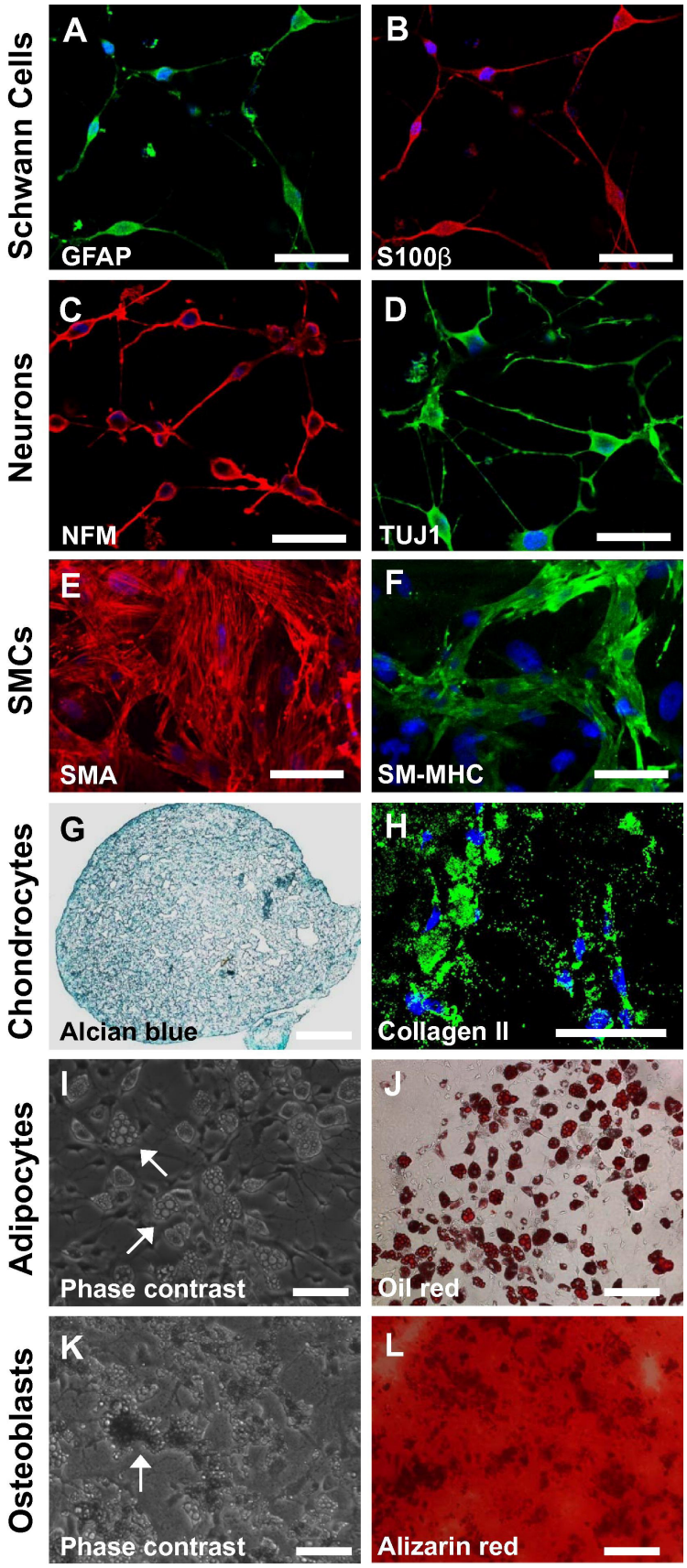

Figure 3.2. Differentiation potential of NCCL-SSCs. The isolated synovial cells were cultured in cultured in specific induction media. (A, B) The directed Schwann cell-like cells were immunostained using antibodies against GFAP and S100β. Scale bars are 50 μm. (C, D) The directed peripheral neuron-like cells were immunostained using antibodies against NFM and TUJ1. Scale bars are 50 μm. (E, F) The directed SMCs were immunostained using antibodies against SMA and SM-MHC. Scale bars are 100 μm. (G, H) The directed chondrocytes were subjected to alcian blue staining and immunostaining using an antibody against collagen II. Scale bars are 100 μm. (I, J) The phase-contrast image and oil red staining were used to show oil droplets, as indicated by the white arrows for characterization of directed adipocytes. Scale bars are 100 μm. (K, L) Phase-contrast image and alizarin red staining were used to show calcium calcification of directed osteoblasts, as indicated by the white arrow. Scale bars are 100 μm.

In summary, the isolated cells not only could differentiate into mesenchymal lineages including SMCs, chondrocytes, adipocytes and osteoblasts as previously reported, but also could differentiate into neural lineages, similar to NCSCs. Therefore, we named this type of cell as NCCL-SSCs.

Single-Cell Cloning of NCCL-SSCs

To investigate whether the derived NCCL-SSCs are a single stem cell type with multipotency or a mixture of different progenitor cells, we performed single-cell cloning in maintenance culture medium. The NCCL-SSCs were detached and seeded into 96-well plates at cloning density (1 cell/well) and cultured for 3 weeks. The average plating efficiency is about 10%, and the derived colonies uniformly express the aforementioned markers including but not limited to Sox10 and Sox17 (Figure 3.3A and B). Differentiation assay showed that the cloned NCCL-SSCs can differentiate into Schwann cell-like cells, peripheral neuron-like cells, SMCs, chondrocytes, adipocytes and osteoblasts (Figure 3.3C–H), indicating that NCCL-SSCs indeed are a type of multipotent stem cells, providing a valuable cell source for tissue engineering.

Knee joint tissues are generally not derived from neural crest; however, given the fact that NCCL-SSCs possess NCSC properties, we performed a lineage tracing experiment by using Wnt1 as a marker to investigate the developmental origin of NCCL-SSCs. NCCL-SSCs were isolated from the synovial membrane of a Wnt-1-Cre/loxP-YFP mouse, but we found that the isolated NCCL-SSCs did not express YFP (Figure 3.3I and J), suggesting that NCCL-SSCs were not derived from neural crest.

Transition of NCCL-SSCs into MSCs

To determine the relationship between NCCL-SSCs and previously identified synovial MSCs, we cultured the NCCL-SSCs in a general medium (DMEM + 10% FBS) that was widely used to culture synovial MSCs in previous studies [2, 25, 26]. TGF-β1 was also added into the medium to promote mesenchymal differentiation. After treatment for 1 week, immunostaining showed that the NCCL-SSCs still retained the expression of some markers including Sox10 and S100β (Figure 3.4A and B), gained the expression of CNN1 (Figure 3.4C), but lost the expression of Sox17 (Figure 3.4D). Flow cytometric analysis showed that the derived cells still retained the expression of the general MSC markers, including CD29 and CD44 (Figure 3.4E and F). However, differentiation assay showed that the cells at this stage lost the response to neural and Schwann cell induction media, indicating that they lost the potential to differentiate into neural lineages (Figure 3.4G and H). Immunostaining also confirmed that the cells shown in Figure 3.4G and H were negative for neural and Schwann cell markers such as GFAP and TUJ1 (data not shown). However, the cells at this stage could still differentiate into SMCs, chondrocytes, osteoblasts and adipocytes (Figure 3.4I–L), suggesting a transition or differentiation into MSCs. Therefore, it is likely that previously identified synovial MSCs are partially differentiated NCCL-SSCs in undefined medium.

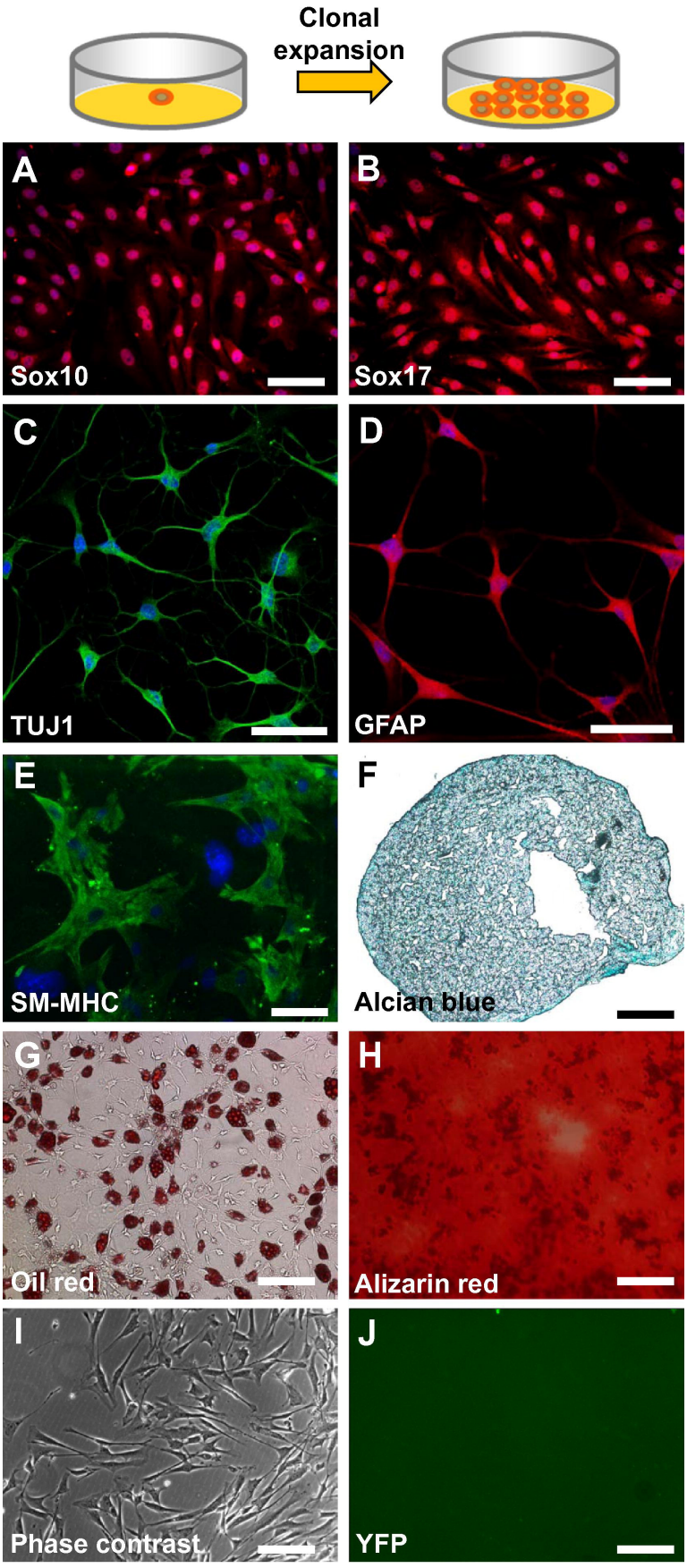

Figure 3.3. Single-cell cloning of NCCL-SSCs. The isolated synovial cells were plated onto 96-well plates at cloning density and cultured in maintenance medium for 3 weeks. (A, B) The cloned cells were immunostained with antibodies against Sox10 and Sox17. Scale bars are 100 µm. (C–H) The cloned cells were differentiated and characterized as in Figure 3.1. Scale bars are 100 µm in C–E; scale bars are 200 µm in F–H. (I–J) The synovial cells were isolated from Wnt1-Cre/LoxP-YFP mice. Phase-contrast and fluorescence images are used to show that the isolated synovial cells were not derived from neural crest. Scale bars are 200 µm.

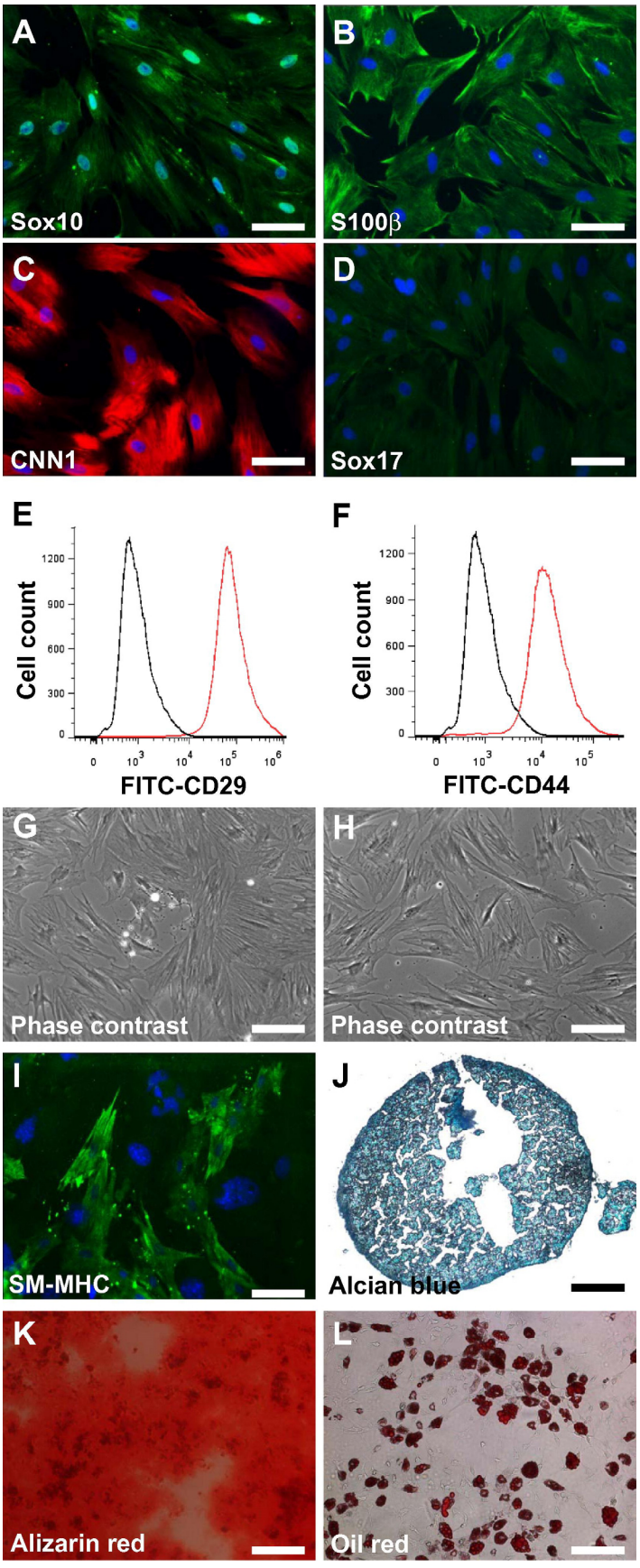

Figure 3.4. Mesenchymal transition of NCCL-SSCs. The isolated NCCL-SSCs were partially differentiated in DMEM with 10% FBS and 10 ng/ml TGF-β1 for 1 week. (A–D) The differentiated NCCL-SSCs were immunostained with antibodies against Sox10, S100β, CNN1 and Sox17. Scale bars are 100 μm. (E, F) Flow cytometry analysis of differentiated NCCL-SSCs with antibodies against CD29 and CD44. (G, H) Phase-contrast images were used to show the differentiated NCCL-SSCs cultured with neural and Schwann cell induction media. Scale bars are 200 μm. (I–L) The multipotency into mesenchymal lineages of partially differentiated NCCL-SSCs was characterized as in Figure 3.1. Scale bar is 100 μm in I; scale bars are 200 μm in J–L.

Fabrication and Characterization of Microfibrous Scaffolds

To determine how NCCL-SSCs responded to microfibrous scaffolds, we fabricated the scaffolds with various porosities by co-electrospinning of slow-degrading PLLA structural fibers and fast-degrading PGA sacrificial fibers [15, 27]. In fact, PLLA has a degradation half-life of a year, whereas PGA degrades between 2 weeks and 4 weeks [28, 29]. The composite scaffolds contained various numbers of PGA fibers. These sacrificial PGA fibers were subsequently removed by in vitro degradation for 2 and 4 weeks to improve the porosity of the composite scaffolds.

Prior to using the microfibrous scaffolds for biological studies, the AS and PD scaffolds were characterized for fiber architecture via SEM (Figure 3.5). We were able to obtain single-polymer PLLA scaffolds as well as composite PLLA/PGA scaffolds with different amounts of PGA content (Figure 3.5A, D, G), with fiber diameters ranging from approximately 330 nm to 3.3 μm (Table 3.1). We then degraded the three types of scaffolds in PBS at 37 °C for durations of 2 weeks (Figure 3.5B, E, H) and 4 weeks (Figure 3.5C, F, I), changing the PBS every other day to prevent the accumulation and retention of acidic byproducts that could have undesired effects on cell behaviors [30]. SEM visualization indicated that the PLLA fibers and overall scaffold structure and integrity remained intact despite the removal of a significant portion of PGA fibers. Using image analysis, we generated histograms to show the apparent two-dimensional (2-D) pore size distribution of the different scaffold groups (Figure 3.6) and approximated the average pore diameter as previously described (Table 3.1) [21], which increased directly with degradation time for both PLLA and PLLA/PGA scaffolds. However, these results may be limited in that analyses were conducted on 2-D SEM micrographs, which cannot accurately delineate the geometry and size of the 3-D pores. In addition, utilizing gravimetric analysis to quantify porosity [10, 31], we observed a gradual increase in porosity as a result of controlled degradation and the time-dependent removal of sacrificial PGA fibers. After 2 weeks of degradation, the PLLA/PGA (high) scaffolds exhibited a statistically significant increase in porosity compared to the PLLA (control) and PLLA/PGA (low) scaffolds; after 4 weeks of degradation, not only was the porosity of PLLA/PGA (high) scaffolds significantly higher, but the porosity of PLLA/PGA (low) scaffolds was also significantly higher compared to the PLLA scaffolds (Figure 3.5J). Nevertheless, due to limitations of 2-D image analysis and gravimetric analysis, detailed measurements of porosity and distribution of pore size require further analysis using standardized techniques described in a previous study as well as ASTM F316 and F2150, specifically capillary flow porometry [31]. Furthermore, FTIR measurement confirmed that PGA completely disappeared after 4 weeks of degradation, in which characteristic peaks of PGA, including δCH_2 bending at 1420 cm^{-1}, were only observed in the AS-PLLA/PGA (high) scaffolds (Figure 3.5K) [32].

To assess the effects of sacrificial PGA fibers on the mechanical properties of the composite scaffolds, uniaxial tensile testing was performed on AS- and PD-PLLA, PLLA/PGA (low), and PLLA/PGA (high) scaffolds. The elastic moduli calculated from the linear portion of the stress–strain curves of the tested 2 weeks and 4 weeks PD scaffolds varied significantly (Figure 3.5L). Prior to degradation, AS-PLLA, AS-PLLA/PGA (low), and AS-PLLA/PGA (high) scaffolds had comparable elastic moduli. The elastic moduli of the scaffolds, especially the PD-PLLA/PGA (high) scaffolds,

decreased by up to 50% after in vitro degradation as the sacrificial PGA fibers were removed and larger pores were introduced.

Scaffold	Average fiber diameter (μm)	Minimum fiber diameter (μm)	Maximum fiber diameter (μm)	Average pore diameter (μm)	Median pore size (μm^2)
AS-PLLA	1.496 ± 0.295	0.978	2.428	2.962 ± 0.262	4.75
AS-PLLA/PGA (low)	0.982 ± 0.360	0.328	1.547	2.667 ± 0.198	4.23
AS-PLLA/PGA (high)	0.772 ± 0.224	0.437	1.194	2.088 ± 0.295	4.24
2-weeks PD-PLLA	1.588 ± 0.459	0.661	3.287	3.339 ± 0.228	3.94
2-weeks PD-PLLA/PGA (low)	1.087 ± 0.325	0.478	1.672	4.751 ± 0.182	7.83
2-weeks PD-PLLA/PGA (high)	1.272 ± 0.228	0.956	1.774	4.875 ± 0.074	6.65
4-weeks PD-PLLA	1.429 ± 0.243	0.778	1.937	6.975 ± 0.784	3.78
4-weeks PD-PLLA/PGA (low)	1.185 ± 0.285	0.547	1.752	7.422 ± 1.336	9.36
4-weeks PD-PLLA/PGA (high)	1.534 ± 0.401	0.969	2.679	9.229 ± 1.749	10.4

Table 3.1. Analysis and characterization of electrospun scaffolds. We used image analysis to not only measure the average fiber diameter and the minimum and maximum fiber diameter, but also approximate the average pore diameter and median apparent pore size of the different scaffold groups.

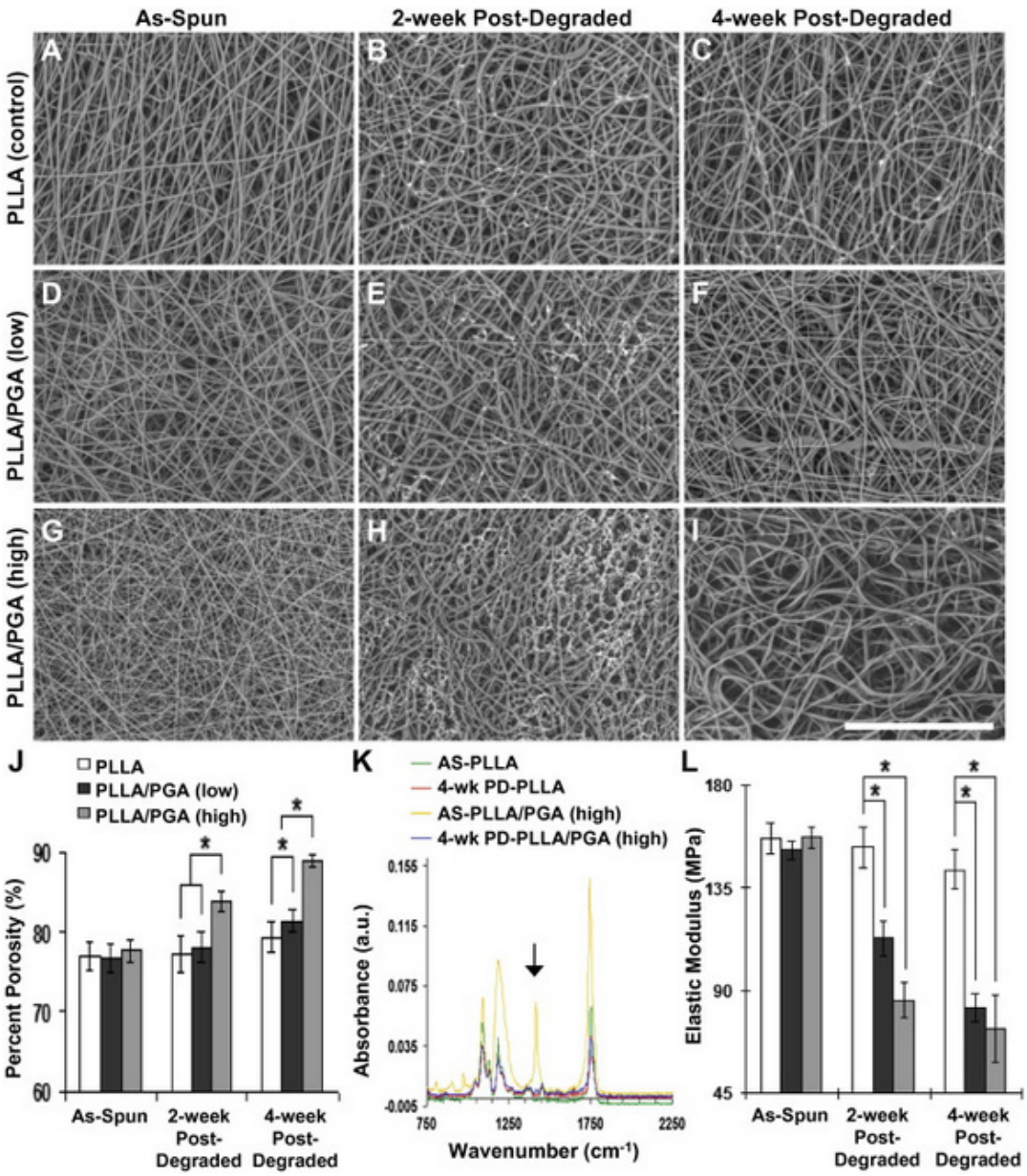

Figure 3.5. Characterization of electrospun microfibrous scaffolds. Scanning electron micrographs were taken of the fabricated electrospun fibrous scaffolds, with 19% PLLA (A–C), 19% PLLA/12.5% PGA (low) (D–F) and 19% PLLA/12.5% PGA (high) (G–I). The scaffolds were as-spun (AS) (A, D, G), 2 weeks post-degraded (PD) (B, E, H) and 4 weeks PD (C, F, I). Scale bar is 100 μm. (J) The porosity of the scaffolds was measured and quantified using gravimetric analysis ($n > 20$). *Significant difference ($P < 0.005$). (K) FTIR spectra of AS-PLLA (green), 4 weeks PD-PLLA (red), AS-PLLA/PGA (high) (yellow) and 4 weeks PD-PLLA/PGA (high) (blue) were obtained as the averages of six measurements taken from the two surfaces of three identical samples. The black arrow indicates a characteristic peak of PGA at 1420 cm^{-1} due to δCH_2 bending. (L) The elastic modulus for each scaffold group was calculated from the slope of the curves and the scaffold dimensions ($n > 3$). *Significant difference ($P < 0.0002$).

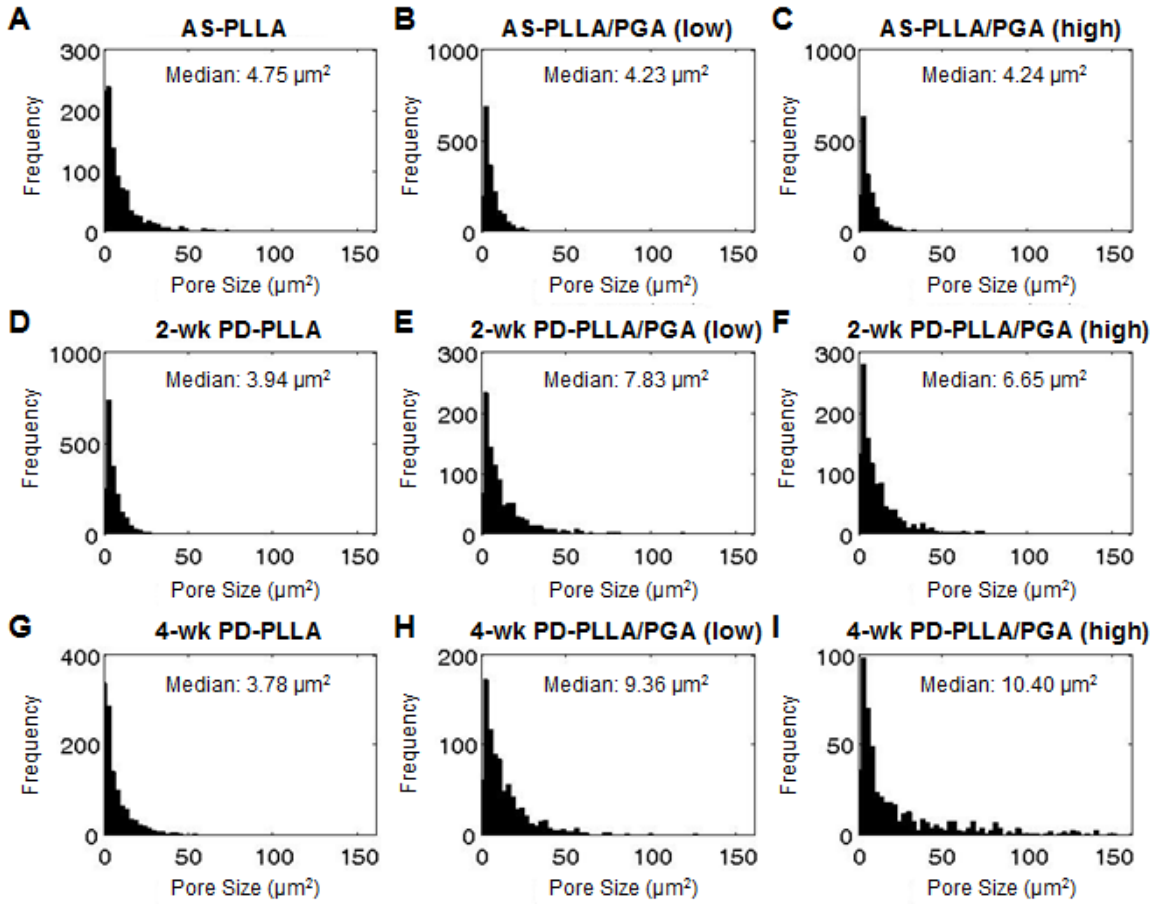

Figure 3.6. Distribution of pore size of the microfibrous scaffolds. Histograms representing the distribution of pore size for each scaffold group were generated using Matlab analysis, with PLLA (A, D, G), PLLA/PGA (low) (B, E, H) and PLLA/PGA (high) (C, F, I). The scaffolds were as-spun (AS) (A–C), 2 weeks post-degraded (PD) (D–F), and 4 weeks PD (G–I).

Effect of Sacrificial PGA Fiber Removal on Cell Infiltration

We performed in vitro and in vivo experiments to investigate the effects of sacrificial PGA fiber removal on cell infiltration into the microfibrous network of the scaffolds. After culturing NCCL-SSCs on the 4 weeks PD scaffolds for 1 week, DAPI staining was performed to assess the extent of cell infiltration into the scaffolds. Cross-section images of the scaffolds indicated noticeable difference of cell infiltration into PLLA fiber meshes and composite PLLA/PGA meshes after PGA degradation (Figure 3.7A–C). Cell infiltration was limited in PD-PLLA scaffolds (Figure 3.7A), while in PD-PLLA/PGA scaffolds, cell infiltration increased with the number of sacrificial PGA fibers Figure 3.7B and C). In fact, cell infiltration quantification indicated that the PLLA/PGA (high) scaffolds exhibited approximately a 7.6-fold and 3-fold increase in cell infiltration

compared to the PLLA (control) and PLLA/PGA (low) scaffolds, respectively (Figure 3.7G). Thus, the improved cell infiltration into PD-PLLA/PGA scaffolds suggests that the increase in overall porosity and pore size is sufficient to facilitate and increase cell penetration. Although the pore size might be comparable to or smaller than cell size, the cells could deform and migrate through the 3-D structure.

Furthermore, cell infiltration was further assessed in an in vivo rat subcutaneous cell infiltration model. Scaffolds from the three 4 weeks PD groups were implanted for 1 week, and the cross-sections were stained with DAPI to visualize the distribution and infiltration of cells throughout the scaffold thickness (Figure 3.7D–F). In general, cell infiltration showed the same trend as that in vitro, in which the PLLA/PGA (high) scaffolds exhibited approximately a 2.7-fold and 1.4-fold increase in cell infiltration compared to the PLLA (control) and PLLA/PGA (low) scaffolds, respectively (Figure 3.7H). However, although the observed penetration and distribution of cells in vivo were better than those in vitro, it is worth noting that in vivo cell infiltration may involve multiple cell types, including inflammatory cells and fibroblasts.

Effects of PGA Fiber Removal on Cell Morphology and Proliferation

Actin staining was used to visualize NCCL-SSCs on the 4 weeks PD scaffolds after 1 day of culture (Figure 3.8A–C). No drastic difference in cell morphology on the scaffold surface was observed based upon the qualitative staining. In addition, the quantification of the cell spreading area indicated no statistically significant difference among the three scaffolds (Figure 3.8G).

NCCL-SSCs had a cell doubling time of 50 h, and the cell growth rate did not change significantly within 5 days after being seeded. To determine the effect of microfiber composition and degradation on cell proliferation, Ki67 staining was used to quantify proliferating cells in active phases of the cell cycle after culturing for 1 day (Figure 3.8D–F). There were no significant differences among the 4 weeks PD groups for PLLA, PLLA/PGA (low) and PLLA/PGA (high) (Figure 3.8H). Even though scaffold structure with higher porosity and larger pore size has been shown to generate better cell growth [30], these results suggest that the manipulation of porosity by including and removing sacrificial PGA fibers did not adversely affect cell behavior such as cell spreading and proliferation.

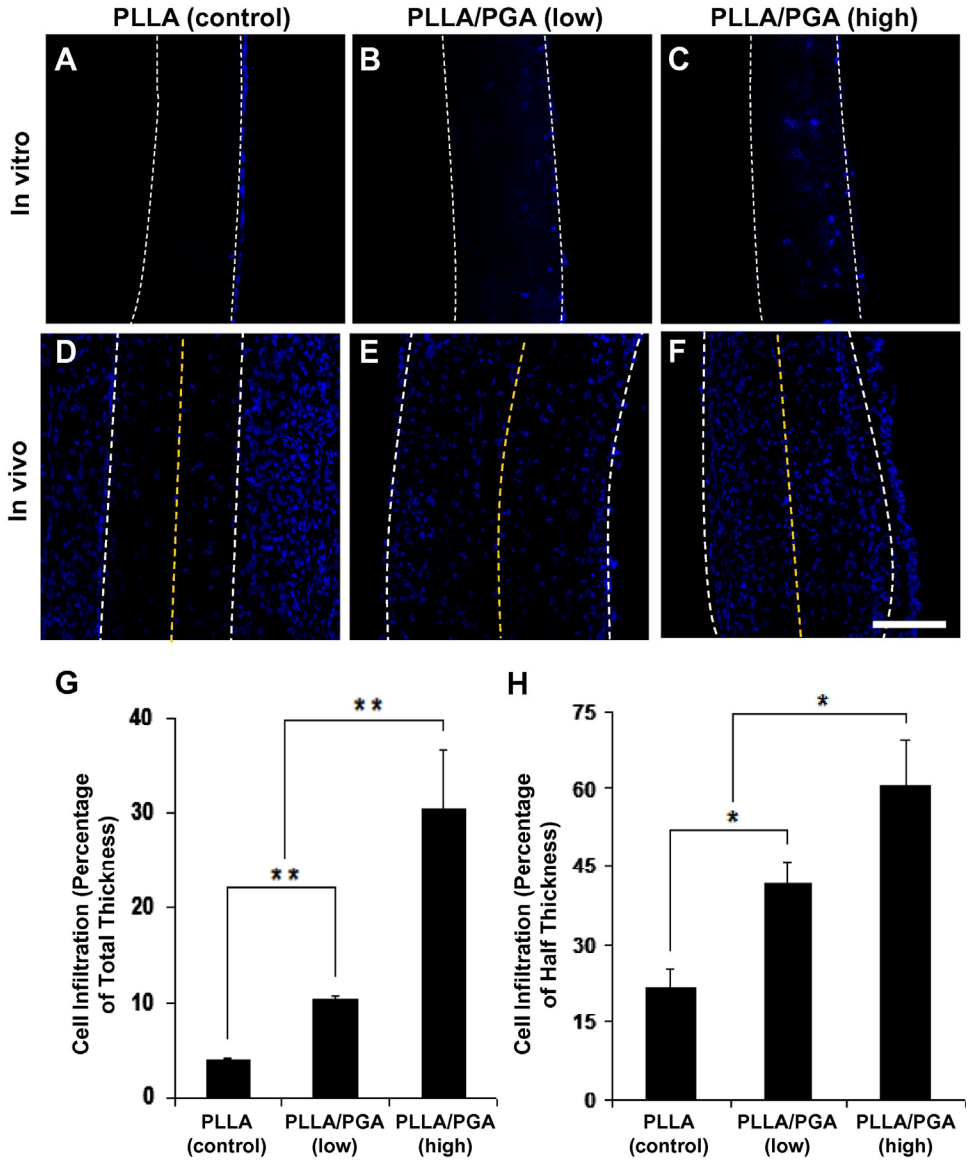

Figure 3.7. In vitro and in vivo cell infiltration into the microfibrous scaffolds. Scaffolds from 4 weeks PD-PLLA (A, D), 4 weeks PD-PLLA/PGA (low) (B, E) and 4 weeks PD-PLLA/PGA (high) (C, F) were selected and used. (A–C) NCCL-SSCs were seeded and cultured for 1 week, followed by nucleus (DAPI) staining of the cells in the cross-sections of scaffolds. (D–F) Cellular infiltration into the microfibrous scaffolds in vivo after 1 week. Scaffolds were implanted subcutaneously between the superficial fascia and contacting muscular layer in the lower abdomen region of SD rats. Nucleus (DAPI) staining of cells in the cross-sections of the scaffolds was performed. Edges of the scaffolds are delineated by the white dashed lines; half of the scaffold thickness is delineated by the yellow dashed lines. Scale bar is 100 μm. Quantitative analyses indicate cell infiltration in vitro with respect to the depth of infiltration as a percentage of total scaffold thickness ($n = 3$) (G), as well as cell infiltration in vivo with respect to the depth of infiltration as a percentage of half of the total scaffold thickness ($n = 3$) (H). **Significant difference ($P < 0.001$); *Significant difference ($P < 0.05$).

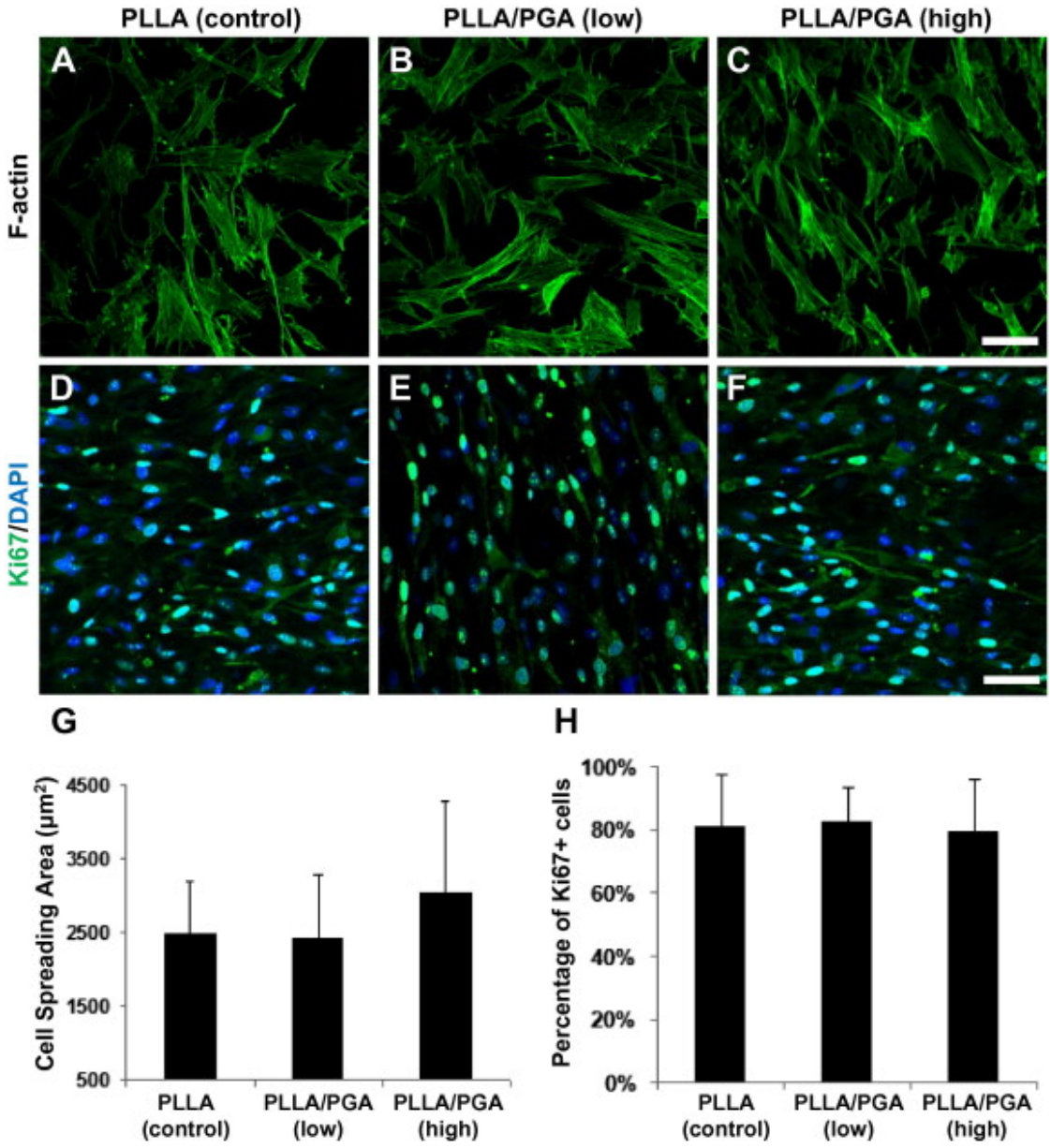

Figure 3.8. Cell morphology and proliferation on the microfibrous scaffolds. Scaffolds from 4 weeks PD-PLLA (A, D), 4 weeks PD-PLLA/PGA (low) (B, E) and 4 weeks PD-PLLA/PGA (high) (C, F) were selected and used. NCCL-SSCs were seeded and cultured for 1 day. (A–C) Cell morphology was visualized by staining the cells with Alexa Fluor 488-phalloidin (actin filaments) and DAPI (nuclei). Scale bar is 50 μm. (D–F) Cell proliferation was quantified by staining for Ki67 (green) and DAPI (blue). Scale bar is 100 μm. Quantitative analyses show the average cell spreading area (G) and the percentage of proliferating cells positive for Ki67 (H) (n = 6).

Effects of cell infiltration on lineage specification of NCCL-SSCs

To determine whether changes in the scaffold porosity regulate cell differentiation, we cultured the NCCL-SSCs on scaffolds with varying porosity using spontaneous differentiation media without any specific chemical clues for 1 week and analyzed the lineage marker expression. Although 4 weeks PD-PLLA/PGA (low) scaffolds were included in this study (data not shown), the 4 weeks PD-PLLA scaffold and 4 weeks PD-PLLA/PGA (high) scaffold with highest porosity were used as representatives. qPCR revealed that the expression of chondrogenic markers, aggrecan and collagen II, increased in cells on more porous scaffolds (Fig. 8A and B), suggesting that cell infiltration may be more favorable for NCCL-SSCs to differentiate into chondrogenic cells. Likewise, osteogenic markers, including osteocalcin (BGLAP) and Runx2, were increased by 2-fold (Fig. 8C and D), suggesting that cell infiltration may also favor osteoblastic differentiation. In contrast, SMC markers, including SMA and CNN1 (Fig. 8E and F), and adipogenic markers, including LPL and PPARγ (Fig. 8G and H), were significantly decreased. However, the change of porosity was not sufficient to drive the terminal differentiation of NCCL-SSCs, and other biochemical differentiation factors might be needed.

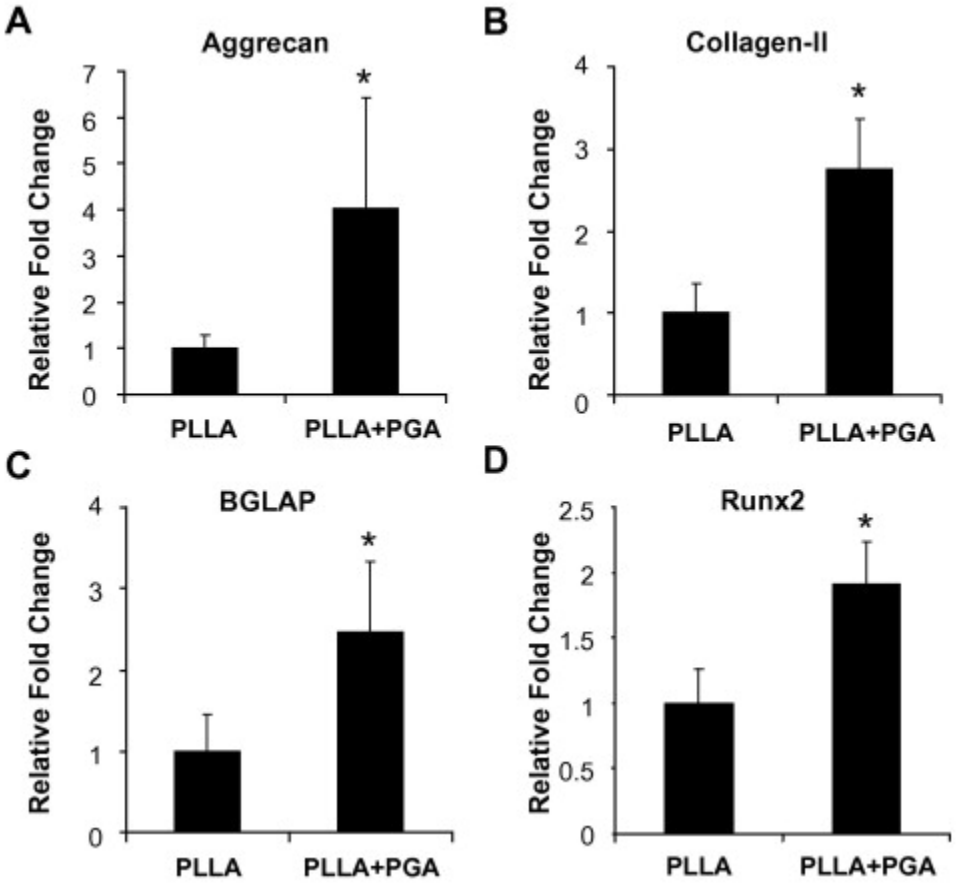

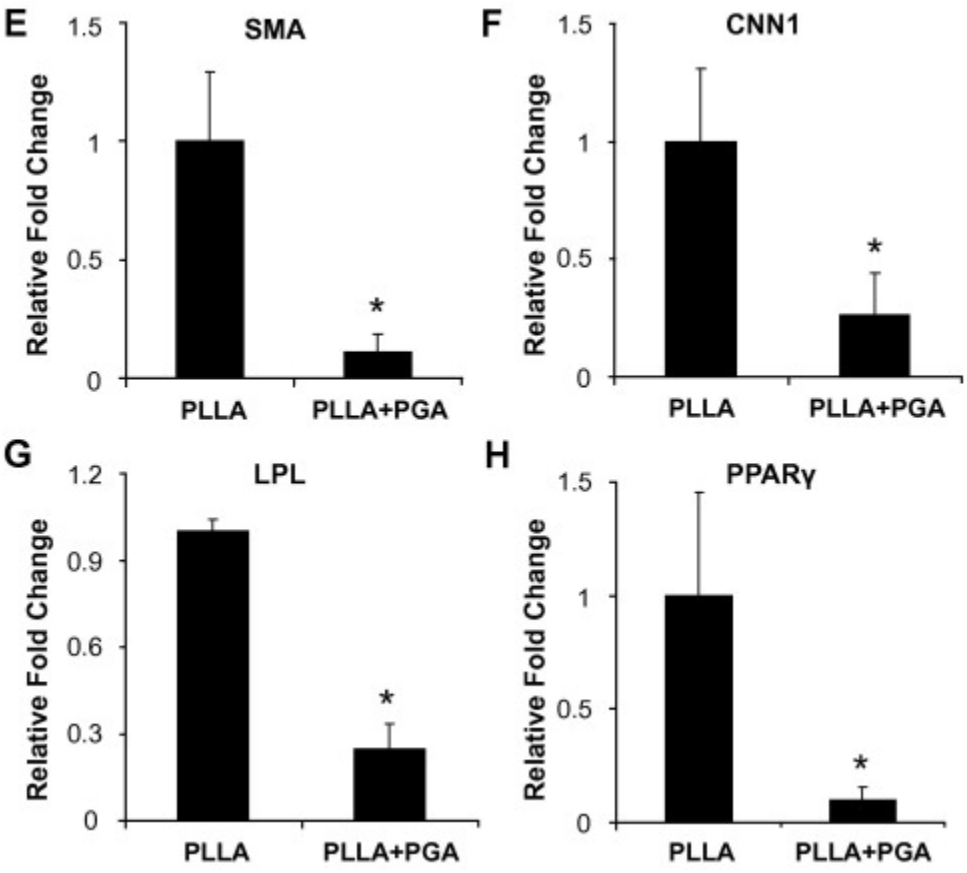

Figure 3.9. Effects of microfibrous scaffolds on lineage commitment of NCCL-SSCs. Scaffolds from 4 weeks PD-PLLA (noted as PLLA) and 4 weeks PD-PLLA/PGA (high) (noted as PLLA + PGA) were selected and used. NCCL-SSCs were seeded and cultured for 1 week in spontaneous differentiation media. The cells were lysed and the extracted RNA was subjected to qPCR analysis for gene expression. Expressions of specific lineage markers for chondrocytes (A, B), osteoblasts (C, D), SMCs (E, F) and adipocytes (G, H) were normalized to the expression level of 18S rRNA. Graphs were shown as relative fold change (y-axis) compared to PLLA group ($n = 3$). *Significant difference ($P < 0.05$).

Conclusions

In this study, we identified a precursor of synovial MSCs, i.e. NCCL-SSCs, that are multipotent as they can differentiate into both ectodermal and mesenchymal lineages. Transcriptional factors such as Sox17 and Sox10, instead of the widely used surface markers such as CD29 and CD44, can be used to characterize the differentiation stage of

stem cells. The transition from NCCL-SSCs to MSCs may represent a general mechanism of adult stem cell differentiation. In addition, we demonstrated that co-electrospinning could be used to create composite scaffolds and manipulate the scaffold porosity; the inclusion of sacrificial PGA fibers and their subsequent time-dependent removal after controlled degradation significantly enhanced cell infiltration both in vitro and in vivo. Another important finding is that the engineered porosity of the scaffolds differentially regulates NCCL-SSC differentiation without specific chemical cues, indicating that certain properties of scaffolds can be tailored to regulate stem cell behavior. It appears that porous scaffolds can facilitate cell infiltration and the differentiation into chondrogenic and osteogenic cells while suppressing the differentiation into SMCs and adipogenic cells. However, it remains to be determined whether this observation can be generalized beyond microfibrous scaffolds. Furthermore, how stem cells sense such change of topographic and 3-D cues and specify the differentiation lineage need to be elucidated. Although biophysical factors such as the porosity of the scaffolds can regulate stem cell differentiation, biochemical factors may be required to drive the terminal differentiation. Whether inflammation in the diseased tissues affects stem cell behavior also needs further investigation. Our findings on NCCL-SSCs and the regulation by biochemical and biophysical factors not only advance our understanding of adult stem cells, but also provide a basis and guidance for the design and fabrication of desirable scaffolds for in situ tissue engineering applications by chemotactic homing of local tissue-specific stem cells in specific tissues.

References

1. Kraus VB. Pathogenesis and treatment of osteoarthritis. Med Clin North Am 1997;81:85–112.
2. De Bari C, Dell'Accio F, Tylzanowski P, Luyten FP. Multipotent mesenchymal stem cells from adult human synovial membrane. Arthritis Rheum 2001;44:1928–42.
3. Mendelson A, Frank E, Allred C, Jones E, Chen M, Zhao W, et al. Chondrogenesis by chemotactic homing of synovium, bone marrow, and adipose stem cells in vitro. FASEB J 2011;25:3496–504.
4. Lee CH, Cook JL, Mendelson A, Moioli EK, Yao H, Mao JJ. Regeneration of the articular surface of the rabbit synovial joint by cell homing: a proof of concept study. Lancet 2010;376:440–8.
5. Lannutti J, Reneker D, Ma T, Tomasko D, Farson D. Electrospinning for tissue engineering scaffolds. Mater Sci Eng C 2007;27:504–9.
6. Tan SH, Inai R, Kotaki M, Ramakrishna S. Systematic parameter study for ultrafine fiber fabrication via electrospinning process. Polymer 2005;46:6128–34.
7. Jang JH, Castano O, Kim HW. Electrospun materials as potential platforms for bone tissue engineering. Adv Drug Deliv Rev 2009;61:1065–83.

8. Bhattarai SR, Bhattarai N, Yi HK, Hwang PH, Cha DI, Kim HY. Novel biodegradable electrospun membrane: scaffold for tissue engineering. Biomaterials 2004;25:2595–602.
9. Thorvaldsson A, Stenhamre H, Gatenholm P, Walkenström P. Electrospinning of highly porous scaffolds for cartilage regeneration. Biomacromolecules 2008;9:1044–9.
10. Zhu X, Cui W, Li X, Jin Y. Electrospun fibrous mats with high porosity as potential scaffolds for skin tissue engineering. Biomacromolecules 2008;9:1795–801.
11. Soliman S, Sant S, Nichol JW, Khabiry M, Traversa E, Khademhosseini A. Controlling the porosity of fibrous scaffolds by modulating the fiber diameter and packing density. J Biomed Mater Res Part A 2011;96A:566–74.
12. Wright LD, Andric T, Freeman JW. Utilizing NaCl to increase the porosity of electrospun materials. Mater Sci Eng C 2011;31:30–6.
13. Lee BL, Jeon H, Wang A, Yan Z, Yu J, Grigoropoulos C, et al. Femtosecond laser ablation enhances cell infiltration into three-dimensional electrospun scaffolds. Acta Biomater 2012;8:2648–58.
14. Yixiang D, Yong T, Liao S, Chan CK, Ramakrishna S. Degradation of electrospun nanofiber scaffold by short wave length ultraviolet radiation treatment and its potential applications in tissue engineering. Tissue Eng Part A 2008;14:1321–9.
15. Baker BM, Gee AO, Metter RB, Nathan AS, Marklein RA, Burdick JA, et al. The potential to improve cell infiltration in composite fiber-aligned electrospun scaffolds by the selective removal of sacrificial fibers. Biomaterials 2008;29:2348–58.
16. Marion NW, Mao JJ. Mesenchymal stem cells and tissue engineering. Methods Enzymol 2006;420:339–61. Rooker SM, Liu B, Helms JA. Role of Wnt signaling in the biology of the periodontium. Dev Dyn 2010;239:140–7.
17. Rooker SM, Liu B, Helms JA. Role of Wnt signaling in the biology of the periodontium. Dev Dyn 2010;239:140-7.
18. Lee G, Kim H, Elkabetz Y, Al Shamy G, Panagiotakos G, Barberi T, et al. Isolation and directed differentiation of neural crest stem cells derived from human embryonic stem cells. Nat Biotechnol 2007;25:1468–75.
19. Wang A, Tang Z, Park IH, Zhu Y, Patel S, Daley GQ, et al. Induced pluripotent stem cells for neural tissue engineering. Biomaterials 2011;32:5023–32.
20. Cheng Q, Komvopoulos K. Synthesis of polyethylene glycol-like films from capacitively coupled plasma of diethylene glycol dimethyl ether monomer. J Phys Chem C 2009;113:213–9.
21. Depan D, Surya PK, Girase B, Misra RD. Organic/inorganic hybrid network structure nanocomposite scaffolds based on grafted chitosan for tissue engineering. Acta Biomater 2011;7:2163–75.
22. Park JS, Chu JS, Tsou AD, Diop R, Tang Z, Wang A, et al. The effect of matrix stiffness on the differentiation of mesenchymal stem cells in response to TGFβ. Biomaterials 2011;32:3921–30.

23. Hashi CK, Derugin N, Janairo RR, Lee R, Schultz D, Lotz J, et al. Antithrombogenic modification of small-diameter microfibrous vascular grafts. Arterioscler Thromb Vasc Biol 2010;30:1621–7.
24. Tang Z, Wang A, Yuan F, Yan Z, Liu B, Chu JS, et al. Differentiation of multipotent vascular stem cells contributes to vascular diseases. Nat Commun 2012;3:875.
25. Nimura A, Muneta T, Koga H, Mochizuki T, Suzuki K, Makino H, et al. Increased proliferation of human synovial mesenchymal stem cells with autologous human serum: comparisons with bone marrow mesenchymal stem cells and with fetal bovine serum. Arthritis Rheum 2008;58:501–10.
26. Fan J, Varshney RR, Ren L, Cai D, Wang DA. Synovium-derived mesenchymal stem cells: a new cell source for musculoskeletal regeneration. Tissue Eng Part B Rev 2009;15:75–86.
27. Ladd MR, Lee SJ, Stitzel JD, Atala A, Yoo JJ. Co-electrospun dual scaffolding system with potential for muscle-tendon junction tissue engineering. Biomaterials 2011;32:1549–59.
28. Leenslag JW, Pennings AJ, Bos RR, Rozema FR, Boering G. Resorbable materials of poly(L-lactide). VII. In vivo and in vitro degradation. Biomaterials 1987;8:311–4.
29. Li S. Hydrolytic degradation characteristics of aliphatic polyesters derived from lactic and glycolic acids. J Biomed Mater Res 1999;48:342–53.
30. Higgins SP, Solan AK, Niklason LE. Effects of polyglycolic acid on porcine smooth muscle cell growth and differentiation. J Biomed Mater Res A 2003;67:295–302.
31. Mukherjee DP, Smith DF, Rogers SH, Emmanual JE, Jadin KD, Hayes BK. Effect of 3D-microstructure of bioabsorbable PGA:TMC scaffolds on the growth of chondrogenic cells. J Biomed Mater Res B Appl Biomater 2009;88:92–102.
32. Kister G, Cassanas G, Vert M. Morphology of poly(glycolic acid) by IR and Raman spectroscopies. Spectrochim Acta Part A 1997;53:1399–403.

CHAPTER 4

End-Point Immobilization of Heparin on Plasma-Treated Surface of Electrospun Polycarbonate-Urethane Vascular Graft

ABSTRACT

Because small-diameter (< 6 mm) synthetic vascular grafts have high failure rate due to primarily surface thrombogenicity, an effective surface chemical modification is desirable. In this study, we engineered an ideal small-diameter, synthetic vascular graft with off-the-shelf availability and desired bioactivity. Carbosil®, a commercially available polycarbonate-urethane (PCU), was electrospun to produce nanofibrous grafts that closely mimicked a native blood vessel in terms of structural and mechanical strength. Through various *in vitro* assessments and comparisons, we determined that plasma treatment was the most effective method to modify the graft surface with functional amine groups, which were subsequently employed to conjugate heparin via end-point immobilization. In addition, we confirmed *in* vitro that the combination of plasma treatment and end-point immobilization of heparin exhibited the highest surface density and correspondingly the highest antithrombogenic activity of heparin molecules. Furthermore, from a short-term *in vivo* study using a rat common carotid artery anastomosis model, we showed that plasma-heparin grafts had higher patency rate at 2 weeks and 4 weeks compared to plasma-control (untreated) grafts. More importantly, we observed a more complete endothelialization of the luminal surface with a more aligned, well-organized monolayer of endothelial cells, as well as more extensive graft integration in terms of vascularization in and cell infiltration from the surrounding tissue. This work demonstrates the feasibility of electrospinning a commercial PCU as an alternative synthetic material to fabricate nanofibrous vascular grafts, as well as the potential to endow desired functionalization to the graft surface via plasma treatment for the conjugation of heparin or other bioactive molecules.

Introduction

Vascular diseases, specifically coronary vascular and peripheral arterial diseases, affect millions of people and remain a worldwide problem as the prevalence continues to rise due to continued growth as the aging of the population [1]. Thus, there is a major unmet need for small-diameter (< 6 mm) vascular grafts as bypass and blood vessel replacement, since autologous vessels, which represent the gold standard and have been shown to demonstrate superior clinical performance, are not always available [2-4]. However, the success of synthetic grafts, such as ones made of Dacron (polyethylene terephthalate; PET) and Teflon (expanded polytetrafluoroethylene; ePTFE), is limited primarily to large-caliber vessels with high blood flow because of their surface thrombogenicity as well as poor elasticity and low compliance that cause acute thrombus formation and intimal hyperplasia, respectively [5-7].

In order to address the shortcoming and develop an ideal, small-diameter vascular graft with mechanically compliant and antithrombogenic properties similar to those of native vessels, different combinations that integrated unique *in vitro* endothelialization techniques or novel surface modifications to endow non-thrombogenic properties with synthetic (i.e. polyesters) as well as natural (i.e. decellularized) surfaces have been well-investigated [8-13]. In fact, from a synthetic material perspective, we, along with many research groups, have employed electrospinning to fabricate fibrous scaffolds for vascular regeneration, since fibrous structures obtained through electrospinning can be tailored to closely resemble the structure and function of the native extracellular matrix (ECM) in order to facilitate cell-material interactions [14-17]. More importantly, such synthetic vascular grafts for small-diameter vessel applications are advantageous because they not only offer off-the-shelf availability but also reduce complications associated with donor-site morbidity and *in vitro* cell source and compatibility.

Recently, one particular polymer that has been electrospun to produce vascular grafts is polyurethane [18-20]. Polyurethanes (PUs) possess excellent biocompatibility and more importantly mechanical properties, which make them ideal for vascular graft applications [21]. However, despite their long-term biostability, PUs eventually degrade *in vivo*; polyester-based PU is susceptible to hydrolytic degradation in the body, whereas polyether-based PU is prone to oxidative degradation [22-24]. As a result, polycarbonate-urethanes (PCUs) have gained more attention and use recently for their improved stability and resistance to both hydrolytic and oxidative degradation [25-27]. Although PU grafts have been reported to have variable patency rates, which in some studies exhibited lower patency rates compared to ePTFE grafts [28, 29], the newer PCUs with and without modifications have reduced thrombogenicity and better *in vivo* performance [30, 31]. More importantly, unlike ePTFE and Dacron, which are much stiffer and less compliant than native vessels, PCU better matches the mechanical properties of native vessels in terms of stiffness and compliance [32, 33].

Numerous strategies of surface modification have been explored to further improve the blood compatibility (i.e. conjugation of heparin) of these PCU surfaces, including chemical immobilization, physical adsorption, and plasma treatment. Heparin, a commonly used anticoagulant agent, has been utilized extensively in vascular therapies

because of its ability to interact with antithrombin-III (AT-III) in preventing thrombus formation [34, 35]. For example, we have previously shown that heparin-modified nanofibrous vascular grafts exhibited higher patency and greater cell infiltration, suggesting that heparin may play multiple roles in maintaining function and promoting remodeling [36]. Other chemical approaches to enable covalent conjugation of heparin using EDC chemistry range from bulk carboxylation of PU via bromoalkylation to the synthesis of PCU with pendant carboxyl groups or with PEG [20, 37, 38]. In addition, recent findings on facile surface modification using mussel-inspired dopamine indicated that such passively adsorbed coating could not only enhance endothelial cell adhesion and viability but also immobilize biomolecules such as VEGF on the surface of vascular graft for accelerated endothelialization [39, 40]. Because this adhesive polydopamine coating serves as a primer for further biofunctionalization, it can be easily applied to different polymeric surfaces for various applications [41, 42]. Furthermore, plasma treatment has been utilized to modify the surface properties of PU as well. For instance, an early study by Kawamoto et al. demonstrated that plasma treatment altered the wettability of the surface of segmented-polyurethane, making it more favorable for the adhesion and proliferation of bovine aortic endothelial cells [43]. Similarly, Bae et al. used oxygen plasma glow discharge to prepare carboxyl group-introduced PU for coupling of polyethylene oxide to immobilize heparin [44]. Although one disadvantage of plasma treatment is its limited penetration depth, it is a powerful surface modification technique useful for the development of small-diameter vascular graft in that surface features can be manipulated to facilitate subsequent biofunctionalization as well as desired endothelialization.

In this study, we electrospun and fabricated small-diameter nanofibrous vascular grafts using Carbosil®, a commercially available thermoplastic PCU. We selected three surface modification techniques from an array of options, and investigated which of them would provide the most effective modification as a primer for subsequent immobilization of heparin on the surface of our PCU grafts. Specifically, we utilized aminolysis with EDC chemistry as a chemical immobilization, polydopamine coating as a passive adsorption, and plasma treatment paired with end-point immobilization to initially introduce amine functional groups and ultimately conjugate heparin on the graft surface. After comparing the three methods, we determined the most effective modification with respect to the surface amine density as well as the antithrombogenic activity of the immobilized heparin. Lastly, we proceeded with these optimized PCU grafts immobilized with heparin for short-term *in vivo* studies, focusing on the performance of heparin-modified electrospun PCU grafts on graft patency as well as endothelialization and overall biocompatibility.

Materials and Methods

Fabrication and Characterization of Polycarbonate-Urethane (PCU) Nanofibrous Vascular Graft

Electrospinning was performed as previously described with minor modification to produce polycarbonate-urethane (PCU) vascular graft [36, 45]. Briefly, polycarbonate-urethane (Carbosil® 90A, DSM Biomedical, Berkeley, CA) was dissolved via sonication in dimethylformamide (DMF) at 16.5% (w/v) concentration. To deliver the polymer solution, a programmable pump along with a 5 mL syringe, which was fitted with flexible silicon tubing connected to 1.5-inch long stainless steel 23G dispensing needles, was used. Two high-voltage generators were utilized to apply approximately +9.7 kV voltage to the needle and -9.2 kV voltage to the collecting mandrel. In addition, the humidity was controlled to be 50-52% during the electrospinning process. PCU solution was delivered at a flow rate of 1.05 mL/hr and gap distance (distance between the positively charged needle tip and the negatively charged collecting mandrel) of 16.5 cm, with a spinneret that traversed in the longitudinal direction to achieve a uniform thickness of the graft longitudinally. PCU fibers with random orientation were obtained by using a low rotation speed (100 rpm) for the collecting mandrel. Electrospinning was allowed to proceed until the wall of the vascular graft reached a desired thickness based on measurements with a thickness gauge (Mitutoyo America, Aurora, IL). The finished graft was placed in a chemical hood overnight to remove any residual DMF.

The overall fibrous structure and integrity of the PCU graft were inspected and imaged using scanning electron microscopy (SEM; TM-1000, Hitachi, Pleasanton, CA). In addition, to determine the mechanical properties of the electrospun PCU graft, graft segments of 1 mm in diameter and 1.5-2 mm in width were prepared and subjected to uniaxial tensile testing in the radial direction using an Instron 5544 tester (Instron, Canton, MA) as described previously [46]. Briefly, two 0.3-mm-diameter stainless steel wires were placed through the lumen of the ring segment of the graft and loaded in between the grips. Each segment was extended until failure at a rate of 0.1 mm/sec, and the applied force and deformation was recorded via Bluehill software (Instron). The elastic modulus was calculated based on the applied load, deformation, and dimensions (thickness and width) of the graft segments; the ultimate tensile strength was recorded as the peak stress prior to failure. The same procedure was conducted after each chemical modification to assess potential changes in the mechanical properties of the PCU graft.

Chemical Modifications of PCU Vascular Graft

Aminolysis of PCU vascular graft to introduce amine functional groups for heparin conjugation

We modified the aminolysis procedure as reported by Zhu et al. to introduce functional amine groups onto the surface of our polycarbonate-urethane (PCU) vascular graft [47]. Briefly, PCU vascular grafts were aminolyzed by immersing them in 100% ethanol (EtOH) containing 50 mg/mL 4-arm-amine-PEG (Sunbright PTE-050PA, NOF America Corporation, White Plains, NY), and heated at 60°C for approximately 4 hours. Aminolyzed grafts were subsequently washed thoroughly with 70% EtOH followed by distilled water. Fourier transform infrared (FTIR) spectrometry was performed with a FTIR spectrometer (Nicolet Avatar 360, Thermo Fisher Scientific, Waltham, MA) as described previously to verify the presence of amine functional groups on the graft

surface (data not shown) [48]. Lastly, 30 mg/mL of unfragmented heparin sodium (Sigma Aldrich, St. Louis, MO) was covalently conjugated to the free amines on the surface of aminolyzed grafts via EDC and Sulfo-NHS (Pierce Biotechnology, Rockford, IL) as described previously [49]. These heparin-conjugated grafts via aminolysis will be referred to as aminolysis-heparin grafts in the remainder of this study.

Polydopamine coating of PCU vascular graft for passive heparin adsorption

We modified the polydopamine coating procedure as described by Lee et al. to introduce an adhesive surface capable of immobilizing biomolecules [50]. Briefly, PCU vascular grafts were initially immersed in 100% EtOH for approximately 10 minutes and washed thoroughly using 1X PBS (pH 8.3). They were then immersed in 2.0 mg/mL of dopamine hydrochloride (Sigma Aldrich) prepared in PBS (pH 8.3) overnight on a shaker at room temperature, and washed with PBS and dried with nitrogen gas. The formation of the polydopamine coating on the grafts was confirmed visually as well as using water contact angle measurements (data not shown). Prior to heparin conjugation, polydopamine-coated grafts were immersed in 0.1N NaOH for 5 minutes and washed with PBS (pH 9). They were subsequently immersed in 30 mg/mL heparin solution prepared in PBS (pH 9) for 24 hours on a shaker at room temperature, followed by washes with PBS. These heparin-adsorbed grafts via polydopamine coating will be referred to as polydopamine (PD)-heparin grafts in the remainder of this study.

Plasma treatment of PCU vascular graft to introduce amine functional groups for end-point immobilization of heparin

In collaboration with Plasma Technology Systems (Belmont, CA), amine functionality was achieved on the graft surface using a two-stage gas plasma recipe from Plasmatreat's Aurora™ low-pressure plasma reactor. The plasma reactor is configured with two side-wall electrodes. A 500-watt RF generator delivers power to the electrodes at 13.56 Mhz. PCU grafts were treated atop Whatman™ glass microfiber filter suspending on screen trays spanning between the power electrodes. The two stages of the plasma recipe consisted of an O_2 plasma cleaning for 1 minute followed by an allyl-amine plasma vapor for 9 minutes to allow polymerization and create an ultra-thin film of stable primary and secondary amines on the graft surface. The allyl-amine evaporation was assisted by a 70°C hot tube and liquid injection system. FTIR spectrometry was performed to confirm the presence of amine functional groups on the graft surface (data not shown). Heparin was conjugated via end-point immobilization onto the surface of plasma-treated grafts, since each heparin chain contains a reducing-end hemiacetal that can be covalently attached to the free amines on the graft surface through reductive amination [51, 52]. Specifically, as previously described with minor modifications, the plasma-treated grafts were immersed in 30 mg/mL heparin solution prepared in cyanoborohydride coupling buffer (0.02 M sodium phosphate, 0.2 M sodium chloride, and 3 mg/mL sodium cyanoborohydride; pH 5.5) for 24 hours on a shaker at room temperature, followed by PBS washes [53]. These heparin-conjugated grafts via plasma treatment will be referred to as plasma-heparin grafts in the remainder of this study.

Utilization of Orange II and Coomassie Brilliant Blue (CBB) Assays for Amine Detection and Quantification

Two colorimetric assays were used as previously described with minor modifications to quantify the amount of free amine groups on the modified surfaces (via aminolysis, polydopamine, and plasma treatment) of the PCU vascular grafts: Orange II and Coomassie Brilliant Blue (CBB) [54]. For both methods, standard solutions containing 0 to 20 mg of NovaPEG amino resin (Novabiochem/EMD Millipore, Billerica, MA) were prepared and used to determine the amine density on the graft surface based on absorbance value comparisons.

Orange II: Modified PCU grafts (1-mm diameter, 0.5-cm length) were immersed in Orange II dye solution (14 mg/mL, Sigma Aldrich) in acidic solution (distilled water adjusted to pH 3 with 1 M HCl) for 30 minutes at 40°C. The grafts were thoroughly and carefully washed using the acidic solution (pH 3) to remove all unbound dye. After air-drying overnight, the grafts were immersed in 1 mL of alkaline solution (distilled water adjusted to pH 12 with 1M NaOH solution). Subsequently, the pH of the solution containing the desorbed dye was adjusted to pH 3 using HCl. The absorbance of the solution from each modification method was measured at 490 nm (Molecular Devices ThermoMax, GMI Inc., Ramsey, MN) and recorded.

Coomassie Brilliant Blue (CBB): Modified PCU grafts were immersed in Coomassie Blue dye solution (0.5 mg/mL, Sigma Aldrich) in acidic solution (approximately 85:10:5 v/v distilled water/methanol/acetic acid; pH ~2.3) for 5 minutes at room temperature. The samples were thoroughly and carefully washed using the same acidic solution to remove all unbound dye. After air-drying overnight, the grafts were immersed in alkaline solution (0.125 M potassium carbonate in 50:50 v/v distilled water/methanol; pH 11.25). The pH of the solution containing the desorbed dye was subsequently adjusted to pH 3 by adding HCl. The absorbance of the solution from each method was then measured at 650 nm (Molecular Devices ThermoMax) and recorded.

Quantification of Heparin on Heparin-Conjugated PCU Vascular Grafts to Determine Its Antithrombogenic Activity and Stability

The presence and stability of heparin on the heparin-conjugated PCU grafts modified via aminolysis, polydopamine, and plasma treatment was confirmed and measured by using toluidine blue (Sigma Aldrich) as described previously [36]. Briefly, at day 0 (immediately after heparin conjugation) and day 7 (one week post-heparin conjugation in which grafts were placed in PBS at room temperature on a shaker), control (untreated), aminolysis-heparin, PD-heparin, and plasma-heparin grafts were immersed in 0.0005% (w/v) toluidine blue solution and vortexed for 10 minutes. Heparin standard solutions containing different amounts of heparin were also prepared in 0.0005% (w/v) toluidine blue solution and vortexed for 10 minutes. After vortexing, 3 mL of n-hexane was added to all the heparin standard and sample solutions and vortexed again for 30 seconds to extract the unbound toluidine blue. The absorbance of the unbound toluidine blue was subsequently measured at 650 nm (Molecular Devices ThermoMax) and

recorded. The density of immobilized heparin on all the samples was determined by comparing their absorbance values to those of the heparin standard solutions.

The antithrombogenic activity and stability of heparin-conjugated PCU grafts modified via aminolysis, polydopamine, and plasma treatment were determined by measuring thrombin activity with the chromogenic substrate S-2238 (Diapharma, West Chester, OH) in the presence of antithrombin-III (AT-III) as previously described with minor modification [36]. Similar to the toluidine blue assay, control (untreated), aminolysis-heparin, PD-heparin, and plasma-heparin grafts taken from day 0 and day 7 were incubated in a 50 mM Tris buffer along with 0.08 NIH units of human AT-III (Sigma Aldrich) for 5 minutes at 37°C. Heparin standard solutions containing varying amounts of heparin were also prepared in Tris buffer along with 0.08 NIH units of human AT-III. Subsequently, 0.08 NIH units of human thrombin (Sigma Aldrich) were added to each of the samples and standard solutions, followed by mixing and incubating for 30 seconds at 37°C. After the thrombin addition, 5 mM S-2238 was added to the samples and standard solutions, which were then incubated for 8 minutes at 37°C. Lastly, all the reactions were stopped by adding 40% acetic acid. The absorbance of the sample supernatants as well as the standard solutions were measured at 405 nm (Molecular Devices ThermoMax) and recorded to determine the thrombin activity in the solutions. The heparin activity of all the samples was subsequently determined by comparing the absorbance values to those of the heparin standard solutions.

Short-Term *In Vivo* Study

Implantation and explantation of plasma-treated PCU vascular grafts

All experimental procedures were approved by the Institutional Review Board Service and the Institutional Animal Care and Use Committee (IACUC) at the University of California, Berkeley. To evaluate and compare the performance of control (untreated) and heparin-conjugated PCU grafts in a short-term *in vivo* study, we used a rat common carotid artery anastomosis model. Male Sprague-Dawley (SD) rats were purchased from the Charles River animal facility. Prior to implantation, 1 mm-diameter PCU grafts were electrospun, plasma treated, and disinfected with 70% EtOH under germicidal UV for 10 minutes (referred to as plasma-control grafts); for heparin-conjugated grafts, they were subsequently conjugated with heparin via reductive amination as aforementioned (referred to as plasma-heparin grafts). The rats were anesthetized with 2% isoflurane in 70% nitrous oxide and 30% oxygen. The left common carotid artery was dissected, clamped, and transected. The graft was then sutured end to end with 8 interrupted stitches by using a 10-0 needle. No heparin or any other anticoagulant was used at any point before, during, or after the implantation procedure. To determine patency of the graft at the time of explantation after 2 weeks and 4 weeks *in vivo*, the blood flow in the blood vessel at the distal anastomosis was examined and verified in the live animal under anesthesia. Specifically, the graft was defined as being patent if unobstructed blood flow and noticeable pulsation were observed and confirmed through the graft into the distally attached native carotid artery. Lastly, the animals were euthanized, and the vascular

grafts were explanted and immediately processed for *en face* immunofluorescent staining or histological analysis and immunofluorescent staining.

Histological analysis and immunofluorescence staining

For *en face* immunofluorescent staining, the explanted grafts were carefully trimmed longitudinally using microscissors into four (quarter) pieces and fixed with 4% PFA for 30 minutes. The samples were then washed with PBS, permeabilized with 0.5% Triton X-100, and blocked with 5% donkey serum. Subsequently, they were stained with the following primary antibodies: CD31 (rabbit, Abcam Inc., Cambridge, MA), CD34 (AF4117, goat, R&D Systems, Littleton, CO), vWF (SC-14014, rabbit, Santa Cruz Biotechnology Inc.), and CD45 (05-1410, mouse, EMD Millipore, Billerica, MA). The samples were stained with DAPI for cell nuclei. Images were captured with a Swept Field Confocal (SFC) microscope (Prairie Technologies, Middleton, WI).

Explanted samples for histological analysis were immediately fixed with 4% PFA before being snap-frozen and embedded in optimal cutting temperature (OCT) compound (TissueTek, Elkhart, IN). Cross-sections of 12-μm thickness were collected using a cryosectioner. For immunofluorescent staining, the samples were fixed with 4% PFA, permeabilized with 0.5% Triton X-100, and blocked with 5% donkey serum. They were subsequently stained with the same primary antibodies listed previously in addition to: SMA (ab7817, mouse, Abcam Inc.), CNN1 (ab46794, rabbit, Abcam Inc.), SM-MHC (BT-562, rabbit, Biomedical Technologies, Inc., Ward Hill, MA), CD68 (MCA341R, mouse, AbD Serotec, Raleigh, NC), and CD163 (MCA342R, mouse, AbD Serotec). Lastly, they were stained with DAPI, followed by confocal microscopy with a Zeiss LSM710 confocal microscope (Carl Zeiss, Inc., Thornwood, NY).

Statistical Analysis

The data in this study are presented as mean $\pm$ standard deviation. For comparison between two groups, two-tailed Student's *t*-test was used. For multiple pairwise comparisons to detect whether a significant difference existed between groups with different treatments, all data were initially compared using analysis of variance (ANOVA), followed by Holm's *t*-test for post-analysis. A *P*-value of less than 0.05 between samples in comparison was considered statistically significant.

Results and Discussion

Structural and Mechanical Characterization of PCU Vascular Grafts

We examined the fibrous architecture and quality of our electrospun PCU vascular graft via SEM (Figure 4.1A-D). The PCU fibrous structure consisted of individual fibers with diameters ranging from approximately 160 nm to 2 μm, with an

average fiber diameter of 496.5 ± 315.7 nm (n=50). As depicted in the micrographs, the fibrous structure of both the inner (luminal) (Figure 4.1C) and outer (Figure 4.1D) surfaces of the graft closely resembles native matrix. In addition, desirable porosity as well as random structure and orientation of fibers were achieved, confirming the uniformity and consistency in our optimized parameters for electrospinning PCU. In fact, the parameters were able to produce quality grafts of varying diameters (i.e. 1 mm and 6 mm) that exhibited uniform wall thickness, surface appearance, and overall graft properties (Figure 4.1E,F), demonstrating the versatility of our electrospinning setup.

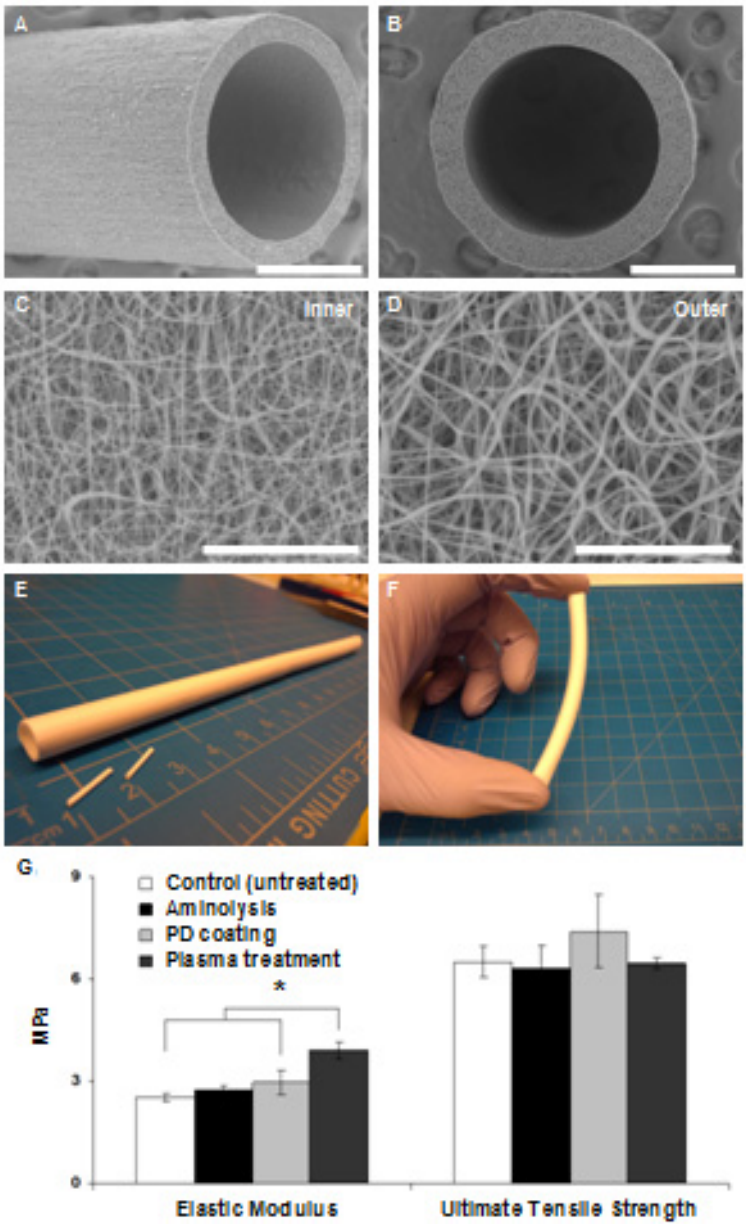

Figure 4.1. Structural and mechanical characterization of nanofibrous PCU vascular graft. Scanning electron microscopy (SEM) images taken from (A) side and (B) top view of an electrospun PCU vascular graft. Structure of nanofibers in the (C) inner (luminal) and (D) outer surface of the vascular graft. (E) Nanofibrous PCU vascular grafts of various inner diameters (i.e. 1-mm and 6-mm) were fabricated to demonstrate the versatility of electrospinning setup. (F) Bending of a 6 mm-diameter PCU graft to confirm desired mechanical property. (G) Comparison of elastic modulus and ultimate tensile strength (UTS) among control (untreated), aminolyzed, polydopamine (PD)-coated, and plasma-treated grafts (n=5). * indicates significant difference (P<0.05). Scale bar = 500 μm in A, B; scale bar = 30 μm in C, D.

Mechanical strength plays a major role in dictating the long-term stability of vascular grafts. Specifically, compliance mismatch at the end-to-end anastomosis between the native artery and the rigid synthetic, especially Dacron and ePTFE, graft results in disturbed flow and shear stress. Thus, we performed mechanical tests to compare our electrospun PCU grafts treated with different chemical modifications and evaluate whether they exhibited similar properties as those of native arteries in terms of elastic modulus and tensile strength (Figure 4.1G). Based on our measurements, control (untreated) PCU grafts had an elastic modulus of 2.54 $\pm$ 0.13 MPa, which is slightly lower than that of the aminolyzed (2.75 $\pm$ 0.14 MPa) and polydopamine-coated (2.97 $\pm$ 0.35 MPa) grafts. Interestingly, the elastic modulus of plasma-treated grafts (3.92 $\pm$ 0.24 MPa) was significantly higher than the control as well as the aminolysis- and polydopamine-modified grafts. It is possible that our surface plasma treatment had a strengthening effect, which could be explained by the increase in elastic modulus of individual fibers or potential interfacial adhesion between adjacent fibers [55, 56]. On the other hand, the control grafts exhibited an ultimate tensile strength of 6.51 $\pm$ 0.44 MPa, comparable to that of the aminolyzed (6.33 $\pm$ 0.67 MPa), polydopamine-coated (7.41 $\pm$ 1.06 MPa), and plasma-treated (6.48 $\pm$ 0.18 MPa) grafts. The comparison of these values indicated that each of the chemical modifications used in this study to functionalize the PCU graft did not adversely affect the overall structure and integrity but could rather strengthen the graft, especially in the case of plasma treatment. More importantly, these tensile properties are comparable to those of human coronary artery, in which both possess low stiffness along with high elasticity that is representative and predictive of their compliance match [57]. However, the mechanical properties of the PCU graft may be further tailored for different applications, such as utilization as conduits for nerve regeneration, by manipulating fabrication parameters and fiber orientation.

Chemical Characterization of Surface Modification of PCU Vascular Grafts

Since mechanical characterization to compare the three chemical modifications did not reveal any undesired changes in mechanical properties, we utilized two chemical assays to assess their effectiveness in amine functionalization of the graft surface: Orange II and Coomassie Brilliant Blue (CBB). Both dyes are commonly used for primary amino group quantification, as they are less expensive, less time-consuming, and more quantitative than other methods, including fluorometry, colorimetry, and spectroscopy. After using varying amounts of the NovaPEG amino resin with known surface amine density to generate a standard curve for each of the two dyes, we quantified the density of exposed primary amine groups on the graft surface (with same dimensions) modified with the different methods (Figure 4.2A, B). For the control (untreated) graft, an insignificant Orange II concentration (0.374 $\pm$ 0.042 mmol/cm^3) was detected, suggesting that nonspecific interactions between the dye and the PCU surface were minimal. In contrast, the plasma-treated graft had an Orange II concentration of 29.787 $\pm$ 0.149 mmol/cm^3, significantly higher than the control as well as the aminolyzed graft (3.623 $\pm$ 0.134 mmol/cm^3) and PD-coated graft (13.659 $\pm$ 0.163 mmol/cm^3) (Figure 4.2A). Similarly, the same trend was observed using the CBB dye, in which the concentration of the dye on the plasma-treated graft (46.876 $\pm$ 0.511 μmol/cm^3) was significantly higher

than the negligible amount on the control (0.003 ± 1.158 μmol/cm^3) as well as the much lower concentrations on the aminolyzed graft (10.397 ± 2.881 μmol/cm^3) and PD-coated graft (28.465 ± 0.640 μmol/cm^3) (Figure 4.2B). Although the exact amine densities as determined by the two colorimetric methods did not match, in which the values from the CBB method were drastically lower than those from the Orange II method, the results were consistent with findings reported previously in a comparison study [54]. In fact, because CBB is a large divalent dye, there exists steric hindrance between CBB molecules that prevented them from binding to some amine groups on the graft surface, resulting in much lower values and lower surface binding compared to those of the small monovalent Orange II dye. Despite the quantitative difference between the Orange II and CBB methods, both revealed the same trend that strongly supported the effectiveness of functionalizing the PCU surface via plasma treatment in comparison to aminolysis and polydopamine coating, specifically in introducing amine groups that could be utilized for subsequent biofunctionalization, such as heparin conjugation.

Verification of Heparin Modification of PCU Vascular Grafts

To further demonstrate that the significantly higher amine density on the plasma-treated PCU graft corresponded to better heparin conjugation with respect to heparin density and stability, we utilized toluidine blue assay to verify and quantify the immobilized heparin on the modified grafts at day 0 (immediately) and day 7 (one week) after heparin immobilization (Figure 4.2C). Immediately after heparin conjugation at day 0, control (untreated) grafts had an insignificant amount of heparin (2.531 μg/cm^3) compared to the heparin density on aminolysis-heparin (27.320 ± 10.968 μg/cm^3), polydopamine (PD)-heparin (28.400 ± 26.763 μg/cm^3), and plasma-heparin (47.740 ± 14.451 μg/cm^3) grafts, confirming that heparin was successfully conjugated via all three methods to the nanofibers. In fact, heparin density on aminolysis-heparin and plasma-heparin grafts was significantly higher than that of control. On the other hand, one week (day 7) after initial heparin conjugation, heparin density on the control, aminolysis-heparin, PD-heparin, and plasma-heparin grafts was 1.246 ± 0.654 μg/cm^3, 21.783 ± 17.459 μg/cm^3, 21.437 ± 11.344 μg/cm^3, and 42.749 ± 5.762 μg/cm^3, respectively. Even though heparin density on both PD-heparin and plasma-heparin grafts was significantly higher than that of control, plasma-heparin grafts retained significantly more heparin than PD-heparin grafts, indicating that plasma treatment was able to bind the most heparin without compromising the stability of the immobilized heparin. This could be correlated with the highest amine density on the surface of plasma-treated grafts, but we speculate that it was due to end-point immobilization of heparin that resulted in the highest heparin density on plasma-heparin grafts. It is highly probable that the utilization of EDC chemistry and passive adsorption to conjugate heparin onto aminolyzed and PD-coated grafts, respectively, increased the likelihood of cross-linking, thereby decreasing the available surface area for heparin attachment. In addition, we believe that the more noticeable decrease in heparin density on the aminolysis-heparin and PD-heparin grafts after one week was due to the loss of heparin that was loosely and not covalently attached to the surface via nonspecific binding. In order to confirm these speculations, more in-

depth analyses need to be further conducted to elucidate the ratio of nonspecific binding and cross-linking as well as the orientation of bound heparin.

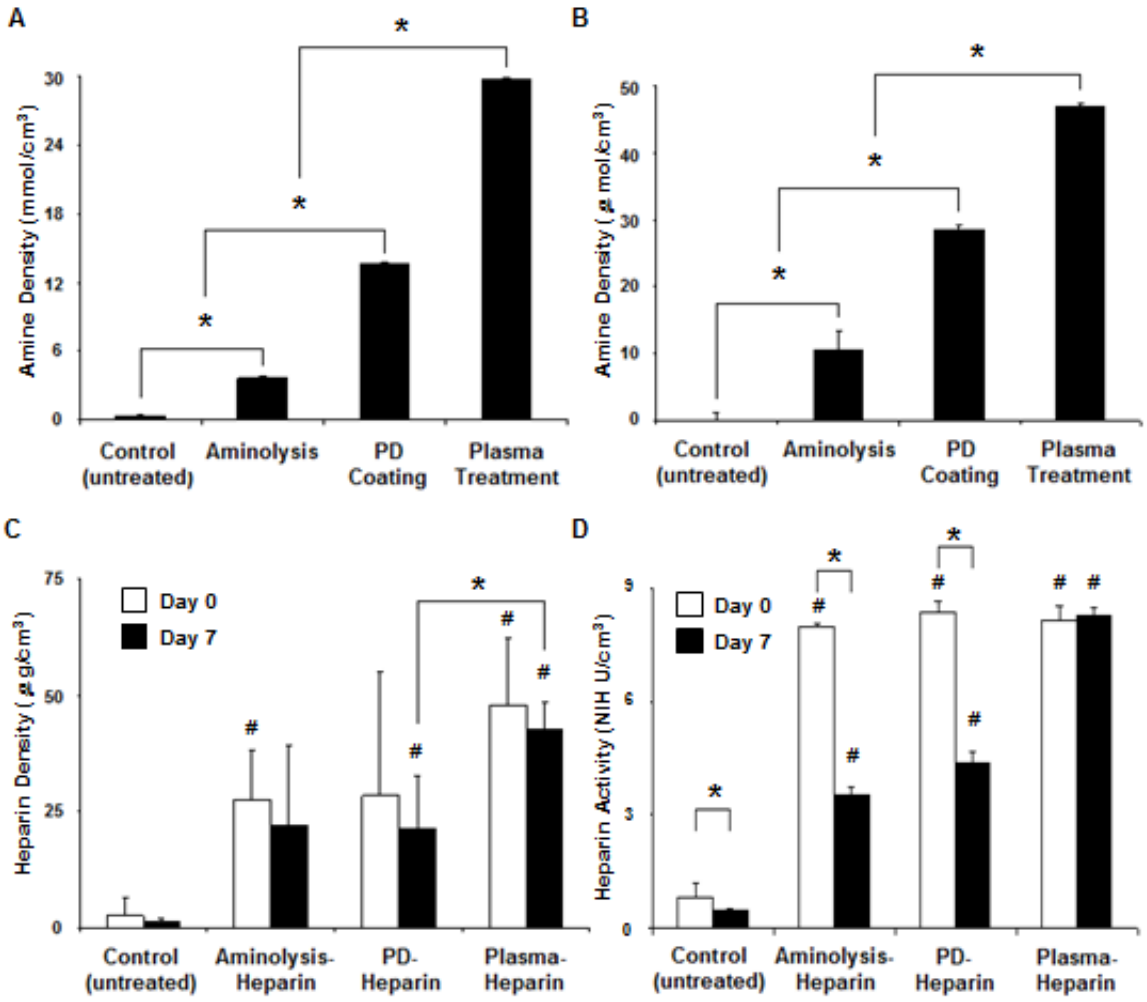

Figure 4.2. Chemical characterization and comparison of surface modifications and heparin conjugation on the surface of nanofibrous PCU vascular graft. Surface density of functional amine groups as introduced via aminolysis, polydopamine (PD) coating, and plasma treatment were quantified using (A) Orange II and (B) Coomassie Brilliant Blue (CBB) dye staining (n=3). (C) Toluidine blue assay was used to verify the presence of conjugated heparin and compare its stability after 1 week (n=3). # indicates significant difference (P<0.05) compared to control (untreated) grafts at respective time point; * indicates significant difference (P<0.05) between the two groups. (D) The maintenance and retention of the antithrombogenic activity of immobilized heparin on the graft surface was quantified using antithrombin-III (n=3). # indicates significant difference (P<0.05) compared to control (untreated) grafts at respective time point; * indicates significant difference (P<0.05) between the two time points of the same group.

Detection of Heparin Activity of Modified PCU Vascular Grafts

To evaluate the maintenance and retention of heparin activity on the graft surface, we performed heparin activity assay to detect the antithrombogenic activity of the immobilized heparin on the modified grafts. Similar to the toluidine blue assay, we quantified the inhibition of thrombin activity in the presence of antithrombin-III on the control (untreated), aminolysis-heparin, polydopamine (PD)-heparin, and plasma-heparin grafts at day 0 (immediately) and day 7 (one week) after initial heparin immobilization (Figure 4.2D). At day 0, control grafts exhibited a baseline activity level of 0.835 ± 0.372 NIH U/cm^3. This value was minimal and significantly lower compared to the activity levels of aminolysis-heparin (7.989 ± 0.094 NIH U/cm^3), PD-heparin (8.370 ± 0.283 NIH U/cm^3), and plasma-heparin (8.151 ± 0.408 NIH U/cm^3) grafts, confirming that the successfully immobilized heparin via the three modifications showed high levels of antithrombogenic activity. However, at day 7, control, aminolysis-heparin, PD-heparin, and plasma-heparin exhibited activity levels of 0.500 ± 0.027 NIH U/cm^3, 3.557 ± 0.199 NIH U/cm^3, 4.360 ± 0.344 NIH U/cm^3, and 8.261 ± 0.239 NIH U/cm^3, respectively. Consistent with our previous results from toluidine blue assay, the heparin conjugated via end-point immobilization on the plasma-treated surface was the most stable as it retained significant activity. In comparison, heparin activity of control, aminolysis-heparin, and PD-heparin groups significantly decreased after 7 days. This suggests that end-point immobilization is more effective and advantageous in that the heparin molecules were immobilized in a more favorable and accessible orientation on the surface of plasma-heparin grafts, thus maximizing the exposure and availability of AT-III binding sites on the immobilized heparin [52, 58]. Therefore, the combination of plasma treatment for amine functionalization and end-point immobilization for heparin attachment provided the most effective technique for heparin conjugation in terms of surface amine functionalization and the maintenance and retention of heparin activity on our electrospun PCU grafts, which was thus selected and used for subsequent small-animal studies to evaluate performance *in vivo*.

In Vivo Performance and Patency of PCU Vascular Grafts

One strategy to improve preclinical and clinical outcomes of synthetic vascular grafts is to incorporate heparin as a blood-contacting coating. Because of its desired anticoagulant and antithrombogenic properties, heparin has been reported to improve the patency of small-diameter grafts [29, 52]. Thus, we aimed to test the efficacy of our surface amine functionalization via plasma treatment by assessing the effects of heparin conjugation on the patency of PCU vascular grafts *in vivo*. Plasma-control (untreated) and plasma-heparin grafts with an inner diameter of 1 mm and approximate length of 0.8 cm were implanted into the left common carotid artery of SD rats. The grafts were examined at 2 weeks and 4 weeks post-operative procedure, with 6 animals per group for each time point. Images of a representative graft from each group at the two time points were taken immediately prior to explantation (Figure 4.3A-D). We noticed much more surrounding tissue around the grafts, especially the plasma-heparin grafts, with visible microvessels indicative of vascularization. Because heparin was immobilized to the entire

graft surface during incubation in heparin solution, we believe that heparin may have played a major role in the recruitment of host cells and the development of such vascularized surrounding tissue. In fact, heparin has been well-reported to bind and regulate the activities of numerous proteins in cellular microenvironment, such as growth factors and ECM components, as well as cell surface proteins that together govern morphogenesis and tissue repair [59, 60]. In terms of graft performance, at 2 weeks, approximately 67% (4 of 6) of plasma-control grafts remained patent, whereas 100% (6 of 6) of plasma-heparin grafts were patent. However, after 4 weeks, plasma-control grafts exhibited approximately 17% (1 of 6) patency, compared to 83% (5 of 6) patency of plasma-heparin grafts. As expected, the antithrombogenic activity of the immobilized heparin as confirmed through our *in vitro* assessment prevented occlusion as a consequence of acute thrombosis, which is a common mechanism for the failure of small-diameter grafts. Furthermore, our patency results (Figure 4.3E) showed interesting similarities and trends as reported in our previous studies, in which heparin-modified grafts exhibited significantly better performance *in vivo* in terms of higher patency rates at various time points [36, 49]. We speculate that our approach further confirmed a synergistic effect of heparin in combination with the nanofibrous structure of our PCU vascular grafts, as the benefits of heparin conjugation were more pronounced as a result of higher surface density from not only high surface-area-to-volume ratio of electrospun fibrous structure but also end-point immobilization of heparin molecules. Therefore, our heparin modification was effective at preventing thrombosis that would have delayed or prohibited endothelialization of the graft lumen.

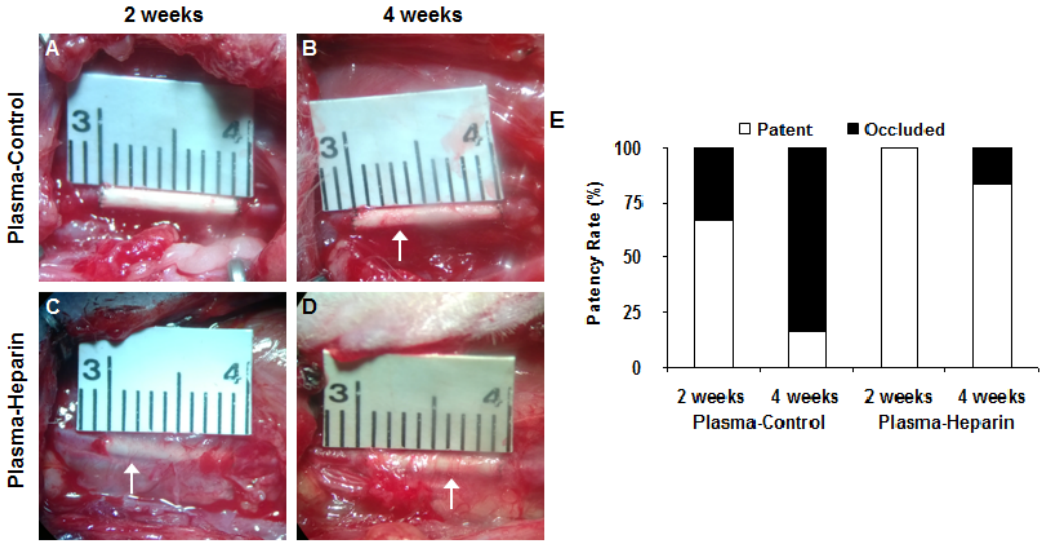

Figure 4.3. Graft explantation and patency of the grafts. Representative image of a (A) 2-week and (B) 4-week plasma-control graft *in situ* taken immediately prior to explantation. Representative image of a (C) 2-week and (D) 4-week plasma-heparin graft *in situ* taken immediately prior to explantation. White arrows indicate noticeable microvessels and vascularization in the surrounding tissue of the grafts. Scale bar is as denoted in A-D. (E) Patency rates of the grafts after 2 weeks and 4 weeks *in vivo* were recorded and compared. Each group at each time point included 6 animals (n=6).

Recruitment of Endogenous Progenitor Cells for Endothelialization and Graft Integration

In addition to mechanical properties, another critical element in dictating the success of vascular grafts *in vivo* is endothelialization. As a result, extensive research in the development and enhancement of an ideal, synthetic vascular graft has focused on engineering luminal surfaces that can promote and accelerate the formation of a mature and functional endothelium. We have previously shown that heparin-modified nanofibrous vascular grafts exhibited more complete endothelialization of the lumen compared to untreated grafts, suggesting that heparin modification may assist in the function and integration of vascular grafts *in vivo* [36]. Similarly, results from our short-term *in vivo* studies were consistent with our previous findings.

En face immunostaining was performed to characterize the cells on the luminal surface of the grafts (Figure 4.4). At 2 weeks (Figure 4.4A-H), although both groups had higher cell number near the anastomosis regions due to trans-anastomotic migration, plasma-heparin grafts had noticeably more cells in the middle portion of the grafts compared to plasma-control grafts (Figure 4.4F, H). In fact, many of these cells were positive for CD34, a marker expressed by endothelial progenitor cells (EPCs). Several endothelial cells (ECs) as identified by $CD31^+$ and vWF^+ staining were also present, especially in the anastomosis-graft region (Figure 4.4A, E). However, these ECs exhibited a more disorganized morphology and less defined cell-cell boundaries, indicating that endothelialization was incomplete as a stable endothelium was still in the early stage of formation. In addition, even though plasma-heparin grafts appeared to have attracted more cells, specifically EPCs, plasma-control grafts exhibited better than expected cell attachment and recruitment. We speculate that the change of PCU surface property from innately hydrophobic to hydrophilic as a result of plasma treatment facilitated cell adhesion, which is consistent with our previous finding that functional amine groups from $Ar\text{-}NH_3/H_2$ plasma treatment promoted attachment and spreading of bovine aorta endothelial cells [59]. Furthermore, both plasma-control and plasma-heparin grafts had a small number of peripheral blood mononuclear cells positive for CD45 (Figure 4.4C-D, G-H), reflecting the difficulty in completely eliminating an inflammatory response.

On the other hand, at 4 weeks after implantation, the luminal surface of the plasma-heparin graft was almost completely covered by cells (Figure 4.4I-L). In particular, most of these cells were $CD31^+$ and vWF^+, with no $CD34^+$ cells present amongst the ECs. These ECs now exhibited a well-organized, cobblestone-like structure that closely resembled the endothelium of a native vessel, along with near-complete alignment of cell nuclei and morphology in the direction of blood flow especially in the anastomosis-graft region (Figure 4.4I, J). Nevertheless, further studies are needed to better determine whether such confluent endothelial coverage resulted from the differentiation and maturation of EPCs, which were observed to have attached at the 2-week time point, into ECs, or the proliferation of mature ECs that migrated trans-anastomotically. Moreover, as shown in Figure 4.4K-L, no $CD45^+$ cells were found in the anastomosis- and mid-graft regions of the 4-week plasma-heparin graft, suggesting that the inflammatory response was acute and potentially transient in the presence of heparin.

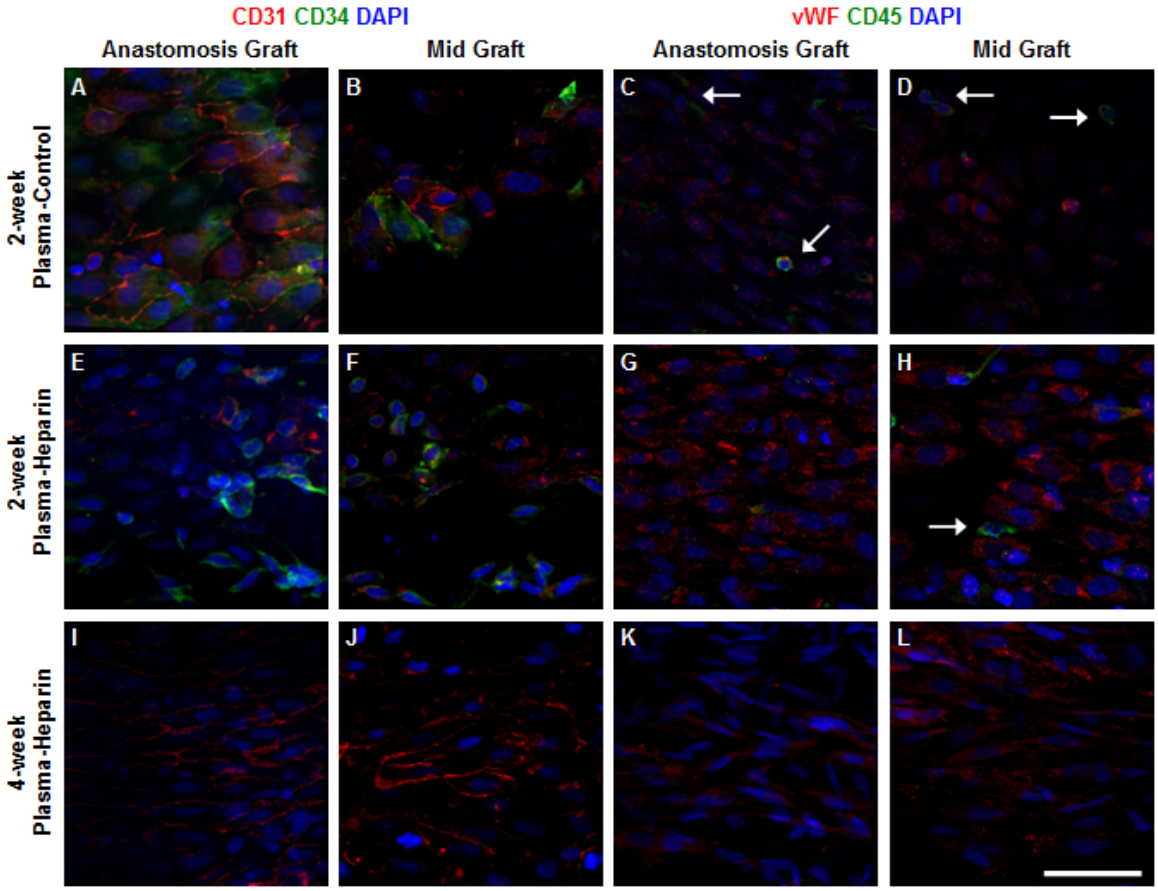

Figure 4.4. *En face* immunostaining of PCU plasma-control and plasma-heparin grafts after 2 and 4 weeks *in vivo*. *En face* immunostaining for CD31 (red) with CD34 (green) and vWF (red) with CD45 (green) of patent (A-D) 2-week plasma-control, (E-H) 2-week plasma-heparin, and (I-L) 4-week plasma-heparin grafts was performed. Representative images were taken from the anastomosis-graft and mid-graft regions of each graft. White arrows indicate cells positive for CD45. Cell nuclei were stained using DAPI (blue). Scale bar = 50 μm.

Cross-section staining to characterize cells not only on the luminal surface but also within the vascular wall and surrounding tissue revealed interesting results. At 2 weeks, both plasma-control and plasma-heparin grafts had $CD34^+$ cells on the luminal surface near the mid-graft region and in the surrounding tissue near the anastomosis, indicative of EPC participation in the endothelialization and regeneration of the grafts (Figure 4.5A-B, G-H). However, very few $CD31^+$ or vWF^+ cells representative of ECs was identified in the plasma-control graft (Figure 4.5A-D), except for an apparent monolayer on the outer lining of the neointima (Figure 4.5C, D); in contrast, more ECs positive for vWF and CD31 were found around the plasma-heparin graft, primarily in the surrounding tissue near anastomosis as well as a few within the vascular wall (Figure 4.5G-J). We believe that heparin modification may have promoted faster vascularization and integration of the graft as represented by the distribution of ECs and formation of

microvasculature surrounding tissue, although further analysis is required to determine the origin and role of these cells. In addition, SMA and CNN1 staining revealed that the patent plasma-control graft at the 2-week time point still developed neointima, as SMA^+ and $CNN1^+$ cells, which most likely are smooth muscle cells (SMCs), were present on the luminal surface, especially at the anastomotic region (Figure 4.5C, E). In comparison, no neointima was noted on the luminal surface of the plasma-heparin graft, in which SMA^+ cells were only present in the surrounding tissue (Figure 4.5I, J). We speculate that neointima formation was caused by surface thrombogenicity and the absence of heparin, corresponding to the poor patency rates of plasma-control grafts.

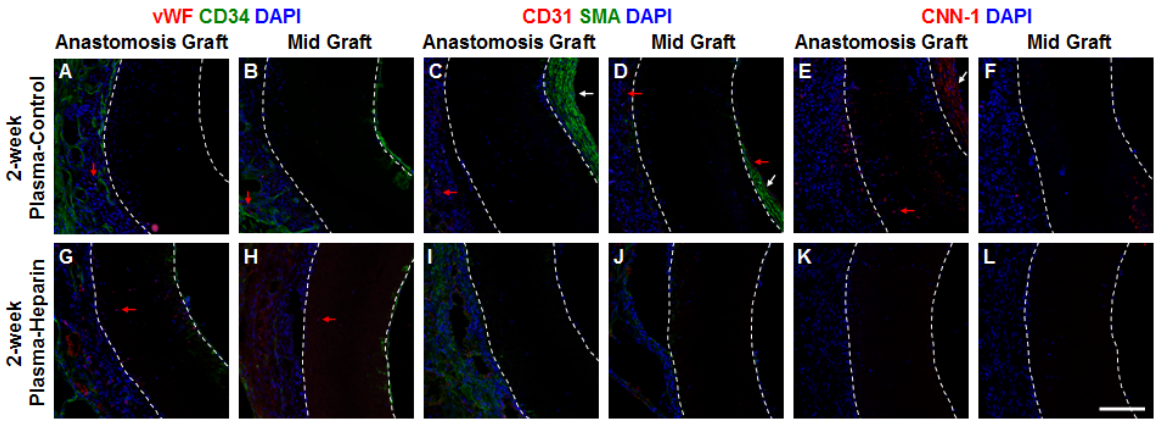

Figure 4.5. Cross-section immunostaining of PCU plasma-control and plasma-heparin grafts after 2 weeks *in vivo*. Immunostaining for (A, B, G, H) vWF (red) and CD34 (green), (C, D, I, J) CD31 (red) and SMA (green), and (E, F, K, L) CNN-1 (red) of the cross-sections obtained from the anastomosis-graft and mid-graft regions of the plasma-control and plasma-heparin grafts after 2 weeks *in vivo* was performed. Red arrows indicate cells positive for the red-colored markers vWF, CD31, and CNN-1. White arrows indicate neointima formation on the luminal surface. White dashed lines delineate the border of the graft wall. Cell nuclei were stained using DAPI (blue). Scale bar = 100 μm.

On the other hand, results from cross-section staining of plasma-control and plasma-heparin grafts at the 4-week time point were somewhat different compared to those from *en face* staining. Unlike the much more well-organized monolayer of ECs characterized on the 4-week plasma-heparin graft via *en face* staining, no sign of endothelialization but rather only a small patch of $CD31^+$ ECs were observed on the luminal surface of the plasma-control (Figure 4.6C, D) and plasma-heparin graft (Figure 4.6I, J), respectively. Likewise, no positive vWF staining was detected in either graft, although the presence and similar distribution of $CD31^+$ cells as seen surrounding the plasma-heparin graft at 2 weeks (Figure 4.5I, J) were also noted at 4 weeks in both the anastomotic and mid-graft regions (Figure 4.6I, J). Interestingly, $CD34^+$ EPCs were still present in the outer lining of the neointima at the anastomosis of the plasma-control graft as opposed to desired $CD31^+$ or vWF^+ ECs (Figure 4.6A). In addition, at 4 weeks,

neointima formation, which was also found on the luminal surface of the plasma-control graft at 2 weeks (Figure 4.5C-E), showed SMA^+ cells as well (Figure 4.6C-F). Although these cells were negative for SM-MHC, a mature marker of SMCs, such neointimal layer would eventually thicken and worsen, ultimately resulting in graft occlusion and failure. Fortunately, no such neointima formation was detected on the luminal surface of the plasma-heparin graft, suggesting the potential of heparin to alleviate thrombogenicity and perhaps suppress intimal hyperplasia. Instead, similar to the 2-week results discussed previously, SMA^+ cells, including SMA^+/$SM\text{-}MHC^+$ cells indicative of mature SMCs, were mainly found and distributed in the surrounding tissue of the plasma-heparin graft, contributing to a better integration and maturation of the graft (Figure 4.6I-L).

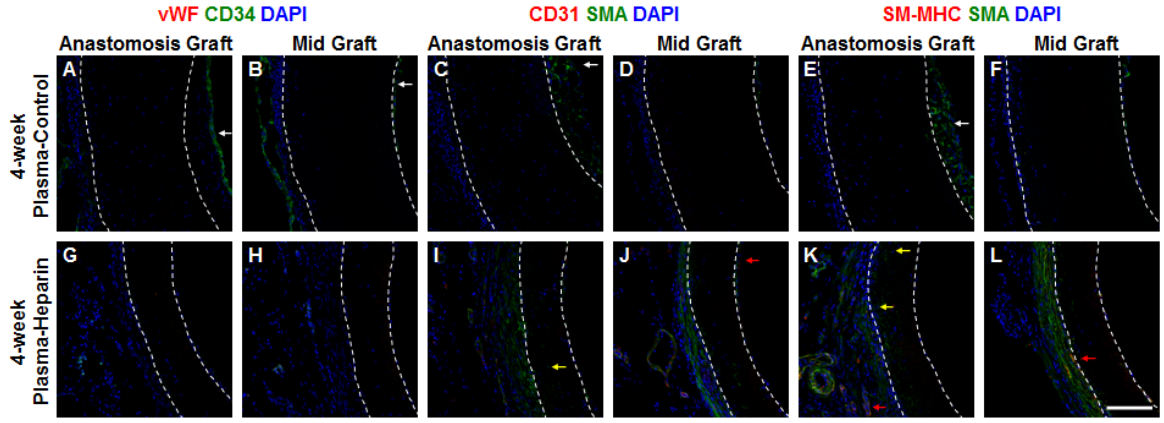

Figure 4.6. Cross-section immunostaining of PCU plasma-control and plasma-heparin grafts after 4 weeks *in vivo*. Immunostaining for (A, B, G, H) vWF (red) and CD34 (green), (C, D, I, J) CD31 (red) and SMA (green), and (E, F, K, L) SM-MHC (red) and SMA (green) of the cross-sections obtained from the anastomosis-graft and mid-graft regions of the plasma-control and plasma-heparin grafts after 4 weeks *in vivo* was performed. Red arrows indicate cells positive for the red-colored markers vWF, CD31, and CNN-1. Yellow arrows indicate cells positive for SMA found within the graft wall. White arrows indicate neointima formation on the luminal surface. White dashed lines delineate the border of the graft wall. Cell nuclei were stained using DAPI (blue). Scale bar = 100 μm.

In terms of inflammatory response, we also performed cross-section staining for CD68 and CD163, which are markers of pan macrophages and specifically M2 macrophages, respectively. At 2 weeks, more $CD68^+$ macrophages were found in the surrounding tissue and within the wall of the plasma-control graft, suggesting that heparin modification could potentially mitigate the inflammatory response typically observed for implanted scaffolds (Figure 4.7A, B). In addition, very few cells, if not none, positive for CD163 were identified (Figure 4.7C-D, G-H). With respect to early integration with host tissue after 2 weeks *in vivo*, both plasma-control and plasma-heparin grafts had significantly more cell infiltration near the anastomosis regions compared to mid-graft (Figure 4.7A-H), which likely resulted from higher transmural migration of cells from the surrounding tissue into the vascular wall. In contrast, at 4 weeks, fewer

CD68^{+} cells were present around or within the plasma-control graft, but much more were found around and within the plasma-heparin graft (Figure 4.7I-J, M-N). However, our staining of CD163, indicative of M2 macrophages that have been shown to participate in tissue remodeling [60], showed positive cells in the tissue surrounding the plasma-heparin graft after 4 weeks *in vivo* (Figure 4.7O, P). We believe that even though macrophages were recruited as indicated by the pan macrophage marker CD68, heparin, which has been known to possess anti-inflammatory properties and the potential to modulate inflammatory cell recruitment, attracted significantly more CD163^{+} M2 macrophages that could facilitate the desired graft remodeling and integration [63].

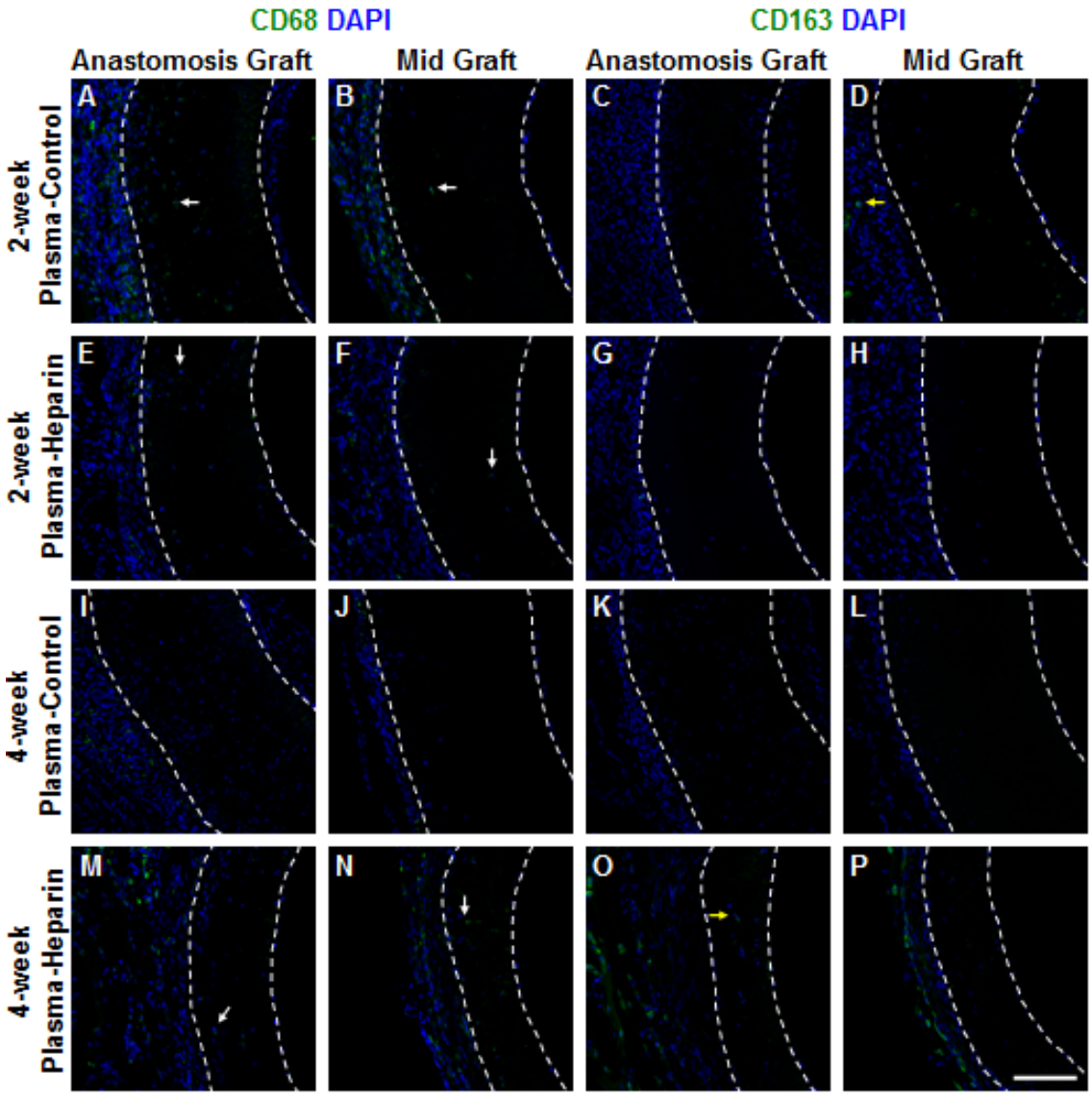

Figure 4.7. Inflammatory response of PCU plasma-control and plasma-heparin grafts after 2 and 4 weeks *in vivo*. Immunostaining for CD68 (green), and CD163 (green) of the cross-sections obtained from the anastomosis-graft and mid-graft regions of the plasma-control and plasma-heparin grafts after (A-H) 2 weeks and (I-P) 4 weeks *in*

vivo was performed. White and yellow arrows indicate cells positive for CD68 and CD163, respectively. White dashed lines delineate the border of the graft wall. Cell nuclei were stained using DAPI (blue). Scale bar = 100 μm.

Nevertheless, our *in vivo* study was solely a short-term study to evaluate the efficacy of our optimized surface modification, specifically end-point immobilization of heparin, on an electrospun PCU vascular graft. Because such short-term study could only provide initial assessment of graft performance in terms of early stages of thrombogenic response and endothelialization, long-term studies, including 6-month and 1-year durations, are necessary to fully determine the stability of the heparin conjugation and its effects, along with the structural and mechanical features of electrospun PCU, on endothelialization and ultimately graft integration and regeneration. In fact, complete luminal endothelialization remains crucial for the success of vascular grafts *in vivo*. Therefore, additional bioactive molecules, such as stromal cell-derived factor-1α (SDF-1α) that we have shown to accelerate endothelialization and remodeling through the recruitment of progenitor cells, can be additionally incorporated to further enhance the performance of and endow self-regenerative potential to our small-diameter PCU vascular grafts for blood vessel regeneration.

Conclusions

In this study, we successfully developed small-diameter nanofibrous vascular grafts using a thermoplastic polycarbonate-urethane, Carbosil®. These electrospun grafts possessed fibrous structure as well as mechanical strength that closely mimic those of the native vessels. We then showed that desired surface functionalization could be achieved using plasma treatment, a technique that we demonstrated to be significantly more effective compared to alternative methods such as aminolysis and physical adsorption via polydopamine coating. In addition, these functional amine groups grafted on the graft surface were used for subsequent conjugation of heparin. In fact, plasma treatment followed by reductive amination permitted end-point immobilization of heparin molecules on the graft surface, providing not only higher surface density but more importantly better stability and antithrombogenic activity. Furthermore, from our short-term *in vivo* study, we demonstrated that the end-point immobilized heparin drastically improved the performance of the vascular grafts with respect to patency as well as early stages of endothelialization and graft integration. Therefore, this engineering approach combined with optimal surface modification can serve as a foundation to develop small-diameter vascular grafts that possess off-the-shelf availability and desired bioactivity, which will have translational impact on the clinical treatment of vascular diseases.

References

1. Kochanek K, Murphy S, Miniño A, Kung H. Deaths: final data for 2009. Natl Vital Stat Rep. 2011;60(3):1-117.
2. Faries PL, LoGerfo FW, Arora S, Hook S, Pulling MC, Akbari CM, et al. A comparative study of alternative conduits for lower extremity revascularization: All-autogenous conduit versus prosthetic grafts. Journal of Vascular Surgery. 2000;32(6):1080-90.
3. Isenberg BC, Williams C, Tranquillo RT. Small-diameter artificial arteries engineered in vitro. Circulation Research. 2006;98(1):25-35.
4. MacNeill BD, Pomerantseva I, Lowe HC, Oesterle SN, Vacanti JP. Toward a new blood vessel. Vascular Medicine. 2002;7(3):241-6.
5. Greisler HP. Interactions at the blood/material interface. Annals of Vascular Surgery. 1990;4(1):98-103.
6. Hoenig MR, Campbell GR, Rolfe BE, Campbell JH. Tissue-engineered blood vessels: alternative to autologous grafts? Arteriosclerosis, Thrombosis, and Vascular Biology. 2005;25(6):1128-34.
7. Conte MS. The ideal small arterial substitute: a search for the Holy Grail? The FASEB Journal. 1998;12(1):43-5.
8. Weinberg CB, Bell E. A blood vessel model constructed from collagen and cultured vascular cells. Science. 1986;231(4736):397-400.
9. Niklason LE, Gao J, Abbott WM, Hirschi KK, Houser S, Marini R, et al. Functional arteries grown in vitro. Science. 1999;284(5413):489-93.
10. Kaushal S, Amiel GE, Guleserian KJ, Shapira OM, Perry T, Sutherland FW, et al. Functional small-diameter neovessels created using endothelial progenitor cells expanded ex vivo. Nat Med. 2001;7(9):1035-40.
11. L'Heureux N, Dusserre N, Konig G, Victor B, Keire P, Wight TN, et al. Human tissue-engineered blood vessels for adult arterial revascularization. Nat Med. 2006;12(3):361-5.
12. Dahl SLM, Kypson AP, Lawson JH, Blum JL, Strader JT, Li Y, et al. Readily available tissue-engineered vascular grafts. Science Translational Medicine. 2011;3(68):68ra9-ra9.
13. Wu W, Allen RA, Wang Y. Fast-degrading elastomer enables rapid remodeling of a cell-free synthetic graft into a neoartery. Nat Med. 2012;18(7):1148-53.
14. Hashi CK, Zhu Y, Yang G-Y, Young WL, Hsiao BS, Wang K, et al. Antithrombogenic property of bone marrow mesenchymal stem cells in nanofibrous vascular grafts. Proceedings of the National Academy of Sciences. 2007;104(29):11915-20.
15. Stitzel J, Liu J, Lee SJ, Komura M, Berry J, Soker S, et al. Controlled fabrication of a biological vascular substitute. Biomaterials. 2006;27(7):1088-94.
16. Ma Z, Kotaki M, Inai R, Ramakrishna S. Potential of nanofiber matrix as tissue-engineering scaffolds. Tissue Engineering. 2005;11(1-2):101-9.

17. Liang D, Hsiao BS, Chu B. Functional electrospun nanofibrous scaffolds for biomedical applications. Advanced Drug Delivery Reviews. 2007;59(14):1392-412.
18. Grasl C, Bergmeister H, Stoiber M, Schima H, Weigel G. Electrospun polyurethane vascular grafts: In vitro mechanical behavior and endothelial adhesion molecule expression. Journal of Biomedical Materials Research Part A. 2010;93A(2):716-23.
19. Bergmeister H, Grasl C, Walter I, Plasenzotti R, Stoiber M, Schreiber C, et al. Electrospun small-diameter polyurethane vascular grafts: ingrowth and differentiation of vascular-specific host cells. Artificial Organs. 2012;36(1):54-61.
20. Feng Y, Tian H, Tan M, Zhang P, Chen Q, Liu J. Surface modification of polycarbonate urethane by covalent linkage of heparin with a PEG spacer. Transactions of Tianjin University. 2013;19(1):58-65.
21. Tiwari A, Salacinski H, Seifalian AM, Hamilton G. New prostheses for use in bypass grafts with special emphasis on polyurethanes. Vascular. 2002;10(3):191-7.
22. Pinchuk L. A review of the biostability and carcinogenicity of polyurethanes in medicine and the new generation of 'biostable' polyurethanes. J Biomater Sci Polym Ed. 1994;6(3):225-67.
23. Szycher M, Reed A, Siciliano A. In vivo testing of a biostable polyurethane. J Biomater Appl. 1991;6(2):110-30.
24. Zdrahala R. Small caliber vascular grafts. Part II: Polyurethanes revisited. J Biomater Appl. 1996;11(1):37-61.
25. Szelest-Lewandowska A, Masiulanis B, Szymonowicz M, Pielka S, Paluch D. Modified polycarbonate urethane: synthesis, properties and biological investigation in vitro. J Biomed Mater Res A. 2007;82(2):509-20.
26. Guo J, Zhao M, Ti Y, Wang B. Study on structure and performance of polycarbonate urethane synthesized via different copolymerization methods. Journal of Materials Science. 2007;42(14):5508-15.
27. Khan I, Smith N, Jones E, Finch DS, Cameron RE. Analysis and evaluation of a biomedical polycarbonate urethane tested in an in vitro study and an ovine arthroplasty model. Part I: materials selection and evaluation. Biomaterials. 2005;26(6):621-31.
28. Nakagawa Y, Ota K, Sato Y, Teraoka S, Agishi T. Clinical trial of new polyurethane vascular grafts for hemodialysis: compared with expanded polytetrafluoroethylene grafts. Artif Organs. 1995;19(12):1227-32.
29. Walpoth B, Rogulenko R, Tikhvinskaia E, Gogolewski S, Schaffner T, Hess O, et al. Improvement of patency rate in heparin-coated small synthetic vascular grafts. Circulation. 1998;98(19 Suppl):II319-23.
30. Jeschke M, Hermanutz V, Wolf S, Köveker G. Polyurethane vascular prostheses decreases neointimal formation compared with expanded polytetrafluoroethylene. J Vasc Surg. 1999;29(1):168-76.
31. Aldenhoff YBJ, van der Veen FH, ter Woorst J, Habets J, Poole–Warren LA, Koole LH. Performance of a polyurethane vascular prosthesis carrying a dipyridamole (Persantin®) coating on its lumenal surface. Journal of Biomedical Materials Research. 2001;54(2):224-33.

32. Tai NR, Salacinski HJ, Edwards A, Hamilton G, Seifalian AM. Compliance properties of conduits used in vascular reconstruction. British Journal of Surgery. 2000;87(11):1516-24.
33. Salacinski HJ, Goldner S, Giudiceandrea A, Hamilton G, Seifalian AM, Edwards A, et al. The mechanical behavior of vascular grafts: a review. Journal of Biomaterials Applications. 2001;15(3):241-78.
34. Hirsh J, Anand SS, Halperin JL, Fuster V. Guide to anticoagulant therapy: Heparin: a statement for healthcare professionals from the American Heart Association. Circulation. 2001;103(24):2994-3018.
35. Capila I, Linhardt R. Heparin-protein interactions. Angew Chem Int Ed Engl. 2002;41(3):391-412.
36. Janairo RRR, Henry JJD, Lee BL, Hashi CK, Derugin N, Lee R, et al. Heparin-modified small-diameter nanofibrous vascular grafts. NanoBioscience, IEEE Transactions on. 2012;11(1):22-7.
37. Alferiev IS, Connolly JM, Stachelek SJ, Ottey A, Rauova L, Levy RJ. Surface heparinization of polyurethane via bromoalkylation of hard segment nitrogens. Biomacromolecules. 2005;7(1):317-22.
38. Lu Y, Shen L, Gong F, Cui J, Rao J, Chen J, et al. Polycarbonate urethane films modified by heparin to enhance hemocompatibility and endothelialization. Polymer International. 2012;61(9):1433-8.
39. Ku SH, Park CB. Human endothelial cell growth on mussel-inspired nanofiber scaffold for vascular tissue engineering. Biomaterials. 2010;31(36):9431-7.
40. Shin YM, Lee YB, Kim SJ, Kang JK, Park J-C, Jang W, et al. Mussel-inspired immobilization of vascular endothelial growth factor (VEGF) for enhanced endothelialization of vascular grafts. Biomacromolecules. 2012;13(7):2020-8.
41. Tsai W-B, Chen W-T, Chien H-W, Kuo W-H, Wang M-J. Poly(dopamine) coating of scaffolds for articular cartilage tissue engineering. Acta Biomaterialia. 2011;7(12):4187-94.
42. Tsai W-B, Chen W-T, Chien H-W, Kuo W-H, Wang M-J. Poly(dopamine) coating to biodegradable polymers for bone tissue engineering. Journal of Biomaterials Applications. 2014;28(6):837-48.
43. Kawamoto Y, Nakao A, Ito Y, Wada N, Kaibara M. Endothelial cells on plasma-treated segmented polyurethane. J Mater Sci Mater Med. 1997;8(9):551-7.
44. Bae J-S, Seo E-J, Kang I-K. Synthesis and characterization of heparinized polyurethanes using plasma glow discharge. Biomaterials. 1999;20(6):529-37.
45. Lee BL-P, Jeon H, Wang A, Yan Z, Yu J, Grigoropoulos C, et al. Femtosecond laser ablation enhances cell infiltration into three-dimensional electrospun scaffolds. Acta Biomaterialia. 2012;8(7):2648-58.
46. Hashi CK, Derugin N, Janairo RRR, Lee R, Schultz D, Lotz J, et al. Antithrombogenic modification of small-diameter microfibrous vascular grafts. Arteriosclerosis, Thrombosis, and Vascular Biology. 2010;30(8):1621-7.
47. Zhu Y, Gao C, He T, Shen J. Endothelium regeneration on luminal surface of polyurethane vascular scaffold modified with diamine and covalently grafted with gelatin. Biomaterials. 2004;25(3):423-30.

48. Lee BL-P, Tang Z, Wang A, Huang F, Yan Z, Wang D, et al. Synovial stem cells and their responses to the porosity of microfibrous scaffold. Acta Biomaterialia. 2013;9(7):7264-75.
49. Yu J, Wang A, Tang Z, Henry J, Li-Ping Lee B, Zhu Y, et al. The effect of stromal cell-derived factor-1α/heparin coating of biodegradable vascular grafts on the recruitment of both endothelial and smooth muscle progenitor cells for accelerated regeneration. Biomaterials. 2012;33(32):8062-74.
50. Lee H, Dellatore SM, Miller WM, Messersmith PB. Mussel-inspired surface chemistry for multifunctional coatings. Science. 2007;318(5849):426-30.
51. Murugesan S, Xie J, Linhardt R. Immobilization of heparin: approaches and applications. Curr Top Med Chem. 2008;8(2):80-100.
52. Begovac PC, Thomson RC, Fisher JL, Hughson A, Gällhagen A. Improvements in GORE-TEX® vascular graft performance by Carmeda® bioactive surface heparin immobilization. European Journal of Vascular and Endovascular Surgery. 2003;25(5):432-7.
53. Chuang T-W, Masters KS. Regulation of polyurethane hemocompatibility and endothelialization by tethered hyaluronic acid oligosaccharides. Biomaterials. 2009;30(29):5341-51.
54. Noel S, Liberelle B, Robitaille L, De Crescenzo G. Quantification of primary amine groups available for subsequent biofunctionalization of polymer surfaces. Bioconjugate Chemistry. 2011;22(8):1690-9.
55. Wong KKH, Hutter JL, Zinke-Allmang M, Wan W. Physical properties of ion beam treated electrospun poly(vinyl alcohol) nanofibers. European Polymer Journal. 2009;45(5):1349-58.
56. Gibeop N, Lee DW, Prasad CV, Toru F, Kim BS, Song JI. Effect of plasma treatment on mechanical properties of jute fiber/poly (lactic acid) biodegradable composites. Advanced Composite Materials. 2013;22(6):389-99.
57. He W, Yong T, Teo WE, Ma Z, Ramakrishna S. Fabrication and endothelialization of collagen-blended biodegradable polymer nanofibers: potential vascular graft for blood vessel tissue engineering. Tissue Engineering. 2005;11(9-10):1574-88.
58. Riesenfeld J, Olsson P, Sanchez J, Mollnes T. Surface modification with functionally active heparin. Med Device Technol. 1995;6(2):24-31.
59. Bernfield M, Götte M, Park PW, Reizes O, Fitzgerald ML, Lincecum J, et al. Functions of cell surface heparan sulfate proteoglycans. Annual Review of Biochemistry. 1999;68(1):729-77.
60. Powell AK, Yates EA, Fernig DG, Turnbull JE. Interactions of heparin/heparan sulfate with proteins: Appraisal of structural factors and experimental approaches. Glycobiology. 2004;14(4):17R-30R.
61. Cheng Q, Lee BL-P, Komvopoulos K, Yan Z, Li S. Plasma surface chemical treatment of electrospun poly(L-lactide) microfibrous scaffolds for enhanced cell adhesion, growth, and infiltration. Tissue Eng Part A. 2013;19(9-10):1188-98.
62. Badylak SF, Valentin JE, Ravindra AK, McCabe GP, Stewart-Akers AM. Macrophage phenotype as a determinant of biologic scaffold remodeling. Tissue Engineering Part A. 2008;14(11):1835-42.

63. Lever R, Smailbegovic A, Page CP. Locally available heparin modulates inflammatory cell recruitment in a manner independent of anticoagulant activity. European Journal of Pharmacology. 2010;630(1–3):137-44.

CHAPTER 5

Concluding Remarks

Tissue engineering undoubtedly is and will be one of the most popular and researched scientific fields because of its limitless potential to improve the lives of patients diagnosed with a broad range of diseases and health problems. The concept of engineering artificial tissues to replace, repair, and ultimately regenerate damaged or lost tissues is a multidisciplinary approach that bridges primarily biology and engineering as well as chemistry, material science, drug delivery, medicine, and many more. In addition, tissue engineering reflects upon the various complex biological systems that naturally occur in our body, and the efficient role they play in controlling not only the development and maturation but also the inevitable deterioration and death of tissues. Therefore, although the main goal is to develop new technologies in constructing artificially engineered tissues and organs, a true motivation behind current and future tissue engineering research is to elucidate and better understand the constant interactions among cells, extracellular matrix (ECM) and its vast pool of proteins, bioactive molecules such as growth factors and transcription factors, etc. Such understanding will then provide scientists, like me, the knowledge to formulate effective and advanced strategies for diagnostics, disease prevention, and regenerative therapies.

The scope of the investigations detailed in this dissertation aims to address the engineering and optimization of tissue-engineered scaffolds from a structural and chemical perspective, focusing on the development of bioactive scaffolds with refined micro/nano structure and enhanced surface chemistry for tissue regeneration. In particular, we have utilized the well-reported electrospinning technique to fabricate biomimetic scaffolds with fibrous structure designed to emulate the natural ECM in terms of both physical and biological properties. However, despite the high surface-area-to-volume ratio favorable for the attachment of cells and bioactive molecules, electrospun scaffolds possess densely packed network of fibers, especially in nanoscale, resulting in small pore size that is unconducive for cell infiltration and tissue ingrowth, two critical factors in the progression of angiogenesis and tissue integration. In order to mitigate and overcome this physical barrier, we explored distinct fabrication methods and post-fabrication processes to engineer and tailor the micro/nano structure of electrospun scaffolds, such as the incorporation of sacrificial fibers and laser ablation, to not only promote cell migration and infiltration but also regulate stem cell differentiation in these three-dimensional scaffolds. Furthermore, we investigated several post-fabrication methods to manipulate the surface chemistry of the scaffolds, such as wet chemistry, polydopamine-mediated adhesion, and plasma treatment, specifically to assess the potential of nanofibrous scaffolds as small-diameter grafts for vascular regenerative therapy. Thus, the studies discussed encompass key elements of the physicochemical properties of electrospun

scaffolds in terms of both structural and chemical modulations for optimal performance in desired tissue engineer applications.

In Chapter 2, we combined bioengineering and mechanical engineering as we examined the application of ultrafast laser microprocessing for structural modification of biomaterial scaffolds. Specifically, we employed a femtosecond (FS) laser system, a powerful and promising tool, to ablate and create microscale topographical features on electrospun poly(L-lactide) (PLLA) nanofibrous scaffolds, and subsequently evaluated the effects of these cues on the behavior of seeded human mesenchymal stem cells (hMSCs) *in vitro* and host response *in vivo*. We uniformly patterned structured through-holes with varying diameters and spacings between adjacent holes on the scaffolds. We demonstrated that ablation with FS laser did not cause fiber melting as our system provided better control of ablation intensity in relation to increasing laser energy and pulse number. In addition, we observed changes in hMSC morphology in response to these through-holes as their morphology appeared to be dictated by the patterned features, but no adverse effects in terms of adhesion and proliferation were noted. More importantly, our *in vivo* study to assess the effect of patterned holes on cell infiltration and tissue integration revealed that holes of varying size and density promoted better endothelial cell ingrowth as well as M2 macrophage and overall cell infiltration, which are critical for angiogenesis and tissue remodeling, in comparison to control (non-ablated) scaffolds. Our findings indicated that laser ablation, especially ultrafast FS laser processing, could be one promising post-fabrication approach to effectively create desired nano- or micro-structural features as a mean to influence cell behavior and improve the integration and function of tissue-engineered scaffolds *in vivo*.

Chapter 3 combined stem cell technology with porous microfibrous scaffold as we investigated the effect of biophysical factors, such as porosity and pore size, on the behavior and differentiation of stem cells. Because acellular scaffolds alone have limited success in the regeneration of complex tissues such as cartilage and bone, it may be more advantageous and ideal to combine stem cells and biomaterials in order to better control cell behavior and harness their regenerative potential using biophysical cues provided by the scaffold structure. Thus, this motivated us to search for an alternative yet more optimal source of multipotent adult stem cells. Interestingly, we identified and characterized a new type of stem cells that can be harvested from the synovial membrane of knee joint, which we referred to as neural crest cell-like synovial stem cells (NCCL-SSCs) based on their multipotent potential and resemblance to neural crest stem cells (NCSCs). The multipotency of NCCL-SSCs could be preserved under optimized maintenance conditions, but these cells could be differentiated into cell types of both mesenchymal and ectodermal lineages when exposed to cocktails of biochemical factors in specific induction media. To better understand how stem cells interact with their microenvironment and whether biophysical features can impact their behavior, we fabricated a composite scaffold via co-electrospinning of two polymers. We used the slow-degrading PLLA to produce structural fibers and the fast-degrading poly(glycolic acid) (PGA) to make sacrificial fibers, and subsequently degraded the composite scaffolds to remove the sacrificial PGA fibers and increase pore size and porosity. We noted that higher ratio of PGA fibers and longer degradation time resulted in higher porosity and larger pore size, both of which exhibited no adverse effect on NCCL-SSC adhesion and proliferation *in vitro* as well as an increased cell infiltration into and

distribution throughout the highly porous scaffolds *in vivo*. More importantly, we determined that such changes in the scaffold porosity could regulate stem cell differentiation, as NCCL-SSCs cultured on the more porous scaffolds without additional biochemical cues from specific induction media showed increased expression of chondrogenic and osteogenic markers and decreased expression of smooth muscle cell and adipogenic markers. Therefore, this study not only advanced our understanding of adult stem cells, but also established a foundation for the design and development of desirable scaffolds using multiple biomaterials with distinct physical properties for *in situ* tissue engineering via chemotactic homing of local tissue-specific stem cells.

In Chapter 4, we transitioned from a physical perspective to focus more on the control of surface properties in the development and fabrication of small-diameter bioactive vascular graft. Because of the unmet need for small-diameter (< 6 mm) vascular grafts as blood vessel substitutes, our motivation was to produce the next-generation, ideal vascular graft with excellent performance *in vivo*. We selected Carbosil®, a commercially available thermoplastic polycarbonate-urethane (PCU), as the material to electrospin our small-diameter vascular grafts, and subsequently utilized various surface modification strategies to endow desired bioactivity as we determined the most effective method to conjugate heparin onto the graft surface given its antithrombogenic properties. We demonstrated that PCU could be a prime polymer in fabricating vascular grafts, as its mechanical strength and compliance closely mimicked those of native vessels. In addition, we compared the effectiveness of heparin conjugation via EDC chemistry, polydopamine adsorption, and plasma treatment, and concluded that the most effective and stable approach was the combination of plasma treatment and reductive amination. In fact, plasma treatment provided the highest density of functional amine groups on the graft surface, which were used for reductive amination to enable end-point immobilization of heparin. This orientation not only increased the surface density of conjugated heparin but more importantly better stabilized the immobilized heparin and preserved its antithrombogenic activity. Furthermore, through short-term *in vivo* rat model studies, we showed that the plasma-treated PCU grafts conjugated with heparin (plasma-heparin) exhibited excellent patency as well as endothelialization and graft integration compared to plasma-control grafts without heparin, further suggesting the effectiveness of our optimized modification technique and the beneficial bioactivity of the immobilized heparin.

From the studies discussed in this dissertation, we investigated and detailed novel strategies to ultimately enhance the functional performance and tissue integration of electrospun scaffolds by enlarging the pore size and regulating structural components. In particular, we demonstrated that the incorporation of multiple polymers with sacrificial components and the post-fabrication utilization of FS laser are simply two promising and distinct strategies to alter pore size, porosity, and other structural facets of biomaterial scaffolds. For example, FS laser patterning could be finely controlled to create desired topographical features of various sizes, shapes, depths, etc. However, future studies and direction could be aimed to further improve and tune the scaffold architecture (i.e. interconnectivity of pores) to achieve enhanced vascularization and desired regulation of cell differentiation, along with elucidating the mechanisms and factors involved in these processes. Subsequently, we translated our findings and knowledge into the development of small-diameter, bioactive vascular grafts with not only optimal mechanical properties

but more importantly desired chemical characteristics. We hope that such design improvements from both physical and chemical perspectives can be integrated with an assortment of tissue engineering applications, providing new ways to accelerate the regeneration of functional native tissue while ensuring the success of implanted medical devices.

Appendix A

Gene	Forward	Reverse
Collagen II	CCAGGGCTCCAATGATGTG	GTGTTTCGTGCAGCCATCCT
Aggrecan	CTTCAAGCTGAACTATGACCACTTTACT	CATGGTCTGGAACTTCTTCTGAGA
BGLAP	GCAGACCTAGCAGACACCATGA	AGGTCAGAGAGGCAGAATGCA
Runx2	TCAATGGTTGGGAGAGAAGCA	CCTTCTGCACCTCCTTTAGCA
SMA	TCCTGACCCTGAAGTATCCGATA	GGTGCCAGATCTTTTCCATGTC
CNN1	AGAACAAGCTGGCCCAGAAA	CACCCCTTCGATCCACTCTCT
PPARγ	CGAGCCCTGGCAAAGCATTTGTAT	TGTCTTTCCTGTCAAGATCGCCCT
LPL	ACAGTCTTGGAGCCCATGCT	CAAGCCAGTAATTCTATTGACCTTCTT
18S	GCCGCTAGAGGTGAAATTCTTG	CATTCTTGGCAAATGCTTTCG

Supplemental Table 3.1. Primer sequences used in the study. Sequences of the primers used for the qPCR of each gene are listed in this table.